Technische Universität München
Fakultät für Physik

Dissertation

Scattering and Absorption of Ultracold Atoms by Nanotubes

Martin Fink

Physik Department
Fachgebiet Theoretische Atomphysik
Prof. Dr. Harald Friedrich

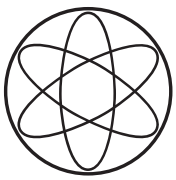

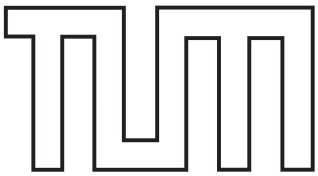

Technische Universität München
Physik Department
Fachgebiet Theoretische Atomphysik

Scattering and Absorption of Ultracold Atoms by Nanotubes

Dipl.-Phys. (Univ.) Martin Norbert Fink

Vollständiger Abdruck der von der Fakultät für Physik der Technischen Universität München zur Erlangung des akademischen Grades eines

Doktors der Naturwissenschaften (Dr. rer. nat.)

genehmigten Dissertation.

Vorsitzender:		Univ.-Prof. Dr. Peter Böni
Prüfer der Dissertation:	1.	Univ.-Prof. Dr. Harald Friedrich (i.R.)
	2.	Univ.-Prof. Dr. Martin Zacharias

Die Dissertation wurde am 04.04.2013 bei der Technischen Universität München eingereicht und durch die Fakultät für Physik am 18.06.2013 angenommen.

Contents

List of Figures

List of Tables

Introduction

In atomic molecular and optical (AMO) physics remarkable progress has been made during the last years. Cooling the motion of atoms down to few nanokelvin has become state of the art and the regime of ultracold temperatures has attracted a considerable amount of interest in this field of AMO physics [1–3]. The regime of ultracold temperatures is governed by quantum mechanical effects, one of the most prominent ones being the formation of a Bose-Einstein condensate (BEC) [4, 5]. Advances in trapping clouds or even single atoms in optical or magnetic traps allows precise control and manipulation of atomic samples [6, 7]. Atom chips enable an accurate positioning of atoms and their transportation over long distances [6–10].

In solid state physics significant progress has been made in particular in nanophysics [11, 12]. New microfabrication techniques have been developed and enable a preparation of mesoscopic structures on the micro- and nanometre scale. This provides a large variety of nanometre sized structures like nanogratings [13, 14] or structured surfaces [15, 16] as well as various geometries such as nanowires, nanotubes and nanorods [12, 17] or even more complex nanostructures [11].

A coupling of an atomic quantum system to a mesoscopic solid-state object constitutes a so called hybrid quantum system. These hybrid systems combine the high controllability on a quantum level in AMO physics with the variety of mesoscopic structures available in solid state or nanophysics [18–21]. A coupling can be provided by optical photons of a laser field as it is typically used in the context of quantum information theory where a coherent and controllable system is achieved [22]. However, a direct coupling between the atomic system and the solid-state object is provided by the quantum mechanical vacuum fluctuations of the electromagnetic field. The presence of a reflecting and refracting solid-state surface constrains the electromagnetic field and leads to a position dependent energy shift of the atom. This gives rise to the so called Casimir-Polder dispersion force acting between a (neutral) atom and a mesoscopic object [23, 24]. For ground state atoms, the corresponding interaction potential is typically attractive and depends crucially on the geometry of the surface, the dielectric properties of the mesoscopic object as well as on the internal properties of the atomic component of the system. Therefore such hybrid systems may provide insight into the underlying physics of dispersion forces, shape, size and properties of the solid-state object as well as of the atom or the atomic ensemble.

One of the first experimental investigations of ultracold atoms interacting with a solid-state surface via a Casimir-Polder potential goes back to Shimizu who measured the reflection of ultracold metastable neon atoms from a plane silicon surface [25]. The interaction potential was first derived by Lennard-Jones in 1932 [26] who proposed a $-1/d^3$ behaviour, where d is the distance of the atom to the surface. Later Casimir and Polder took into

account retardation effects – originating from the finite time it takes a virtual photon, mediating the interaction, to travel from the atom to the surface – and observed corrections to the result of Lennard-Jones. At large distances the full potential differs from its non-retarded counterpart and shows a $-1/d^4$ behaviour [23]. A classical reflection process is forbidden as this interaction potential is purely attractive and the nature of the finite reflection probability that was observed by Shimizu, is thus purely quantum mechanical. In particular in the low-energy regime, this quantum reflection becomes dominant and the reflection probability approaches unity in the limit of small incident velocities. This first measurement of the extremely non-classical process of quantum reflection stimulated further research in this field, both theoretically [27–29] and experimentally [15, 16, 30, 31]. However, the atom-plane system can only be tuned by the choice of the projectile atom or by the surface material which offers only limited possibilities.

Further solid-state components of different geometry and size introduce further parameters into the system and can be implemented and used to design more complex hybrid quantum systems. The interaction between the atomic and the solid-state constituent in a hybrid system crucially depends on the shape of the solid-state surface in particular if the size of the solid-state object becomes comparable to the typical length scales of the coupling potential. For Casimir-Polder interactions, typical length scales of the potential range from several nanometres up to few micrometres. Benefiting from advanced microfabrication techniques, solid-state structures of comparable size can be fabricated and implemented in hybrid systems. Such complex hybrid systems may provide useful tools in various fields of physics; exploring the behaviour and properties of atomic ensembles or quantum gases like a BEC, investigating the wave nature of single atoms or large molecules in diffraction experiments, analysing the shape, size and optical properties of solid-state objects or studying the behaviour of the Casimir-Polder interaction between atoms and solid-state surfaces at various regimes of atom-surface distances.

Nanotubes, nanowires and nanorods have proven effective for constructing various kinds of hybrid systems [17, 32–34]. New techniques have been developed that allow a precise fabrication of tubes with a diameter down to few nanometres only and a length up to tens of micrometres [35–38]. These nanotubes can be grown on top of nanochips forming diverse nanostructures and may also be integrated in complex hybrid systems. Combining them into carpets of dense standing nanotubes forms a structured surface, which can be used to study the influence of surface roughness on the quantum reflection probability of atoms from surfaces [15, 30, 39]. An array of nanotubes can serve as a diffraction grating to study diffraction and interference of large molecules or single atoms [13, 14]. Furthermore, nanowire-based hybrid systems, where an atomic quantum gas couples to the mechanical vibration of a nanowire have been proposed [40].

The basis for complex nanowire-based hybrid systems is the interaction of a single atom with a cylindrical geometry and the corresponding scattering process [41, 42]. This fundamental system lays the foundation for understanding systems of higher complexity. Nevertheless, this seemingly simple problem turns out to be non-trivial due to the two-dimensional character of the system [43–46] and due to the intricacy of the exact interaction potential [42, 47, 48].

The present thesis deals with the fundamental system of a single atom interacting with a cylindrical geometry. An accurate description of this system needs to take into account

both the exact Casimir-Polder interaction as well as the two-dimensional nature of the system. This forms the basis for a detailed analysis of the scattering and absorption of ultracold atoms by nanotubes. In a second step, the results obtained within this fundamental system can be applied to a complex hybrid system of a nanotube immersed in a cold quantum gas, which is recently of particular interest both theoretically and experimentally [49–51]. This dependable approach can give insight into the underlying processes and promote a deeper understanding of this hybrid quantum system.

Outline of the thesis

In Chapter 1, the theoretical framework for the description of the scattering of atoms at a cylindrical solid-state structure is presented. The scattering process is described within two-dimensional scattering theory, which differs significantly from the well-studied three-dimensional case, in particular in the low-energy regime of ultracold atoms. The dynamics of the scattering process at large distances is governed by the long-range Casimir-Polder potential. Close to the surface, the interaction becomes complicated and an accurate and model-independent description of this highly reactive short-range regime is achieved within the Langevin model using incoming boundary conditions.

In Chapter 2, we study the Casimir-Polder interaction for an atom facing a cylindrical geometry. This potential has in general a quite complicated form but simplifies significantly in the non-retarded and in the highly retarded limit where retardation effects are either negligible or dominant. In these limits, analytical expressions for the asymptotic behaviour of the interaction potential are given. An accurate description of the full Casimir-Polder potential, which undergoes a smooth transition from the non-retarded limit at small distances to the highly retarded limit at large atom-surface separations, is given within a shape-function approach. This enables an accurate numerical evaluation of the interaction potential for all distances. This method is successfully applied to the Casimir-Polder potential of a hydrogen atom facing a cylindrical geometry.

The scattering of ultracold atoms at a cylindrical geometry is discussed in Chapter 3. The scattering process in this low-energy regime is governed by the scattering length. Numerical results of the scattering length are presented in the thin and thick-wire limit where analytical expressions are derived. Particular attention is given to the fundamental question of the influence of retardation effects on the scattering process, where a significant difference between a metallic, perfectly conducting cylinder and an insulating tube is observed. Furthermore, the scattering of atoms is compared to the diffraction of light at a cylindrical geometry where the existence of an electromagnetic limit and of a non-electromagnetic limit is shown.

In Chapter 4, we study a more complex hybrid system consisting of a single carbon nanotube (CNT) immersed in an ultracold atomic quantum gas, such as a cloud of thermal atoms or a Bose-Einstein condensate. We show that this system is properly described on the basis of the fundamental scattering process discussed before. The predicted trap loss in this system is in agreement with recent experimental results by Schneeweiss *et al.* [49]. This parameter-free approach offers a foundation for extensions to more complex hybrid systems and might assist the design of CNT based nanodevices.

Chapter 1

Theoretical Framework

An atom scattered at a cylindrical geometry forms a system that is translationally invariant along the axis of the cylinder. The longitudinal free motion along the cylinder is separated from the two-dimensional dynamics perpendicular to the cylinder. This leads to an effectively two-dimensional system, which is governed by the interaction potential. In this chapter, the general concept for the treatment of an atom colliding with a cylindrical geometry, such as a nanotube, is developed. The collision process is described within the framework of scattering theory [52–57], which is presented in the first part of this chapter for the present case of an effectively two-dimensional system (Section 1.1). An accurate method for the description of the highly-reactive interaction processes in the region close to the surface of a mesoscopic structure is given within the Langevin model [58] (Section 1.2).

1.1 Scattering in two dimensions

The scattering of an atom at a mesoscopic structure, such as a plane wall or a cylindrical or spherical geometry, is described within the framework of scattering theory, which is a well-established field of theoretical physics [52–57]. Nevertheless the scattering process in the present two-dimensional system differs significantly from the well-studied three dimensional case, in particular in the low-energy regime of ultracold atoms [43–46].

1.1.1 Elastic scattering

The scattering process is in general a time-dependent problem. However, it is well described by a time-independent Schrödinger equation in most cases [54]. For a projectile particle of mass μ and energy $E = \hbar^2 k^2/(2\mu)$, interacting with the scattering target via the potential $V(\boldsymbol{r})$, the stationary Schrödinger equation for the two-dimensional system reads

$$\left[-\frac{\hbar^2}{2\mu}\Delta_{\mathrm{2D}} + V(\boldsymbol{r})\right]\psi(\boldsymbol{r}) = E\,\psi(\boldsymbol{r})\,, \tag{1.1}$$

with the two-dimensional Laplacian Δ_{2D} which is given in polar coordinates,

$$\Delta_{\mathrm{2D}} = \frac{\mathrm{d}^2}{\mathrm{d}r^2} + \frac{1}{r}\frac{\mathrm{d}}{\mathrm{d}r} + \frac{1}{r^2}\frac{\mathrm{d}^2}{\mathrm{d}\phi^2} = \frac{\mathrm{d}^2}{\mathrm{d}r^2} + \frac{1}{r}\frac{\mathrm{d}}{\mathrm{d}r} - \frac{\hat{L}_z^2}{r^2\hbar^2}\,, \tag{1.2}$$

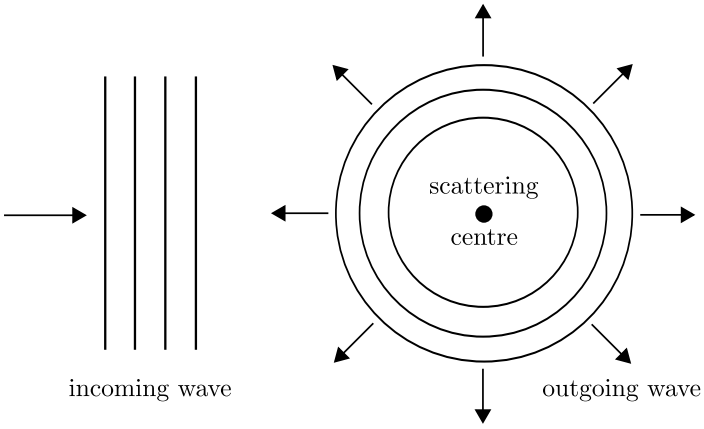

Figure 1.1: Schematic illustration of the two-dimensional scattering solution constituted by an incoming plane wave and an outgoing circular wave.

with the distance r to the scattering centre and the polar angle ϕ. The present work focuses on the scattering of neutral atoms by nanostructures where the interaction potential $V(\boldsymbol{r})$ vanishes faster than $1/r^2$,

$$\lim_{r\to\infty} r^2 V(\boldsymbol{r}) \to 0\,. \tag{1.3}$$

In this case, the scattering solution $\psi(\boldsymbol{r})$ in Eq. (1.1) has the following asymptotic form

$$\psi(\boldsymbol{r}) \overset{r\to\infty}{=} \mathrm{e}^{\mathrm{i}kx} + f(\phi)\frac{\mathrm{e}^{\mathrm{i}kr}}{\sqrt{r}}\,. \tag{1.4}$$

The first term on the right-hand side of Eq. (1.4) represents a "plane" incoming wave moving in positive x-direction with velocity $v = \hbar k/\mu$. The second term describes an outgoing circular wave, modulated by a *scattering amplitude* $f(\phi)$ depending on the polar angle ϕ (see Fig. 1.1). The flux density

$$\boldsymbol{j} = \frac{\hbar}{2\mathrm{i}\mu}\left(\psi^*\nabla\psi - \psi\nabla\psi^*\right) \tag{1.5}$$

for the plane wave is $k\hbar/\mu\,\boldsymbol{e}_x$, while the flux for the outgoing wave is

$$\boldsymbol{j}_{\mathrm{out}} \overset{r\to\infty}{=} \frac{\hbar k}{\mu}\frac{1}{r}\left|f(\phi)\right|^2\boldsymbol{e}_r + \mathcal{O}\left(r^{-2}\right)\,. \tag{1.6}$$

Here $\boldsymbol{e}_r$ ($\boldsymbol{e}_x$) denotes the unit vector pointing in radial direction (x-direction). The ratio of the flux scattered into the angle $\mathrm{d}\phi$ to the incoming current density defines the *differential scattering cross section* $\mathrm{d}\lambda/\mathrm{d}\phi$. The flux through the segment $r\mathrm{d}\phi$ is given by $\hbar k|f(\phi)|^2/\mu$ and the differential cross section is

$$\frac{\mathrm{d}\lambda}{\mathrm{d}\phi} = \left|f(\phi)\right|^2\,. \tag{1.7}$$

Integrating over the polar angle gives the *total elastic cross section*

$$\lambda_{\mathrm{el}} = \int\frac{\mathrm{d}\lambda}{\mathrm{d}\phi}\mathrm{d}\phi = \int_0^{2\pi}\left|f(\phi)\right|^2\mathrm{d}\phi\,. \tag{1.8}$$

Notice that due to the reduced dimensionality of the system the cross section has the dimension of a length. This is emphasised by the use of the letter "λ" instead of "σ", which typically denotes the cross section in three dimensions, which is a surface.

Partial-wave expansion

For an interaction potential $V(\boldsymbol{r})$ that is radially symmetric, $V(\boldsymbol{r}) = V(r)$, the angular momentum is conserved. We expand the solution of the stationary Schrödinger equation (1.1) in eigenfunctions of the angular part of the two-dimensional Laplacian (1.2),

$$\psi(\boldsymbol{r}) = \sum_{m=-\infty}^{+\infty} \frac{u_m(r)}{\sqrt{r}} \mathrm{e}^{\mathrm{i}m\phi}\,, \tag{1.9}$$

with the eigenfunction $\mathrm{e}^{\mathrm{i}m\phi}$ of the angular momentum operator $\hat{L}_z$ to the eigenvalue $\hbar m$ and the integer angular momentum quantum number m ranging from $-\infty$ to $+\infty$. The radial wave function $u_m(r)$ is a solution of the *radial Schrödinger equation*,

$$\left[-\frac{\hbar^2}{2\mu}\frac{\mathrm{d}^2}{\mathrm{d}r^2} + \frac{\hbar^2}{2\mu}\frac{m^2-1/4}{r^2} + V(r)\right] u_m(r) = \frac{\hbar^2 k^2}{2\mu} u_m(r)\,, \tag{1.10}$$

which has – in each partial wave – the same form as the full stationary Schrödinger equation for a one-dimensional system with an effective potential constituted by the centrifugal term and the interaction potential,

$$V_{\mathrm{eff}}(r) = \frac{\hbar^2}{2\mu}\frac{m^2-1/4}{r^2} + V(r)\,. \tag{1.11}$$

The centrifugal term in Eqs. (1.10) and (1.11) can be related to its familiar three-dimensional counterpart by substituting $|m| = l + 1/2$. Notice that the centrifugal term in two dimensions only depends on $|m|$ and is, in contrast to the three- or higher dimensional form, attractive for s waves, $m = 0$. This counter-intuitive attractive potential is just too weak to support a dipole series of bound states, but it significantly affects the near-threshold behaviour of the system (see Section 1.1.3).

The regular solution $u_m^{(\mathrm{c})}(r)$ and the irregular solution $u_m^{(\mathrm{s})}(r)$ of the free radial Schrödinger equation $[V(r) \equiv 0]$ in two dimensions are

$$u_m^{(\mathrm{c})}(r) = \sqrt{\frac{\pi}{2}kr}\; J_{|m|}(kr)\,, \tag{1.12}$$

and

$$u_m^{(\mathrm{s})}(r) = \sqrt{\frac{\pi}{2}kr}\; Y_{|m|}(kr)\,, \tag{1.13}$$

with cylindrical Bessel functions $J_m(x)$ and $Y_m(x)$ [59]. Their asymptotic behaviour is

$$u_m^{(\mathrm{c})}(r) \overset{r\to\infty}{\sim} \cos\left(kr - |m|\frac{\pi}{2} - \frac{\pi}{4}\right) \tag{1.14}$$

and

$$u_m^{(\mathrm{s})}(r) \overset{r\to\infty}{\sim} \sin\left(kr - |m|\frac{\pi}{2} - \frac{\pi}{4}\right)\,. \tag{1.15}$$

The solution $u_m(r)$ of the radial Schrödinger equation (1.10), including an interaction potential $V(r)$ vanishing faster than $1/r^2$, can – at large distances where the interaction potential is negligible – be written as a superposition of the regular solution $u_m^{(\mathrm{c})}(r)$ and irregular solution $u_m^{(\mathrm{s})}(r)$,

$$u_m(r) \overset{r\to\infty}{\propto} \cos(\delta_m) u_m^{(\mathrm{c})}(r) - \sin(\delta_m) u_m^{(\mathrm{s})}(r) \overset{r\to\infty}{\sim} \cos\left(kr - |m|\frac{\pi}{2} - \frac{\pi}{4} + \delta_m\right) , \tag{1.16}$$

which defines the energy-dependent *scattering phase shift* δ_m. Furthermore, the scattering solution in Eq. (1.4) can be expanded in partial waves and we obtain an expression for the scattering amplitude

$$f(\phi) = \sum_{m=-\infty}^{+\infty} f_m \mathrm{e}^{\mathrm{i}m\phi} , \quad f_m = \frac{1}{\sqrt{2\pi \mathrm{i}k}} \left(S_m - 1\right) . \tag{1.17}$$

The *partial wave amplitudes* f_m are determined by the S-matrix in partial wave m, $S_m = \mathrm{e}^{2\mathrm{i}\delta_m}$. The asymptotic form of the radial solution (1.16) yields,

$$u_m(r) \overset{r\to\infty}{\sim} \frac{\mathrm{i}^{|m|+1}}{\sqrt{2\pi k}} \left(\mathrm{e}^{-\mathrm{i}(kr - m\pi/2 + \pi/4)} - S_m \mathrm{e}^{+\mathrm{i}(kr - m\pi/2 + \pi/4)}\right) . \tag{1.18}$$

The total elastic cross section can easily be evaluated

$$\lambda_{\mathrm{el}} = \frac{1}{k} \sum_{m=-\infty}^{+\infty} |1 - S_m|^2 , \tag{1.19}$$

with the partial cross sections $\lambda_{\mathrm{el}}^{(m)} = |1 - S_m|^2/k$.

1.1.2 Inelastic and reactive collisions

In a more generalised case, the internal state of the projectile may also be affected by the interaction between the projectile and the scattering target. An additional coupling potential might change the internal state of the projectile during the scattering process; more complex reactions of the projectile with the scattering target may lead to a loss of the incoming projectile from the scattering process. The scattering without changing the initial state of the atom defines the elastic channel, which has been discussed above. A detailed description of the individual inelastic channels is possible [52] but not part of the present work. However, the total flux that is inelastically scattered or otherwise lost from the elastic channel is given by the net flux in the elastic channel, obtained from Eqs. (1.9) and (1.18),

$$\boldsymbol{j}_{\mathrm{abs}} = -\oint \boldsymbol{j}_{\mathrm{total}} \mathrm{d}\boldsymbol{s} = \frac{\hbar}{\mu} \sum_{m=-\infty}^{+\infty} \left(1 - |S_m|^2\right) \tag{1.20}$$

In the absence of any absorption processes, the net flux in the elastic channel vanishes as all incoming current is elastically scattered. Therefore the absolute value of the S-matrix is

$$|S_m| = 1 \tag{1.21}$$

and the scattering phase shift δ_m is a real-valued number. In the case of additional inelastic or reactive collisions the incoming net flux is non-vanishing and

$$|S_m| < 1\,, \tag{1.22}$$

leading to complex values of δ_m.

Quantum reflection and absorption cross section

The complex value of δ_m breaks up the intuition of a phase shift; however, we can interpret the first term in the brackets on the right-hand side of Eq. (1.18) as an incoming wave and the second term as the scattered, outgoing wave. This defines a *reflection amplitude* R_m of each partial wave which is connected to the S-matrix via $R_m = -S_m$. The corresponding reflection probability is $P_R^{(m)} = |R_m|^2$.

In classical mechanics, the reflection is either certain ($P_R = 1$) if there exists a classical turning point $r_{\rm ctp}$ – given by $E = V_{\rm eff}(r_{\rm ctp})$ – or impossible ($P_R = 0$) in the absence of any classical turning point. In contrast, the quantum mechanical reflection probability P_R can attain any value between zero and unity. If reflection is classically forbidden, a finite reflection probability is purely governed by quantum mechanical effects and therefore named *quantum reflection*, which is in particular a dominant effect in the scattering of ultracold atoms, see Section 1.1.3.

In analogy to the total elastic cross section (1.8), the total *absorption cross section* is given by the ratio of the absorbed flux (1.20) to the incoming flux which is $\hbar k/\mu$

$$\lambda_{\rm abs} = \frac{1}{k}\sum_{m=-\infty}^{+\infty}\left(1-|S_m|^2\right) = \frac{1}{k}\sum_{m=-\infty}^{+\infty}\left(1-P_R^{(m)}\right)\,, \tag{1.23}$$

with the partial absorption cross sections $\lambda_{\rm abs}^{(m)} = (1-|S_m|^2)/k$. In the case of purely elastic scattering ($|S_m| = 1$ for all m) the absorption cross section consequently vanishes.

1.1.3 Near-threshold behaviour

In the limit $k \to 0$, the two linearly independent solutions (1.12) and (1.13) of the free Schrödinger equation [$V(r) \equiv 0$] are

$$u_m^{(\rm s)}(r) \overset{kr\to 0}{\sim} \frac{\sqrt{\pi}}{\Gamma\left(|m|+1\right)}\left(\frac{kr}{2}\right)^{\frac{1}{2}+|m|}\,, \tag{1.24}$$

and

$$u_{m\neq 0}^{(\rm c)}(r) \overset{kr\to 0}{\sim} -\frac{\Gamma\left(|m|\right)}{\sqrt{\pi}}\left(\frac{kr}{2}\right)^{\frac{1}{2}-|m|}\,, \quad u_{m=0}^{(\rm c)}(r) \overset{kr\to 0}{\sim} \sqrt{\frac{2}{\pi}kr}\left[\ln\left(\frac{kr}{2}\right)+\gamma_{\rm E}\right]\,, \tag{1.25}$$

with Euler's constant $\gamma_{\rm E} = 0.5772156649\ldots$. At threshold, $k = 0$, the regular solution (1.12) has to become a k-independent superposition of the linearly independent threshold solutions $r^{\frac{1}{2}+|m|}$ and $r^{\frac{1}{2}-|m|}$ for $m \neq 0$ and $\sqrt{r}$ and $\sqrt{r}\ln(r)$ for $m = 0$. This

determines the threshold behaviour of the scattering properties. For the s wave ($m = 0$), the threshold behaviour of the scattering phase shift δ_0 for potentials falling off faster than $1/r^2$ is

$$\tan\delta_0 \overset{k\to 0}{\sim} \frac{\pi}{2}\left[\ln\left(\frac{ka}{2}\right)+\gamma_\mathrm{E}\right]^{-1} . \tag{1.26}$$

For $|m| > 0$ and potentials falling off faster than $1/r^{2|m|+2}$ the threshold behaviour is

$$\tan\delta_{m\neq 0} \overset{k\to 0}{\sim} \frac{\pm\pi}{\Gamma(|m|)\Gamma(|m+1|)}\left(\frac{ka_m}{2}\right)^{2|m|} . \tag{1.27}$$

Notice that, in contrast to the scattering in three-dimensions, the scattering length in two dimensions is always non-negative and for $|m| > 0$ the sign in Eq. (1.27) has to be chosen explicitly. The threshold solutions of the radial Schrödinger equation (1.10) asymptotically behave as

$$u_0^{k=0}(r) \overset{r\to\infty}{\propto} \sqrt{r}\ln\left(\frac{r}{a}\right) , \tag{1.28}$$

$$u_{m\neq 0}^{k=0}(r) \overset{r\to\infty}{\propto} \sqrt{r}\left[\left(\frac{r}{a_m}\right)^{|m|} \pm \left(\frac{r}{a_m}\right)^{-|m|}\right] . \tag{1.29}$$

The constants a and a_m are the scattering lengths in the respective partial wave and unambiguously characterise the leading near-threshold behaviour of the scattering phase shift δ_m and the S-matrix S_m. This definition of the scattering length has been introduced by Verhaar *et al.* [44]; alternative definitions [60] of the s-wave scattering length are rather unpractical as they do not cover all contributions of $\mathcal{O}(k^0)$ to $\tan\delta_0$.

For a general scattering process, including inelastic or reactive collisions, the absolute value of S_m is no longer unity and the near-threshold behaviour is expressed by a complex scattering length $\mathfrak{a}$. For potentials falling off faster than $1/r^{2|m|+2}$, the S-matrix is

$$S_{m=0} \overset{k\to 0}{\sim} 1 + \frac{\mathrm{i}\pi}{\ln\left(\frac{k|\mathfrak{a}|}{2}\right)+\gamma_\mathrm{E}+\mathrm{i}\left[\arg(\mathfrak{a})-\frac{\pi}{2}\right]} \tag{1.30}$$

for the s wave and for partial waves with $|m| > 0$,

$$S_{m\neq 0} \overset{k\to 0}{\sim} 1 \pm \frac{2\pi\mathrm{i}}{\Gamma(|m|+1)\Gamma(|m|)}\left(\frac{k\mathfrak{a}_m}{2}\right)^{2|m|} . \tag{1.31}$$

The reflection probability for the s wave $P_R^{(m=0)} = |R_0|^2$ which is directly connected to the S-matrix S_0 thus yields,

$$P_R^{(m=0)} \overset{k\to 0}{\sim} 1 - \frac{-2\pi\arg(\mathfrak{a})}{\left[\ln\left(\frac{k|\mathfrak{a}|}{2}\right)+\gamma_\mathrm{E}\right]^2+\left[\arg(\mathfrak{a})-\frac{\pi}{2}\right]^2} \tag{1.32}$$

for potentials vanishing faster than $1/r^2$. The reflection probability for the s wave reaches unity in the limit $k \to 0$ even for attractive potentials where for $m = 0$ reflection is

classically forbidden due to the absence of a classical turning point. Therefore quantum reflection dominates the scattering in the near-threshold regime of ultracold atoms. For partial waves with $|m| > 0$ the reflection probability still reaches unity at threshold; however, in these cases, reflection would also be allowed in a classical description and would in particular be certain in the limit $k \to 0$ due to the centrifugal barrier.

The near-threshold behaviour of the cross sections is given by the leading contribution of the s wave ($m = 0$). The total elastic cross section is thus given by,

$$\lambda_{\mathrm{el}} \overset{k\to 0}{\sim} \frac{\pi^2/k}{\left[\ln\left(\frac{k|\mathfrak{a}|}{2}\right) + \gamma_{\mathrm{E}}\right]^2 + \left[\arg(\mathfrak{a}) - \frac{\pi}{2}\right]^2} \tag{1.33}$$

and the absorption cross section is

$$\lambda_{\mathrm{abs}} \overset{k\to 0}{\sim} \frac{-2\pi \arg(\mathfrak{a})/k}{\left[\ln\left(\frac{k|\mathfrak{a}|}{2}\right) + \gamma_{\mathrm{E}}\right]^2 + \left[\arg(\mathfrak{a}) - \frac{\pi}{2}\right]^2}\,. \tag{1.34}$$

Both the elastic and absorption cross sections diverge as $1/k$, including additional logarithmic factors. The next-to-leading contribution is of the order k^1 and comes from the next-to-leading order of the s wave and from the leading order of the $|m| = 1$ contributions. Notice that a real-valued scattering length, $\arg(\mathfrak{a}) = 0$, leads to a vanishing absorption cross section.

1.2 The Langevin model

The scattering of an atom by a nanostructure is a highly non-trivial problem. While the interaction potential for large distances is given by the Casimir-Polder interaction (see Chapter 2), the interaction at short distances to the surface of the nanostructure becomes very complicated and remains in general unknown. The interaction of the projectile atom with the individual atoms constituting the nanostructure leads to a variety of inelastic channels and further reactive collision processes (adsorption, sticking, ...) [61–65]. Therefore a reactive or inelastic collision is almost certain and an elastic collision practically impossible in the region close to the surface. Such a scattering process has first been described by Langevin in a classical model [58].

1.2.1 The classical Langevin model

The classical Langevin model [58] was originally developed to describe the scattering of an ion by a neutral molecule. In a classical description of the scattering process there exists a critical impact parameter b_{c} such that trajectories with $b > b_{\mathrm{c}}$ are deflected under the influence of the interaction potential without reaching the scattering centre while trajectories with $b < b_{\mathrm{c}}$ are captured (see Fig. 1.2). At very short distances, both constituents strongly interact and a reaction is practically certain. Then all classical trajectories that enter this region lead to inelastic reactions and contribute to the absorption cross section.

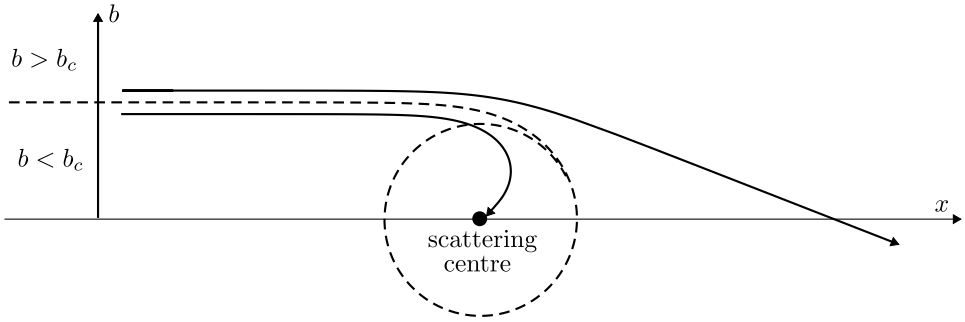

Figure 1.2: Schematic illustration of the classical Langevin model. All trajectories with impact parameters $b < b_c$ are absorbed while all trajectories with $b > b_c$ are elastically scattered. The critical impact parameter b_c is given by the orbiting solution.

Therefore, the classical absorption cross section is[1]

$$\lambda_{\text{abs}}^{\text{class}} = 2b_c \,. \tag{1.35}$$

Although the Langevin model was originally developed for molecule-ion collisions, it is applicable for all collisions that are highly reactive at very short distances between the constituents, such as atoms colliding with nanostructures.

1.2.2 Incoming boundary conditions

In a quantum mechanical description, it is no longer possible to select distinct trajectories that reach the scattering centre. Nevertheless, it is possible to reproduce the Langevin model quantum mechanically.

In the short-range regime where the atom is close to the surface, inelastic reactions are practically certain and impossible for distances beyond the short-range region. In the spirit of the classical Langevin model, all flux entering the reactive short-range region is absorbed by inelastic or reactive collisions. In the elastic channel this results in an absorbing boundary condition. This can be expressed via an inwards travelling wave, giving rise to *incoming boundary condition*; alternative approaches using complex potentials are purely artificial and model-dependent.

Equation (1.18) already showed that the asymptotic ($r \to \infty$) radial solution can be separated into an inwards and outwards travelling plane wave. Typical atom-surface potentials diverge in the region close to the surface and the solution of the Schrödinger equation in this region cannot be expressed by such plane waves. However, an approximate solution to the Schrödinger equation using the WKB approximation – originally developed by Wentzel Kramers and Brillouin [67–69] – provides a wave function with properly defined direction of motion. Therefore, we can express the absorbing boundary conditions by an inwards travelling WKB wave function in the short-range region

$$u_m^{\text{WKB}}(r) \propto \frac{1}{\sqrt{p(r)}} \exp\left[-\frac{\mathrm{i}}{\hbar}\int_{r_0}^{r} p(r')\mathrm{d}r'\right] , \tag{1.36}$$

[1] For detailed discussion see e.g. [58, 66]

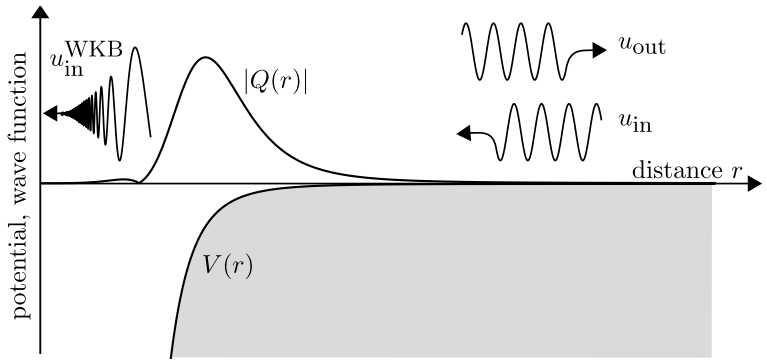

Figure 1.3: Schematic illustration of a scattering process with incoming wave boundary conditions. An attractive interaction potential $V(r)$ (diverging faster than $1/r^2$) gives rise to two regions where $|\mathcal{Q}| \ll 1$, which is sketched for an arbitrary finite energy. In the outer region the elastic scattering solution is given by a superposition of inwards ($u_{\rm in}$) and outwards ($u_{\rm out}$) travelling plane waves [see (1.18)]. In the inner region an inwards travelling WKB wave $u_{\rm in}^{\rm WKB}$ constitutes the absorbing boundary conditions at the surface.

with an in principal arbitrary reference point r_0 and the local classical momentum given by,

$$p(r) = \sqrt{2\mu\left(E - \frac{\hbar^2}{2\mu}\frac{m^2-1/4}{r^2} - V(r)\right)}\,. \tag{1.37}$$

Figure 1.3 shows a schematic illustration of the scattering process with incoming boundary conditions realised via WKB waves (1.36).

The WKB wave function (1.36) is not necessarily an exact solution of the Schrödinger equation (1.10). Explicit evaluation of the second derivative of the WKB wave function (1.36) gives

$$\frac{\mathrm{d}^2}{\mathrm{d}r^2}u_m^{\rm WKB}(r) + \frac{p^2(r)}{\hbar^2}u_m^{\rm WKB}(r) - \left[\frac{3}{4}\frac{\big(p'(r)\big)^2}{p^2(r)} - \frac{p''(r)}{2p(r)}\right]u_m^{\rm WKB}(r) = 0\,. \tag{1.38}$$

Comparing Eq. (1.38) to the radial Schrödinger equation (1.10) gives a reliable criterion for the validity of the WKB approximation. Relation (1.38) resembles the Schrödinger equation (1.10) whenever the third term on the left hand side is small compared to the second term $p(r)^2/\hbar^2$. The ratio of of both term defines the dimensionless *quantality function* [70],

$$\mathcal{Q}(r) = \hbar^2\left(\frac{3}{4}\frac{p'(r)^2}{p(r)^4} - \frac{p''(r)}{2p(r)^3}\right)\,. \tag{1.39}$$

Whenever the absolute value of the quantality function (1.39) becomes small,

$$|\mathcal{Q}(r)| \ll 1\,, \tag{1.40}$$

the exact solution of the Schrödinger equation is accurately approximated by the WKB wave function. The accuracy of the WKB approximation is a local property; the quantality

function allows an identification of spatial regions where the approximation is accurate, see Eq. (1.40), or even exact for $\mathcal{Q}(r) = 0$. For general inverse power potentials

$$V(r) = \pm\frac{\hbar^2}{2\mu}\frac{\beta_\alpha^{\alpha-2}}{r^\alpha}\,, \tag{1.41}$$

the quantality function $\mathcal{Q}(r)$ is

$$\mathcal{Q}(r) \overset{r\to 0}{\sim} \frac{\alpha}{4}\left(1-\frac{\alpha}{4}\right)\left(\frac{r}{\beta_\alpha}\right)^{\alpha-2} \tag{1.42}$$

and vanishes in particular in the limit $r \to 0$ for potentials diverging faster than $1/r^2$ (see Fig. 1.3), which is typical for atom-nanostructure potentials.

Typical length scales of the short-range region where reactive collisions happen are much smaller than the characteristic length β_α of the long-range Casimir-Polder interaction potential, which is typically on the order of several thousand Bohr radii (see Chapter 2). Therefore the quantality function is sufficiently small in this region and an accurate description of the incoming wave boundary conditions via an inwards travelling WKB wave (1.36) is possible. Although the size of the reactive short-range region remains in general unknown, the incoming boundary condition is applicable in the whole short-range region, in particular at $r = 0$. This enables an unambiguous, model-independent description of the short-range interaction of ultracold atoms with nanostructures in the spirit of the classical Langevin model.

Chapter 2

The Atom-Cylinder Potential

The vacuum fluctuations of the electromagnetic field are the origin of various effects like the Lamb shift [71], spontaneous emission [72] but also of the dispersion forces acting between atoms and surfaces of macroscopic or mesoscopic bodies [24]. Calculation and measurements of this Casimir-Polder interaction has attracted considerable attention as it plays an important role in various fields of physics [24, 25, 28, 73, 74].

The interaction of an atom with a cylindrical wire has been studied by various groups during the last decades and is still subject of ongoing research [49, 51, 74]. The first description of the corresponding interaction potential goes back to Zel'dovic [75] who analysed the interaction between an atom and a thin metallic cylinder in 1935. By calculating the interaction potential at large distances, Zel'dovic obtained a $-1/r^4$ behaviour, which differs from the correct result only by logarithmic corrections [48, 76–78]. Further work by Schmeits and Lucas [79] extended the potential to the van der Waals interaction – neglecting retardation effects – between an atom and a dielectric (insulating) cylinder with finite radius. Their ansatz fails as the atom is described in an insufficient two-level model, which has been proven wrong for a perfectly conducting plane [80].

A closed form of the full Casimir-Polder potential between an atom and a dielectric cylinder of radius R was first given by Nabutovskii *et al.* in 1979 [48]. In their approach the interaction energy of a rarefied gas, separated from the cylinder by a shell of vacuum, is calculated via the force due to the fluctuating electromagnetic field, which was given in Ref. [81]. The interaction potential of a single atom is obtained in the limit of zero density of the gas. This result has been confirmed by Marvin and Toigo [76] in 1982 whose ansatz was based on a normal-mode expansion and a linear-response formalism, proposed by Langbein [82]. Further results for the van der Waals potential of a polarisable molecule in front of a dielectric cylinder, neglecting retardation effects were obtained by Boustimi *et al.* [83].

The interaction potential of a polarisable atom in front of a perfectly conducting cylinder, however, differs significantly from the potential of an atom facing a dielectric wire. It has already been noted by Barash and Kyasov that the limit of perfect conductivity does not commute either with the limit of large distances of the atom to the surface of the cylinder or with the limit of a small radius [84]. An accurate calculation of the Casimir-Polder potential of an atom facing a perfectly conducting cylinder has recently been presented by Eberlein and Zietal using a Hamiltonian approach and perfectly reflecting boundary

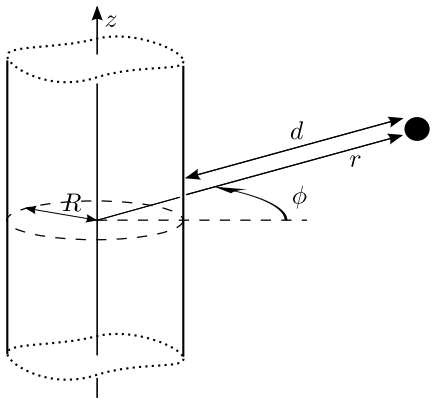

Figure 2.1: Schematic illustration of an atom at distance r from the axis of a cylinder with radius R in cylindrical coordinates r, ϕ, z.

conditions for the fluctuating electromagnetic field [77]. Their result has been confirmed by Bereza *et al.* using a Green's function method to determine the interaction energy [78].

Nevertheless, the potential derived by Nabutovskii *et al.* [48] (and equivalently the result of Marvin and Toigo [76]) is valid also in the perfect-conductor limit and both results [77, 78] can be reproduced by treating the limit of perfect conductivity properly (see Section 2.1). Therefore, the Casimir-Polder potential presented by Nabutovskii *et al.* [48] and later by Marvin and Toigo [76] is the most general one, covering the interaction of an atom with a cylindrical geometry with arbitrary dielectric properties, including the perfectly conducting case of a metallic cylinder.

In this chapter the Casimir-Polder interaction potential for an atom facing a cylindrical geometry is presented. We discuss the behaviour of the interaction potential in its asymptotic limits (Sections 2.1-2.3) and show, how it can accurately be applied to a realistic system (Section 2.4).

Consider an atom located at a distance r from the axis of a cylinder of radius R (see Fig. 2.1). According to the geometry of the system the potential is naturally given in cylindrical coordinates (r, ϕ, z) and depends, due to the rotational symmetry around the cylinder axis (z-axis) and due to the translational invariance along the cylinder axis, on the radial coordinate r only. The Casimir-Polder potential $V(r)$, given in Refs. [48, 76][2], of an atom interacting with a dielectric cylinder of radius R and dielectric constant ϵ in

[2]Note that there is a misprint in the paper of Nabutovskii *et al.*. The last term (underlined) in Eq. (18) of Ref. [48] should read

$$U(r) = -\frac{4T}{\pi r^3}{\sum_{n=0}^{\infty}}' \alpha {\sum_{m=0}^{\infty}}' \int_0^\infty \mathrm{d}x \frac{I_m(z_1)K_m^2(z)}{K_m(z)} \Big\{ \ldots + \underline{4m^2\rho q_1^4 x^2 z_2^2}(\epsilon-1)\Phi_m(z)\left[\Phi_m(z_1) - \Psi_m(z_1)\right] \Big\}. \quad (2.1)$$

This can be verified by the equivalent result calculated by Marvin and Toigo [76].

atomic units is

$$V(r) = -\frac{1}{\pi^2 d^3}\int_0^\infty \mathrm{d}\xi\,\alpha(\mathrm{i}\xi)\sum_{n=-\infty}^{+\infty}\int_0^\infty \mathrm{d}x\,\frac{I_n(z_1)}{\delta_0^0\,K_n(z_1)}K_n^2(\varrho z_1)\Bigg\{q^2\left(\delta_1^0+\delta_0^1\right) + \left(x^2\delta_1^0 - q^2\delta_0^1\right)\left(\frac{n^2}{\varrho^2 z_1^2}+1+\Phi_n^2(\varrho z_1)\right) + 4n^2\varrho^{-1}q_1^4x^2z_2^2(\epsilon-1)\Phi_n(\varrho z_1)\left[\Phi_n(z_1)-\Psi_n(z_1)\right]\Bigg\}, \quad (2.2)$$

where $d = r - R$ is the distance of the atom to the surface of the cylinder. The following abbreviations are used,

$$\varrho = \frac{r}{R}\,, \qquad z_1 = \frac{\sqrt{x^2+q^2}}{\varrho-1}\,, \qquad z_2 = \frac{\sqrt{x^2+\epsilon q^2}}{\varrho-1}\,, \quad (2.3a)$$

$$q = \frac{d}{c}\xi\,, \qquad q_1 = \frac{q}{\varrho-1}\,, \qquad x_1 = \frac{x}{\varrho-1}\,, \quad (2.3b)$$

$$\delta_0^0 = [nx_1q_1^2(\epsilon-1)]^2 + [q_1z_1z_2]^2\,(\Psi_{12}-\Phi_{21})\,(\epsilon\Psi_{12}-\Phi_{21})\,, \quad (2.3c)$$

$$\delta_1^0 = [nx_1q_1^2(\epsilon-1)]^2 + [q_1z_1z_2]^2\,(\Psi_{12}-\Phi_{21})\,(\epsilon\Psi_{12}-\Psi_{21})\,, \quad (2.3d)$$

$$\delta_0^1 = [nx_1q_1^2(\epsilon-1)]^2 + [q_1z_1z_2]^2\,(\Psi_{12}-\Psi_{21})\,(\epsilon\Psi_{12}-\Phi_{21})\,, \quad (2.3e)$$

$$\Psi_n(z) = \frac{\mathrm{d}}{\mathrm{d}z}\ln I_n(z)\,, \qquad \Phi_n(z) = \frac{\mathrm{d}}{\mathrm{d}z}\ln K_n(z)\,, \quad (2.3f)$$

$$\Psi_{ik} = z_i\Psi(z_k)\,, \qquad \Phi_{ik} = z_i\Phi(z_k)\,, \quad (2.3g)$$

with the modified Bessel functions $I_n(z)$ and $K_n(z)$ [59]. The dynamic polarisability $\alpha(\mathrm{i}\xi)$ of the atom can be expressed in terms of atomic dipole transitions [85]. The diagonal components of an atomic or molecular polarisability are given by

$$\alpha_{\nu\nu}(\mathrm{i}\xi) = 2\sum_{j\neq i}\frac{E_{ji}\left|\langle i|\hat{d}_\nu|j\rangle\right|^2}{E_{ji}^2+\xi^2} \quad (2.4)$$

where $|i\rangle$ is the internal state of the atom with energy E_i, $\hat{d}_\nu$ are the components of the dipole operator and $E_{ji} = E_j - E_i$ is the transition energy. In the present case we refer to a spherical atomic state where the three components are equal, $\alpha_{rr} = \alpha_{\phi\phi} = \alpha_{zz} \equiv \alpha$.

2.1 The limit of a perfect conductor

It was already shown by Barash and Kyasov [84] that the Casimir-Polder potential of an atom facing an insulating, dielectric cylinder differs significantly from the interaction potential of a metallic, perfectly conducting wire. The latter case, where $\epsilon \to \infty$, requires a separate treatment because the perfect-conductor limit does not commute with the limit of large atom-surface separations.

Nevertheless, the full potential in [48] is valid for a perfectly conducting cylinder, as long as the limit $\epsilon \to \infty$ is treated properly. Taking the perfect-conductor limit first, we avoid these problems (see Ref. [84]) and we find

$$\delta_1^0/\delta_0^0 \overset{\epsilon\to\infty}{\longrightarrow} 1\,, \qquad\qquad \delta_0^1/\delta_0^0 \overset{\epsilon\to\infty}{\longrightarrow} \frac{\Psi(z_1)}{\Phi(z_1)}\,. \tag{2.5}$$

The last term in Eq. (2.2) is of $\mathcal{O}(\epsilon^{-1/2})$ and vanishes for $\epsilon \to \infty$; the full potential (2.2) reduces to

$$V^{\epsilon\to\infty}(r) = -\frac{1}{\pi^2 d^3}\int_0^\infty \mathrm{d}\xi\alpha(\mathrm{i}\xi)\sum_{n=-\infty}^{+\infty}\int_0^\infty \mathrm{d}x\Bigg\{\left(q^2+\frac{x^2n^2}{\varrho^2 z_1^2}+x^2\right)\frac{I_n(z_1)}{K_n(z_1)}K_n^2(\varrho z_1)$$
$$-\,q^2\frac{n^2}{\varrho^2 z_1^2}\frac{I_n'(z_1)}{K_n'(z_1)}K_n^2(\varrho z_1) - q^2\frac{I_n'(z_1)}{K_n'(z_1)}K_n^{'2}(\varrho z_1) + x^2\frac{I_n(z_1)}{K_m(z_1)}K_m^{'2}(\varrho z_1)\Bigg\}. \tag{2.6}$$

Expressing the dynamic polarisability via Eq. (2.4) and changing the integration variables to polar coordinates z and ϕ with $x = z\sin\phi$ and $q = z\cos\phi$, where the angular integrals are elementary

$$\int_0^{\pi/2}\mathrm{d}\phi\frac{B}{B^2+\cos^2\phi} = \frac{\pi}{2}\frac{1}{\sqrt{B^2+1}}\,, \tag{2.7}$$

$$\int_0^{\pi/2}\mathrm{d}\phi\frac{B\cos^2\phi}{B^2+\cos^2\phi} = -\frac{\pi}{2}\left(\frac{B^2}{\sqrt{B^2+1}}-B\right), \tag{2.8}$$

$$\int_0^{\pi/2}\mathrm{d}\phi\frac{B\sin^2\phi}{B^2+\cos^2\phi} = \frac{\pi}{2}\left(\sqrt{B^2+1}-B\right), \tag{2.9}$$

Eq. (2.6) yields

$$V^{\epsilon\to\infty}(r) = -\frac{1}{3\pi d^3}\sum_{j\neq i}\sum_{n=-\infty}^{+\infty}\int_0^\infty \mathrm{d}z\, z\left|\langle i|\hat{\boldsymbol{d}}|j\rangle\right|^2\Bigg\{\frac{z^2}{\sqrt{(E_{ji}d/c)^2+z^2}}\frac{I_n(z_1)}{K_n(z_1)}K_n^2(\varrho z_1)$$
$$+\frac{n^2}{\varrho^2 z_1^2}\left[\sqrt{(E_{ji}d/c)^2+z^2}-(E_{ji}d/c)\right]\frac{I_n(z_1)}{K_n(z_1)}K_n^2(\varrho z_1)$$
$$+\frac{n^2}{\varrho^2 z_1^2}\left[\frac{(E_{ji}d/c)^2}{\sqrt{(E_{ji}d/c)^2+z^2}}-(E_{ji}d/c)\right]\frac{I_n'(z_1)}{K_m' n(z_1)}K_n^2(\varrho z_1)$$
$$+z\left[\frac{(E_{ji}d/c)^2}{\sqrt{(E_{ji}d/c)^2+z^2}}-(E_{ji}d/c)\right]\frac{I_n'(z_1)}{K_n'(z_1)}K_n^{'2}(\varrho z_1)$$
$$+z\left[\sqrt{(E_{ji}d/c)^2+z^2}-(E_{ji}d/c)\right]\frac{I_n(z_1)}{K_n(z_1)}K_n^{'2}(\varrho z_1)\Bigg\}, \tag{2.10}$$

with $z_1 = z/(\varrho-1)$ according to (2.3). This result is equivalent to the one obtained by Eberlein and Zietal in Eq. (17) of Ref. [77] and the potential calculated by Bezerra *et al.*, see Eq. (23) of Ref. [78]. The potential in Ref. [77] is obtained using a Hamiltonian approach and calculating the interaction between a single atom and the fluctuating electromagnetic field by second-order perturbation theory. The perfect conductivity is taken

into account by perfectly reflecting boundary conditions for the electromagnetic field at the surface of the cylinder. The result in Ref. [78] is obtained via a Green's function method leading to the same result. Notice that in [77] the international system of units is used, while this work refers to atomic units.

There are basically two timescales in the system, the time $T_{ji} = \hbar/E_{ji}$ associated with the atomic transition $|i\rangle \to |j\rangle$ and the mediation time $T_\gamma = 2d/c$ it takes a virtual photon, mediating the interaction, to travel from the atom to the surface and back. If $T_\gamma \ll T_{ji}$ for all contributing transitions, the interaction is entirely electrostatic. While, for $T_\gamma \approx T_{ji}$ or larger, retardation begins to play a role and the evolution of the internal state of the atom during the exchange of a virtual photon is not negligible. According to these timescales, we can identify two limits of the interaction; namely the *non-retarded* (nr) or van der Waals limit, where $T_\gamma \ll T_{ji}$ and the *highly retarded* (hr) limit (sometimes called the retarded or Casimir-Polder limit), where $T_\gamma \gg T_{ji}$.

2.2 The non-retarded or van der Waals limit

In the non-retarded or van der Waals limit the interaction is entirely electrostatic. The electrostatic interaction is instantaneous and retardation effects due to the finite mediation time T_γ are negligible. Therefore, the non-retarded limit in the atom-cylinder potential (2.2) is obtained in the limit $T_\gamma = 2d/c \to 0$, which enters the Casimir-Polder potential (2.2) via Eq. (2.3b), where $q \to 0$. In this limit Eq. (2.3) reduces to

$$z_1 \overset{q\to 0}{\sim} x_1\,, \qquad z_2 \overset{q\to 0}{\sim} x_1 \tag{2.11a}$$

$$\delta_1^0/\delta_0^0 \overset{q\to 0}{\sim} \frac{\Psi_{21} - \epsilon\Psi_{12}}{\Phi_{21} - \epsilon\Psi_{12}}\,, \qquad \delta_0^1/\delta_0^0 \overset{q\to 0}{\sim} \frac{\Psi_{21} - \Psi_{12}}{\Phi_{21} - \Psi_{12}}\,, \tag{2.11b}$$

$$\Psi_{12} \overset{q\to 0}{\sim} \Psi_{21}\,, \qquad \Phi_{12} \overset{q\to 0}{\sim} \Phi_{21}\,. \tag{2.11c}$$

The last term in (2.2) is of $\mathcal{O}(q^2)$ and vanishes in the limit $q \to 0$. In the non-retarded limit the atom-cylinder potential in Eq. (2.2) thus is (see also Eq. (22) of Ref. [48])

$$V(r) \overset{q\to 0}{\sim} -\frac{(\epsilon-1)}{\pi^2 d^3}\int_0^\infty \mathrm{d}\xi\alpha(\mathrm{i}\xi)\sum_{n=-\infty}^{+\infty}\int_0^\infty \mathrm{d}x\, x^2\left[\epsilon\frac{K_n(x_1)}{I_n(x_1)} - \frac{K_n'(x_1)}{I_n'(x_1)}\right]^{-1}\times \left[K_n^{'2}(\varrho x_1) + \left(\frac{n^2}{\varrho^2 x_1^2}+1\right)K_n^2(\varrho x_1)\right]. \tag{2.12}$$

This result is equivalent to the potential calculated by Bustimi *et al.* [83] (see Eq. (13) of Ref. [83] with $\alpha_{xx} = \alpha_{yy} = \alpha_{zz} = \alpha(\mathrm{i}\xi)$ and $\alpha_{xy} = 0$) who calculated the potential of a polarisable molecule in front of a dielectric cylinder in the van der Waals limit using a linear response ansatz.

The potential further simplifies as the integral over the dynamic polarisability $\alpha(\mathrm{i}\xi)$ reduces to

$$\frac{1}{\pi}\int_0^\infty \mathrm{d}\xi\alpha(\mathrm{i}\xi) = \frac{1}{3}\langle\hat{\boldsymbol{d}}^2\rangle\,, \tag{2.13}$$

Table 2.1: Expectation value of the squared dipole-operator $\langle \hat{\boldsymbol{d}}^2 \rangle$ and characteristic length $\beta_{\rm nr}$ of the atom-wire interaction in the non-retarded limit as defined in Eq. (2.16).

Atom	H [a]	He [b,c]	He(2^1S) [d]	He(2^3S) [d]	Li [b,e]	Na [f,g]	K [g]	Rb [g]	Cs [g]
$\langle \hat{\boldsymbol{d}}^2 \rangle$ [a.u.]	3	2.256	32.04	22.8	18.21	22.68	34.32	40.32	49.68
$\beta_{\rm nr}/10^3$ [a.u.]	3.67	11.0	156	111	154	633	1630	4190	8018

From Refs. [a][85]; [b][86]; [c][87]; [d][88]; [e][89]; [f][90]; [g][91]

where $\langle \hat{\boldsymbol{d}}^2 \rangle$ is the expectation value of the squared dipole-operator $\hat{\boldsymbol{d}}^2$. The potential $V_{\rm nr}(r)$ of an atom interacting with a cylinder in the non-retarded or van der Waals limit is thus

$$V_{\rm nr}(r) = -\frac{\hbar^2}{2\mu}\frac{\beta_{\rm nr}}{d^3}\frac{(\epsilon-1)}{\pi}\sum_{n=-\infty}^{+\infty}\int_0^\infty \mathrm{d}x\, x^2 \left[\epsilon\frac{K_n(x_1)}{I_n(x_1)} - \frac{K_n'(x_1)}{I_n'(x_1)}\right]^{-1} \times \left[K_n^{'\,2}(\varrho x_1) + \left(\frac{n^2}{\varrho^2 x_1^2}+1\right)K_n^2(\varrho x_1)\right] . \quad (2.14)$$

The non-retarded potential of an atom interacting with a metallic cylinder is obtained either from Eq. (2.14) by taking the perfect-conductor limit, $\epsilon \to \infty$, or from Eq. (2.10) by taking the limit $d/c \to 0$, which in both cases gives (see also Ref. [92])

$$V_{\rm nr}^{\epsilon\to\infty}(r) = -\frac{\hbar^2}{2\mu}\frac{\beta_{\rm nr}}{\pi d^3}\sum_{n=-\infty}^{+\infty}\int_0^\infty \mathrm{d}x\, x^2 \frac{I_n(x_1)}{K_n(x_1)}\left[K_n^{'\,2}(\varrho x_1) + \left(\frac{n^2}{\varrho^2 x_1^2}+1\right)K_n^2(\varrho x_1)\right] , \quad (2.15)$$

with the characteristic length $\beta_{\rm nr}$ related to the expectation value of the squared dipole-operator of the atom

$$\beta_{\rm nr} = \frac{2\mu}{\hbar^2}\frac{\langle \hat{\boldsymbol{d}}^2 \rangle}{3} . \quad (2.16)$$

The characteristic length $\beta_{\rm nr}$ is typically quite large, since $\langle \hat{\boldsymbol{d}}^2 \rangle$ is usually of the order of a few atomic units and the mass μ of the atom, in atomic units, is quite large. Table 2.1 lists, as examples, explicit values of the expectation value of the squared dipole-operator $\langle \hat{\boldsymbol{d}}^2 \rangle$ and the characteristic length $\beta_{\rm nr}$ for hydrogen and several alkali atoms in their respective ground state and helium in its ground or metastable $2S$ state. Values of $\beta_{\rm nr}$ range from a few thousand to several million Bohr radii.

An explicit evaluation of the atom-cylinder potential (2.14) in the non-retarded limit is difficult and requires a sophisticated treatment in order to reproduce the correct behaviour of the non-retarded potential for all atom-surface separations. An accurate approximation method that enables an explicit evaluation of the potential by truncating the infinite sum in Eq. (2.14) to a finite range from $-n_{\rm max}$ to $+n_{\rm max}$ and including the residual terms approximately, is presented in Appendix A.1.

The interaction potential (2.14) of an atom facing a dielectric or metallic cylinder in the non-retarded limit has in general a quite complicated form. However, it can be substantially simplified in the asymptotic limits of small and large distances of the atom to the surface of the cylinder.

2.2.1 Asymptotic behaviour at small atom-surface separations

Close to the surface of the cylinder, $d/R \to 0$, each term of the sum in Eq. (2.14) is of $\mathcal{O}(d/R)$ and contributes equally. By including all terms properly via an accurate approximation, as presented in Appendix A.1, we obtain the well-known result [26] for the non-retarded van der Waals potential of an atom in front of a plane conducting surface

$$V_{\mathrm{nr}}^{\epsilon\to\infty}(r) \overset{d/R\to 0}{\sim} -\frac{C_3(\infty)}{d^3}, \quad \text{with} \quad C_3(\infty) = \frac{1}{12}\langle \hat{\boldsymbol{d}}^2 \rangle , \tag{2.17}$$

and for a finite value of the dielectric constant,

$$V_{\mathrm{nr}}(r) \overset{d/R\to 0}{\sim} -\frac{C_3(\epsilon)}{d^3}, \quad \text{with} \quad C_3(\epsilon) = \frac{\epsilon-1}{\epsilon+1} C_3(\infty) . \tag{2.18}$$

Notice that this behaviour can only be obtained by treating the potential properly, as it is shown in Appendix A.1. This is particularly important in the context of the Langevin model where a description via incoming boundary conditions requires a potential vanishing faster than $1/d^2$ for $d \to 0$ (see Section 1.2); this is only guaranteed within an accurate treatment and violated by simple truncation methods (see Appendix A.1).

2.2.2 Asymptotic behaviour at large atom-surface separations

For large atom-surface separations, $d/R \to \infty$, the leading contribution to the non-retarded potential (2.14) for a dielectric cylinder differs substantially from the long-range asymptote (2.10) of the non-retarded potential of a metallic wire. In the latter case, the leading contribution to the potential (2.10) is given solely by the $n = 0$ term which is proportional to $1/(r^3 \ln \varrho)$ for large values of ϱ,

$$V_{\mathrm{nr}}^{\epsilon\to\infty}(r \to \infty) \overset{d/R\to\infty}{\sim} -\frac{\hbar^2}{2\mu}\frac{\pi}{8}\frac{\beta_{\mathrm{nr}}}{r^3 \ln(r/R)} . \tag{2.19}$$

This leading behaviour is, however, not very helpful, as the next-to-leading terms differ only through additional factors of $1/\ln \varrho$ and such logarithmic series converge very slowly [42, 92]. The deviations of the exact potential from its long-range asymptote are $> 1\%$ even for distances d on the order of several millions of cylinder-radii R.

Figure 2.2 shows the asymptotic behaviour of the non-retarded atom-cylinder potential (2.15) at small and large atom-surface separations for a perfectly conducting cylinder. For small distances of the atom to the surface of the cylinder, $d \ll R$, the non-retarded potential (green solid line) is well described by the asymptotic expression given in Eq. (2.17), shown by the black dashed line. The asymptotic behaviour (2.19) at large distances (black dot-dashed line) remains a poor description in the whole range up to $d/R = 50$.

The long-range behaviour of the non-retarded potential of a dielectric cylinder (2.14) is given both by the $n = 0$ and $|n| = 1$ terms in the sum, which are of $\mathcal{O}(1/\varrho^2)$ in this

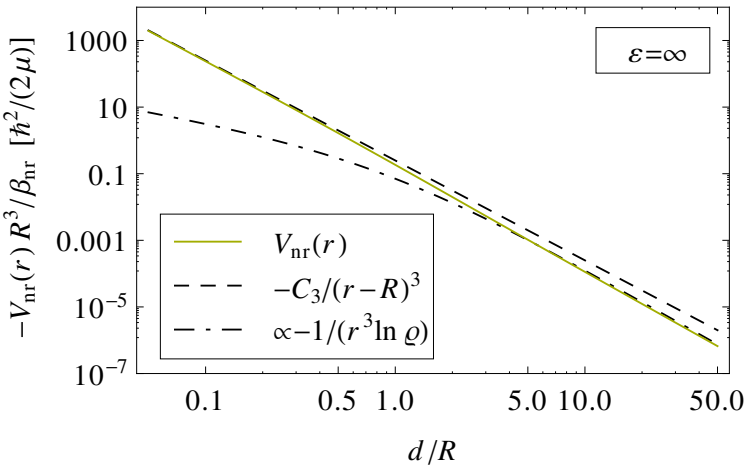

Figure 2.2: Asymptotic behaviour of the non-retarded atom-cylinder potential at small and large atom-surface separations for an atom facing a perfectly conducting cylinder. The green solid line shows the non-retarded potential (2.15); the black dashed line shows the behaviour of the potential close to the surface, given in Eq. (2.17) and the black dot-dashed line shows the behaviour of the non-retarded potential at large atom-surface separations, given in Eq. (2.19). The deviations of the exact result from the long-range behaviour are $> 1\%$ in the whole range of values d/R. Notice that $V_{\rm nr}(r)R^3/\beta_{\rm nr}$ depends on the dimensionless ratio d/R only.

case. By retaining only these terms in Eq. (2.14), the leading behaviour a large distances yields

$$V_{\rm nr}(d) \overset{d/R\to\infty}{\sim} -\frac{\hbar^2}{2\mu}\frac{9\pi}{128}\frac{(\epsilon-1)(\epsilon+7)}{\epsilon+1}\frac{\beta_{\rm nr}R^2}{r^5}\,. \tag{2.20}$$

This asymptotic inverse power potential was already obtained in Refs. [48, 84] and provides, in contrast to the case of perfect conductivity, a useful approximation of the potential, which is essentially indistinguishable from its long-range asymptote already for distances $d/R \gtrsim 10$, see Fig. 2.3. However, Eq. (2.20) fails to reproduce the correct asymptotic behaviour in the limit of perfect conductivity, $\epsilon \to \infty$, as the limit of large atom-surface separations $d/R \to \infty$, and the limit of perfect conductivity, $\epsilon \to \infty$, do not commute. For that reason Eq. (2.20) is only applicable for a finite value of the dielectric constant ϵ.

Figure 2.3 shows the asymptotic behaviour of the non-retarded atom-cylinder potential (2.14) at small and large atom-surface separations for a dielectric cylinder. The dielectric constant is chosen to be $\epsilon = 5$; qualitatively similar results are obtained for other dielectric constants. For small distances of the atom to the surface of the cylinder, $d \ll R$, the non-retarded potential (green solid line) is well described by the asymptotic expression given in Eq. (2.18), shown by the black dashed line. Far away from the cylinder $d \gg R$ the potential reaches its long-range asymptote (2.20), shown by the black dot-dashed line. In the transition region where $d \approx R$, the non-retarded potential shows a smooth but non-trivial transition between both asymptotic limits.

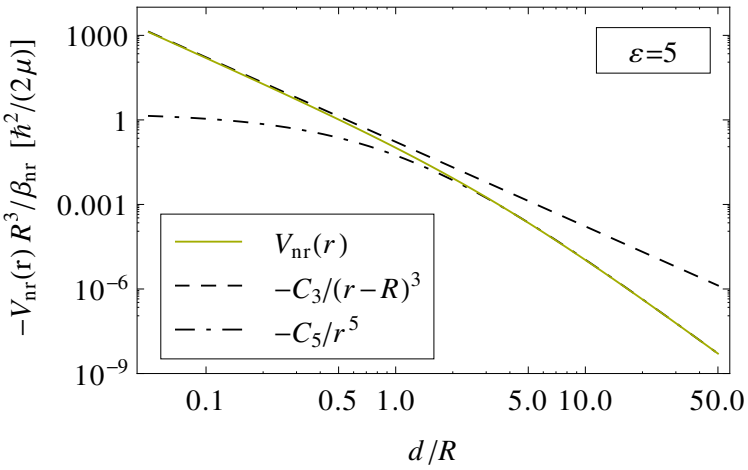

Figure 2.3: Asymptotic behaviour of the non-retarded atom-cylinder potential at small and large atom-surface separations for an atom facing a cylinder with dielectric constant $\epsilon = 5$. The green solid line shows the non-retarded potential (2.14); the black dashed line shows the behaviour of the potential close to the surface, given in Eq. (2.18), and the black dot-dashed line shows the behaviour of the non-retarded potential at large atom-surface separations, given in Eq. (2.20). Notice that $V_{\rm nr}(r)R^3/\beta_{\rm nr}$ depends on the dimensionless ratio d/R only.

2.3 The highly retarded limit

In the highly retarded limit – sometimes also called the retarded or the Casimir-Polder limit – the finite mediation time T_γ, it takes a virtual photon to travel to the surface and back, is non-negligible and thus the interaction is affected or even dominated by retardation effects. Compared to the mediation time T_γ, the characteristic times $T_{ji} = \hbar/E_{ji}$ of all contributing atomic transitions are small and thus the highly retarded limit is obtained in the limit $T_{ji} \to 0$, or equivalently $E_{ji} \to \infty$. Therefore, the dynamic polarisability, given in Eq. (2.4) reduces to

$$\alpha(\mathrm{i}\xi) = 2\sum_{j\neq i} \frac{E_{ji}\left|\langle i|\hat{d}_\nu|j\rangle\right|^2}{E_{ji}^2+\xi^2} \overset{E_{ji}\to\infty}{\sim} 2\sum_{j\neq i} \frac{\left|\langle i|\hat{d}_\nu|j\rangle\right|^2}{E_{ji}} = \alpha_{\rm d}\,. \tag{2.21}$$

where $\alpha_{\rm d}$ is the static dipole-polarisability of the atom. By changing the integration variable to $q = d/c\,\xi$, the atom-cylinder potential in the highly retarded limit is,

$$\begin{aligned} V(r) = -\frac{\hbar^2}{2\mu}\frac{2\beta_{\rm hr}^2}{\pi^2 d^4}\sum_{n=-\infty}^{+\infty}\int_0^\infty \mathrm{d}q \int_0^\infty \mathrm{d}x\, \frac{I_n(z_1)}{\delta_0^0\, K_n(z_1)} K_n^2(\varrho z_1)\Bigg\{ & q^2\left(\delta_1^0+\delta_0^1\right) \\ & + \left(x^2\delta_1^0 - q^2\delta_0^1\right)\left(\frac{n^2}{\varrho^2 z_1^2}+1+\Phi_n^2(\varrho z_1)\right) \\ & + 4n^2\varrho^{-1}q_1^4 x^2 z_2^2(\epsilon-1)\Phi_n(\varrho z_1)\left[\Phi_n(z_1)-\Psi_n(z_1)\right]\Bigg\}. \end{aligned} \tag{2.22}$$

Table 2.2: Static dipole polarisability α_d and characteristic length β_hr of the atom-wire interaction in the highly retarded limit as defined in Eq. (2.24).

Atom	H [a]	He [b,c]	He(2^1S) [d]	He(2^3S) [d]	Li [b,e]	Na [f,g]	K [g]	Rb [g]	Cs [g]
α_d [a.u.]	4.5	1.38	800	316	164	163	290	318	401
$\beta_\mathrm{hr}/10^3$ [a.u.]	1.06	1.17	28.3	17.8	16.9	30.6	53.2	82.4	115

From Refs. [a][85]; [b][86]; [c][87]; [d][88]; [e][89]; [f][90]; [g][91]

The highly retarded limit of the atom-cylinder potential in the perfect-conductor limit is obtained from Eq. (2.10) in the limit $T_\gamma = 2d/c \to \infty$ or equivalently from Eq. (2.22) by taking the limit $\epsilon \to \infty$, which allows further simplifications. Both procedures lead to

$$V_\mathrm{hr}^{\epsilon\to\infty}(r) = -\frac{\hbar^2}{2\mu}\frac{\beta_\mathrm{hr}^2}{2\pi d^4}\sum_{n=-\infty}^{+\infty}\int_0^\infty \mathrm{d}z\, z^3 \Bigg\{ \frac{I_n(z_1)}{K_n(z_1)}\left[K_n'^{\,2}(\varrho z_1) + \left(\frac{n^2}{\varrho^2 z_1^2}+2\right)K_n^2(\varrho z_1)\right] - \frac{I_n'(z_1)}{K_n'(z_1)}\left[K_n'^{\,2}(\varrho z_1) + \frac{n^2}{\varrho^2 z_1^2}K_n^2(\varrho z_1)\right]\Bigg\}, \quad (2.23)$$

with the characteristic length of the highly retarded atom-cylinder potential,

$$\beta_\mathrm{hr} = \sqrt{\frac{2\mu}{\hbar^2}\frac{\alpha_\mathrm{d}}{2\alpha_\mathrm{fs}}}, \quad (2.24)$$

which is related to the static dipole-polarisability α_d and to the fine structure constant $\alpha_\mathrm{fs} = e^2/(\hbar c)$. Table 2.2 lists explicit values of the static dipole-polarisability α_d and of the characteristic length β_hr for hydrogen, several alkali atoms in their respective ground state and helium in its ground or metastable $2S$ state. Typical values of β_hr are large (in atomic units) and range from few to several thousand Bohr radii, but they are usually smaller than the corresponding length in the non-retarded limit β_nr (see Tab. 2.1).

In contrast to the non-retarded limit, discussed in Section 2.2, the potential in the highly retarded limit (2.22) allows no further simplifications. However, the remaining two integrals can be evaluated numerically, as the the dynamic polarisability $\alpha(i\xi)$ – depending on all atomic dipole transitions, which are in general unknown, and preclude an explicit evaluation of Eq. (2.2) – has reduced to α_d, which is a well-known property of the atom. An explicit evaluation of the highly retarded potential in Eq. (2.22) remains difficult and requires an accurate treatment similar to that of the non-retarded case. Appendix A.2 shows an accurate and practicable approximation based on a truncation of the infinite sum in Eq. (2.22) and an approximate treatment of the residual terms.

The highly retarded limit of the atom-cylinder potential (2.22), which is in general very complicated, simplifies in the asymptotic limits of large and small separations of the atom to the surface of the cylinder.

2.3.1 Asymptotic behaviour at small atom-surface separations

The behaviour of the potential close to the surface is obtained by treating Eq. (2.22) accurately as shown in Appendix A.2, which includes contributions of all terms in Eq. (2.22) – at least approximately. Close to the surface of the cylinder, $d/R \to 0$, we obtain the well-known interaction of an atom facing a plane conducting surface in the highly retarded limit as first described by Casimir and Polder in 1948 [23],

$$V_{\rm hr}(r) \overset{d/R\to 0}{\sim} -\frac{C_4(\infty)}{d^4}\,, \quad \text{with} \quad C_4(\infty) = \frac{3}{8\pi}\frac{\alpha_{\rm d}}{\alpha_{\rm fs}}\,. \tag{2.25}$$

For a finite value of the dielectric constant we find [88, 89],

$$V_{\rm hr}(r) \overset{d/R\to 0}{\sim} -\frac{C_4(\epsilon)}{d^4}\,, \quad \text{with} \quad C_4(\epsilon) = \frac{\epsilon-1}{\epsilon+1}\,\Phi(\epsilon)\,C_4(\infty)\,. \tag{2.26}$$

The function $\Phi(\epsilon)$ is a smooth and well-defined function of the dielectric constant ϵ,

$$\Phi(\epsilon) = \frac{1}{2}\frac{\epsilon+1}{\epsilon-1}\int_1^\infty H(p,\epsilon)p^{-4}\,{\rm d}p \tag{2.27}$$

where

$$H(p,\epsilon) = \frac{s-p}{s+p} + \frac{s-\epsilon p}{s+\epsilon p}(1-2p^2)\,, \quad \text{with} \quad s = (\epsilon - 1 + p^2)^{1/2}\,, \tag{2.28}$$

and which is 23/30 for $\epsilon = 1$ and unity for $\epsilon \to \infty$

2.3.2 Asymptotic behaviour at large atom-surface separations

For distances much larger than the radius of the cylinder, $d/R \to \infty$, the highly retarded atom-cylinder potential shows a significantly different behaviour for a cylinder with finite dielectric constant and for a perfectly conducting wire. The long-range behaviour of the atom-cylinder potential (2.23) for a perfectly conducting cylinder is given by the $n = 0$ term only, which is asymptotically proportional to $1/(r^4 \ln \varrho)$ in the limit of large ϱ,

$$V_{\rm hr}^{\epsilon\to\infty}(r) \overset{d/R\to 0}{\sim} -\frac{\hbar^2}{2\mu}\frac{2}{3\pi}\frac{\beta_{\rm hr}^2}{r^4\ln(r/R)}\,. \tag{2.29}$$

Similar to the non-retarded case, this leading behaviour is not very helpful and differs from next-to-leading terms only by additional logarithmic factors $1/\ln\varrho$. This logarithmic series converges slowly [42, 92] and deviations of Eq. (2.23) from its asymptotic behaviour are $> 1\%$ even for large distances up to $d/R \lesssim 1000$.

Figure 2.2 shows the highly retarded potential (2.23) of an atom facing a perfectly conducting cylinder (blue solid line) as well as the asymptotic behaviour at small (black dashed line) and large (black dot-dashed line) atom-surface separations. While the potential is well-described by its asymptotic behaviour at short distances, the convergence to the long-range asymptote remains poor.

In contrast to the perfectly conducting cylinder, the leading contribution of the potential for an insulating wire with a finite dielectric constant is given both by the terms with $n = 0$ and $|n| = 1$ in Eq. (2.22). Retaining these terms only, gives

$$V_{\rm hr}(d) \overset{d/R\to\infty}{\sim} -\frac{\hbar^2}{2\mu}\frac{2}{15\pi}\frac{(\epsilon-1)(7\epsilon+39)}{\epsilon+1}\frac{\beta_{\rm hr}^2 R^2}{r^6}\,. \tag{2.30}$$

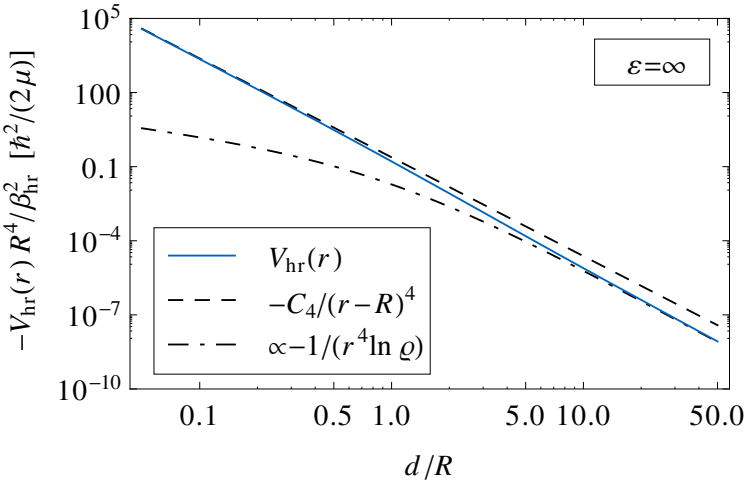

Figure 2.4: Asymptotic behaviour of the highly retarded atom-cylinder potential at small and large atom-surface separations for an atom facing a perfectly conducting cylinder. The blue solid line shows the highly retarded potential (2.23); the black dashed line shows the behaviour of the potential close to the surface, given in Eq. (2.25) and the black dot-dashed line shows the behaviour of the highly retarded potential at large atom-surface separations, given in Eq. (2.29). Notice that $V_{\rm hr}(r)R^4/\beta_{\rm hr}^2$ depends on the dimensionless ratio d/R only.

This long-range inverse-power behaviour, which was also obtained in Refs. [48, 84], accurately approximates the highly retarded potential, which deviates less than 1% from its long-range asymptote already for $d/R \gtrsim 10$. Similar to the non-retarded limit of the Casimir-Polder potential, the long-range behaviour (2.30) for a dielectric cylinder fails, for $\epsilon \to \infty$, to reproduce the potential (2.29) obtained for a perfectly conducting wire, and is thus only applicable to a cylinder with finite dielectric constant ϵ.

Figure 2.5 shows the asymptotic behaviour of the highly retarded atom-cylinder potential (2.22) at small and large atom-surface separations for a cylinder with dielectric constant $\epsilon = 5$; qualitatively similar results are obtained for different values of ϵ. For small distances of the atom to the surface of the cylinder, $d \ll R$, the highly retarded potential (blue solid line) is well described by the asymptotic expression (black dashed line) given in Eq. (2.26). The highly retarded potential reaches its long-range asymptote (black dot-dashed line), given in Eq. (2.30) for $d \gg R$ and shows a smooth but non-trivial transition in between both asymptotic limits in the region where $d \approx R$.

2.4 Realistic atom-cylinder potential

The non-retarded and the highly retarded limit of the Casimir-Polder potential, which have been discussed in the previous sections, are related to the mediation time T_γ, it takes a virtual photon to travel to the surface and back, and to the times T_{ji} of the contributing atomic transitions. In the non-retarded limit the mediation time T_γ is negligible ($T_\gamma \ll T_{ji}$) and $T_\gamma \gg T_{ji}$ constitutes the highly retarded limit. The mediation time T_γ of

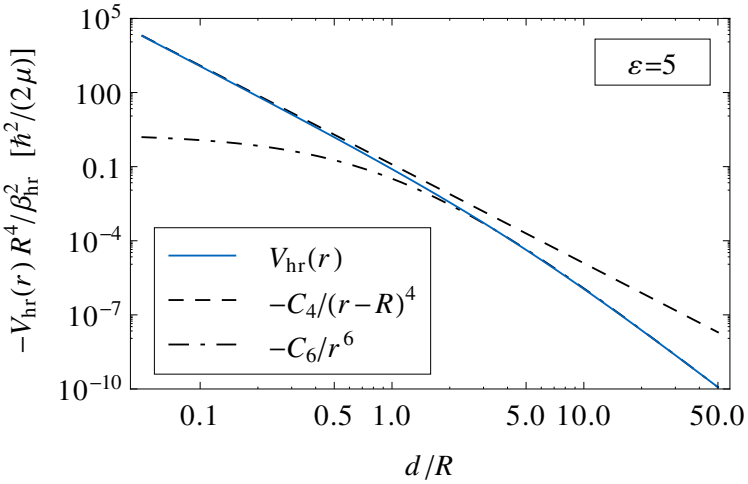

Figure 2.5: Asymptotic behaviour of the highly retarded atom-cylinder potential at small and large atom-surface separations for an atom facing a cylinder with dielectric constant $\epsilon = 5$. The blue solid line shows the highly retarded potential (2.22); the black dashed line shows the behaviour of the potential close to the surface, given in Eq. (2.26), and the black dot-dashed line shows the behaviour of the highly retarded potential at large atom-surface separations, given in Eq. (2.30). Notice that $V_{\rm hr}(r)R^4/\beta_{\rm hr}^2$ depends on the dimensionless ratio d/R only.

the interaction is connected to the distance of the atom to the surface of the cylinder via $T_\gamma = 2d/c$. Thus, in a realistic scenario the Casimir-Polder interaction potential reaches its non-retarded or van der Waals limit at small distances, $d \to 0$, and its highly retarded limit at large distances, $d \to \infty$. In the *transition zone* in between the non-retarded and highly retarded regime, the Casimir-Polder potential undergoes a smooth but non-trivial transition.

In the limit of large radii, $R \gg d$, where the potential is given by Eqs. (2.18) and (2.26) in the non-retarded and in the highly retarded limit, the full potential contains an intrinsic length

$$L(\epsilon) = \frac{C_4(\epsilon)}{C_3(\epsilon)} = \frac{3}{\pi}\frac{\beta_{\rm hr}^2}{\beta_{\rm nr}}\Phi(\epsilon)\,. \tag{2.31}$$

which separates the non-retarded region of small distances, $d \ll L$, from the highly retarded region of large distances, $d \gg L$. This length scale was first introduced by Friedrich *et al.* for the interaction of atoms with a flat surface [27]. A characteristic length for this transition zone in the case of a thin ($R \ll d$) metallic cylinder can be obtained similarly from Eqs. (2.19) and (2.29),

$$L'_{\epsilon\to\infty} = \frac{16}{3\pi^2}\frac{\beta_{\rm hr}^2}{\beta_{\rm nr}} = \frac{16}{9\pi}L(\infty)\,. \tag{2.32}$$

For a cylinder with a finite dielectric constant, the non-retarded and highly retarded limit of the potentials behave as C_5/r^5 and C_6/r^6, in the limit of small radii, $R \ll d$. A

Table 2.3: Characteristic lengths L and $L'_{\epsilon\to\infty}$ of the transition zone for a perfectly conducting tube and a cylinder with a dielectric constant $\epsilon = 5$, given in Eqs. (2.31) - (2.33) as well as the characteristic ratio $\rho = \beta_{\rm nr}/\beta_{\rm hr}$.

Atom	H	He	He(2^1S)	He(2^3S)	Li	Na	K	Rb	Cs
$L(\infty)$ [a.u.]	294	120	4903	2717	1768	1411	1659	1548	1584
$L'_{\epsilon\to\infty}$ [a.u.]	167	68	2775	1538	1000	798	939	876	897
$L(\epsilon = 5)$ [a.u.]	229	93	3806	2109	1372	1095	1287	1202	1230
$L'(\epsilon = 5)$ [a.u.]	365	149	6084	3372	2193	1750	2058	1921	1966
ρ	3.45	9.34	5.51	6.24	9.11	20.7	30.6	50.8	69.5

characteristic length for the transition zone is given by

$$L'(\epsilon) = \frac{C_6}{C_5} = \frac{256}{135\pi^2}\frac{(7\epsilon+39)}{(\epsilon+7)}\frac{\beta_{\rm hr}^2}{\beta_{\rm nr}}\,. \tag{2.33}$$

Explicit values for the characteristic lengths $L(\epsilon)$, $L'(\epsilon)$ and $L'_{\epsilon\to\infty}$ are given in Tab. 2.3 for hydrogen, helium and several alkali atoms interacting with a perfectly conducting cylinder as well as for an insulating tube with $\epsilon = 5$.

2.4.1 Shape function approach

The Casimir-Polder potential in the transition zone can be described by a generalised from of the ansatz that has already been used for the potential of an atom in front of a plane surface [27] or a sphere [93]. In this description, the potential in the transition zone between both asymptotic regimes of the potential is expressed using a shape function $v(x)$,

$$V(r) = \frac{V_{\rm nr}(r)}{v\left[V_{\rm nr}(r)/V_{\rm hr}(r)\right]}\,. \tag{2.34}$$

The non-retarded potential $V_{\rm nr}(r)$ diverges faster than $V_{\rm hr}(r)$ in the limit $d \to 0$ [see Eqs. (2.18) and (2.26)] while the highly retarded potential $V_{\rm hr}(r)$ vanishes faster than $V_{\rm nr}(r)$ in the limit of large distances, $d \to \infty$ [see Eqs. (2.20) and (2.30)]. When the magnitudes of $V_{\rm nr}$ and $V_{\rm hr}$ are very different, the Casimir-Polder potential $V(r)$ is close to the weaker of the two, which is $V_{\rm nr}$ for $d \to 0$ and $V_{\rm hr}$ for $d \to \infty$. In order to ensure the correct asymptotic behaviour of the Casimir-Polder potential, $v(x)$ fulfills the following asymptotic properties:

$$v(x) = \begin{cases} 1, & x \to 0, \\ x, & x \to \infty. \end{cases} \tag{2.35}$$

This description of the Casimir-Polder potential using a shape-function approach to describe the transition between the non-retarded and highly retarded regime is is principle no restriction but requires the knowledge of the shape function $v(x)$. However, an accurate numerical evaluation of the full Casimir-Polder potential in Eq. (2.2) is difficult in this

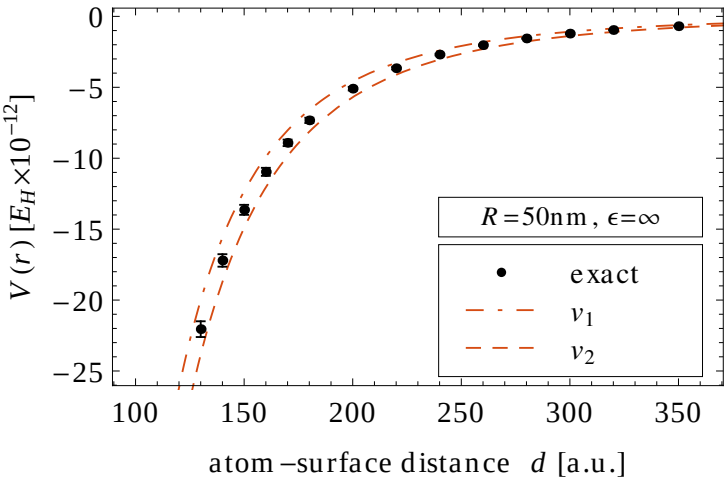

Figure 2.6: Casimir-Polder potential for a hydrogen atom interacting with a cylinder with a radius of 50 nm (≈ 1000 a.u.). The dot-dashed curve shows the potential approximated using the shape function v_1 from Eq. (2.36) and the dashed line shows the approximation using v_2 from Eq. (2.37). The black dots show results of an explicit calculation of the atom-cylinder potential, with errorbars resulting from the uncertainty of the numerical calculation.

transition regime and the exact shape function can only be determined for few particular cases (see Section 2.4.2). For explicit applications of the atom-wire potential for realistic systems in general, we use two shape functions $v(x)$,

$$v_1(x) = 1 + x\,, \tag{2.36}$$

$$v_2(x) = \frac{\pi/2}{\arctan(\pi/(2x))}\,. \tag{2.37}$$

The shape function v_1 was first introduced by Shimizu [25] to analyse experimentally obtained quantum reflection probabilities of metastable neon atoms reflected from a silicon surface. The shape function v_2 was introduced by O'Carroll [94] to describe the interaction potential between two atoms or molecules including retardation effects. Both shape functions have already successfully been applied to similar situations [27, 41, 93].

2.4.2 Casimir-Polder potential between a hydrogen atom and a cylindrical geometry

A calculation of the dynamic polarisability $\alpha(\mathrm{i}\xi)$ via Eq. (2.4) is possible – at least numerically – for a hydrogen atom where all atomic transitions are well-known. This is the only situation where all atomic transitions are known exactly and an evaluation of the full Casimir-Polder potential (2.2) is possible beyond the non-retarded or highly retarded limit, in particular in the transition regime.

In order to analyse the quality of the approximation of the transition region given in Eq. (2.34) using the approximate shape functions (2.36) and (2.37), we calculate the

Table 2.4: Numerical results for the Casimir-Polder potential $V(r)$ for a hydrogen atom in its ground state in front of a perfectly conducting cylinder with a radius of $R = 50\,\mathrm{nm}$ ($\approx 1000\,\mathrm{a.u.}$). The uncertainty results from the extrapolation method in Eq. (2.39).

d [a.u.]	$V(r)/10^{-12}$ [E_H]		d [a.u.]	$V(r)/10^{-12}$ [E_H]	
20	− 8069	± 79	350	−0.6932	± 0.0106
30	− 2338	± 7	400	−0.4234	± 0.0053
40	− 962.2	± 2.5	450	−0.2725	± 0.0027
50	− 480.0	± 3.7	500	−0.1828	± 0.0014
60	− 270.5	± 3.2	550	−0.1270	± 0.0008
70	− 165.8	± 2.5	600	−0.09070	± 0.00046
80	− 108.1	± 2.0	650	−0.06639	± 0.00027
90	− 73.89	± 1.51	700	−0.04962	± 0.00016
100	− 52.43	± 1.16	750	−0.03776	± 0.00010
110	− 38.36	± 0.90	800	−0.02920	± 0.00006
120	− 28.78	± 0.71	850	−0.02290	± 0.00004
130	− 22.05	± 0.56	900	−0.01819	± 0.00002
140	− 17.21	± 0.44	950	−0.01461	± 0.00002
150	− 13.64	± 0.35	1000	−0.01186	± 0.00001
160	− 10.96	± 0.28	1100	−0.008027	$\pm 4 \times 10^{-6}$
170	− 8.915	± 0.229	1200	−0.005606	$\pm 2 \times 10^{-6}$
180	− 7.330	± 0.187	1300	−0.004021	$\pm 1 \times 10^{-6}$
200	− 5.096	± 0.126	1400	−0.002951	$\pm 5 \times 10^{-7}$
220	− 3.656	± 0.087	1500	−0.002210	$\pm 2 \times 10^{-7}$
240	− 2.693	± 0.060	1600	−0.001684	$\pm 1 \times 10^{-7}$
260	− 2.028	± 0.043	1700	−0.001304	$\pm 7 \times 10^{-8}$
280	− 1.556	± 0.031	1800	−0.001023	$\pm 3 \times 10^{-8}$
300	− 1.214	± 0.022	1900	−0.0008132	$\pm 2 \times 10^{-8}$
320	− 0.9614	± 0.0165	2000	−0.0006536	$\pm 1 \times 10^{-8}$

Casimir-Polder potential for a hydrogen atom in its ground state ($1s$) in front of a perfectly conducting cylinder with a radius of 50 nm ($\approx 1000\,\mathrm{a.u.}$). Contributions to the dynamic polarisability (2.4) from transitions to the bound states $|n\,p\rangle$ are included up to $n = 1000$. For hydrogen atoms the transition energies $E_{ji} = E_{n\,p} - E_{1s}$ and the transition matrix element

$$\left|\langle 1s|\hat{d}_\nu|np\rangle\right|^2 = \frac{2^8 n^7 (n-1)^{2n-5}}{3(n+1)^{2n+5}} \tag{2.38}$$

are known analytically [85]. Transitions to continuum states are taken into account up to an energy of $1000\,E_\mathrm{H}$, with the Hartree energy $E_\mathrm{H} = 2\,\mathcal{R}_\infty = 27.21\,\mathrm{eV}$ and have been calculated numerically using the Coulomb continuum wave functions [52]. The remaining transitions contribute less than 0.001% to the Casimir-Polder potential.

In Eqs. (2.2) and (2.10) the summation over the index n in the exact atom-wire po-

tential has to be truncated for an explicit numerical evaluation to a finite range from $-n_{\max}$ to $+n_{\max}$. An accurate treatment of the residual terms $\Delta V(r)$ is not possible in the transition zone. However, in the non-retarded and highly retarded limit an accurate approximation of $\Delta V_{\rm nr}$ and $\Delta V_{\rm hr}$ is possible (see Appendix A). The full Casimir-Polder potential $V^{n_{\max}}(r)$ obtained by truncating the summation can thus be extrapolated to $n_{\max} = \infty$ via

$$V(r) = V^{n_{\max}}(r) \left(1 + \frac{\Delta V_{\rm nr/hr}(r)}{V^{n_{\max}}_{\rm nr/hr}(r)} \right) . \tag{2.39}$$

The full circles in Fig. 2.6 show numerical results for the full Casimir-Polder potential, with the respective error bars coming from the extrapolation procedure in Eq. (2.39). Explicit values for the potential are given in Tab. 2.4. The potential calculated with the help of the shape functions (2.36) and (2.37) (dot-dashed and dashed curves, respectively) provides a fair approximation to the exact potential which lies in between.

This shows that the description of the transition region via approximate shape functions offers a practicable way of numerically calculating the atom-cylinder potential. This method is also applicable to other atoms where the dynamic polarisability $\alpha(\mathrm{i}\xi)$ is unknown but where $\beta_{\rm nr}$ and $\beta_{\rm hr}$ are accessible via the well-known properties $\langle \hat{\boldsymbol{d}}^2 \rangle$ and $\alpha_{\rm d}$ of the atom (see Tab. 2.1 and 2.2). Further calculations show that this result still holds for cylindrical geometries with different radii and also for the case of a dielectric cylinder.

Summary

In this chapter we have presented the long-range Casimir-Polder interaction of a polarisable atom facing a cylindrical geometry with radius R, which has first been given by Nabutovskii *et al.* [48]. The crucial difference at large atom-surface separations between the interaction of an atom with a dielectric cylinder or with a perfectly conducting tube has already been emphasised by Barash and Kyasov [84]. However, we have shown that the potential derived in Ref. [48] accurately describes both cases as long as the limit of perfect conductivity is treated properly.

Particular attention has been given to the non-retarded (Section 2.2) and to the highly retarded limit (Section 2.3) of the Casimir-Polder potential where retardation can either be neglected or becomes dominant. In these limits the potential substantially simplifies and allows an accurate numerical evaluation, as it is shown in Appendix A. Furthermore, the behaviour of the Casimir-Polder potential at large and small distances has been discussed. At short atom-surface separations $(r - R)$, the curvature of the cylinder becomes unimportant and the potential resembles the well-known interaction of an atom facing a plane surface, which is $\propto -1/(r-R)^3$ in the non-retarded and $\propto -1/(r-R)^4$ in the highly retarded limit.

At large distances of the atom to the cylinder, it has been shown that the interaction potential crucially depends on the dielectric properties of the cylinder. The Casimir-Polder potential for an atom facing a dielectric cylinder asymptotically behaves $\propto -1/r^5$ in the non-retarded and $\propto -1/r^6$ in the highly retarded limit. The interaction of an atom with a perfectly conducting tube differs significantly from this behaviour and is $\propto -1/[r^3 \ln(r/R)]$ in the non-retarded and $\propto -1/[r^4 \ln(r/R)]$ in the highly retarded limit.

However, the leading asymptotic behaviour in the perfectly conducting case is not very accurate as next-to-leading-order terms differ only by additional logarithmic factors.

In a realistic situation, the Casimir-Polder potential undergoes a smooth transition from the non-retarded limit at small distances to the highly retarded limit at large distances. We introduced the characteristic length L for thick wires and L' for thin wires, separating the non-retarded from the highly retarded region of the potential. A proper description of the full potential has been presented within a generalised shape-function approach. This method has been shown to be accurate and has successfully been applied to the Casimir-Polder potential of a ground-state hydrogen atom interacting with a perfectly conducting cylinder (Section 2.4).

Chapter 3

Scattering and Absorption of Ultracold Atoms by Nanotubes

The fundamental properties in the interaction of ultracold atoms with a cylindrical geometry can be studied by analysing the corresponding scattering process. The description of a scattering process for atoms colliding with nanostructures in two dimensions has been introduced in Chapter 1 and can now be applied to the scattering and absorption of ultracold atoms at a nanotube. The corresponding Casimir-Polder interaction potential has been discussed in the previous Chapter 2.

In the case of the scattering of ultracold atoms by a flat surface, which has been studied in detail both theoretically [27] and experimentally [25], the interaction potential can only be modified by the choice of the scattered atom or surface material, which offers only limited possibilities. In contrast, the scattering of atoms at a curved surface like a cylindrical geometry introduces the radius of the cylinder as a further tuning parameter to the system. The scattering of ultracold atoms at a perfectly conducting cylinder has already been studied in the non-retarded van der Waals limit in Refs. [42, 47, 95]. We extend this result to the scattering at a cylinder with finite conductivity taking into account the full Casimir-Polder interaction potential. We discuss the dependence of the scattering process of ultracold atoms on the radius of the wire, where we are able to derive analytical results in the limits of a thick and a thin cylinder (Section 3.1). The influence of retardation effects on the scattering process in studied in detail (Section 3.2). Furthermore, we compare the scattering of atoms to the diffraction of light at a cylindrical geometry and show the existence of an electromagnetic and non-electromagnetic limit in the scattering of matter waves (Section 3.3).

The stationary Schrödinger equation describing the scattering process is

$$\left[-\frac{\hbar^2}{2\mu}\frac{\mathrm{d}^2}{\mathrm{d}r^2}+\frac{\hbar^2}{2\mu}\frac{m^2-1/4}{r^2}+V(r)\right]u_m(r)=E\,u_m(r)\,. \tag{3.1}$$

The dynamics of the scattering process is determined by the Energy $E=\hbar^2k^2/(2\mu)$ and the Casimir-Polder interaction potential $V(r)$. The atom-cylinder interaction potential in Eq. (2.34), which is based on a generalised shape function approach (see Section 2.4.1),

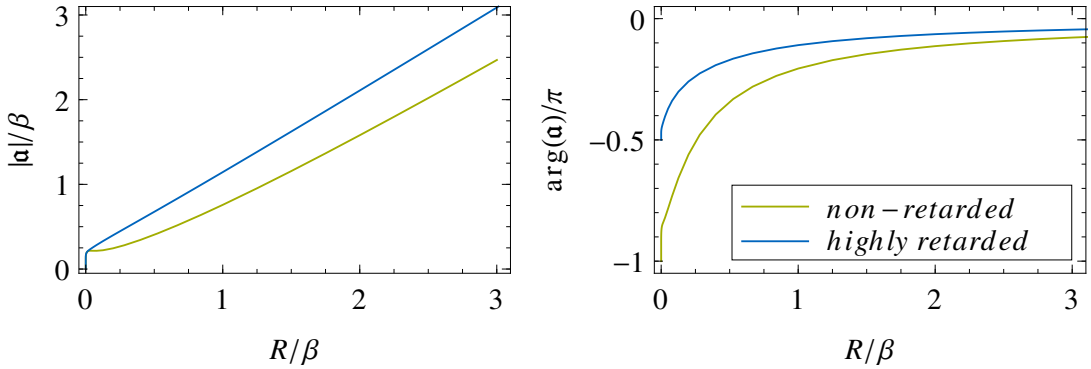

Figure 3.1: Modulus $|\mathfrak{a}|$ and phase $\arg(\mathfrak{a})$ of the scattering length as a function of R/β for a perfectly conducting cylinder, in the non-retarded limit (green line) and in the highly retarded limit (blue line) of the atom-cylinder interaction. The length β is the characteristic length scale β_{nr} or β_{hr} in the corresponding limit.

depends on the radius R of the cylinder as well as on both characteristic lengths β_{nr} and β_{hr}. Expressing the Schrödinger equation in terms of dimensionless quantities ($z = r/\beta_{\mathrm{nr}}$ or $z = r/\beta_{\mathrm{hr}}$) leaves two dimensionless parameters which determine the Casimir-Polder potential; the radius R of the cylinder relative to one of the characteristic length scales β_{nr} or β_{hr} and the characteristic ratio

$$\rho = \frac{\beta_{\mathrm{nr}}}{\beta_{\mathrm{hr}}}\,, \tag{3.2}$$

the latter being a property of the atom only. Explicit values for the characteristic ratio ρ are listed in Tab. 2.3 for hydrogen and several alkali atoms in their respective ground state and helium in its ground or metastable $2S$ state. The energy dependence of the dynamics is given by the dimensionless product of k and one of the characteristic lengths.

The corresponding stationary Schrödinger equation expressed in terms of the dimensionless quantity $z = r/\beta$ is

$$\left[-\frac{\mathrm{d}^2}{\mathrm{d}z^2} + \frac{m^2 - 1/4}{z^2} + U(z, \rho, R/\beta)\right] u_m(z) = (k\beta)^2\, u_m(z)\,, \tag{3.3}$$

where β is one of the two characteristic lengths β_{nr} or β_{hr} and $U = 2\mu/\hbar^2 V$ depending on z, R/β and ρ.

3.1 The scattering length

The scattering of ultracold atoms is dominated by s-wave scattering, and in the regime of low energies the crucial quantity, characterising the scattering process, is the (complex) scattering length $\mathfrak{a}$ (see Section 1.1.3). This scattering length thus gives insight into the fundamental properties of the scattering of ultracold atoms and can be calculated numerically from Eq. (3.3) for $E = 0$ or equivalently $k\beta = 0$, where the asymptotic behaviour of the threshold solutions is given in Eq. (1.28).

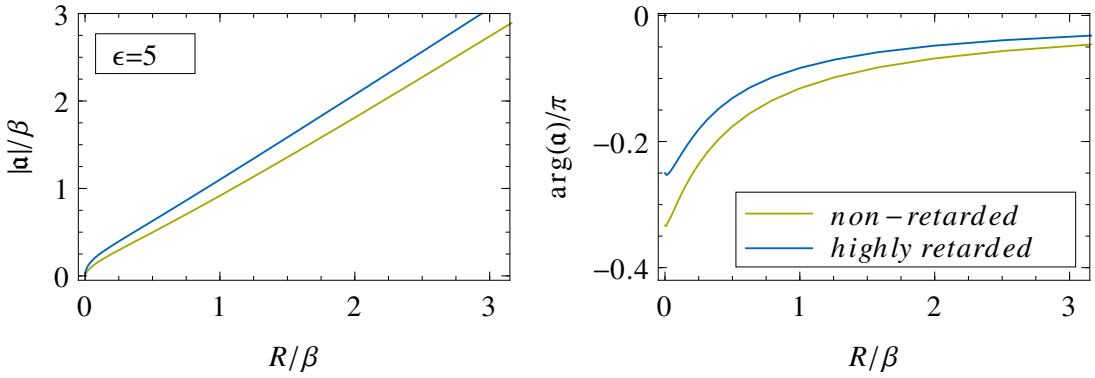

Figure 3.2: Modulus $|\mathfrak{a}|$ and phase $\arg(\mathfrak{a})$ of the scattering length as a function of R/β for a cylinder with dielectric constant $\epsilon = 5$, in the non-retarded limit (green line) and in the highly retarded limit (blue line) of the atom-cylinder interaction. The length β is the characteristic length scale β_{nr} or β_{hr} in the corresponding limit.

The scattering length depends both on the characteristic ratio ρ and on the radius R/β with β being one of the characteristic length scales β_{nr} or β_{hr}. In order to study the influence of the radius on the scattering process and the influence of the Casimir-Polder potential in general, we calculate the scattering length for cases where retardation effects are negligible (see also Refs. [42, 95]) or where retardation becomes dominant. The non-retarded limit [Eqs. (2.14) and (2.15)] of the Casimir-Polder potential, where retardation is neglected, can be obtained from Eq. (2.34) in the limit $\rho \to 0$ while the highly retarded limit [Eqs. (2.22) and (2.23)] of the interaction potential, where retardation is dominant, is obtained in the limit $\rho \to \infty$. In these limits, the scattering length thus depends solely on the dimensionless radius R/β and on the dielectric properties of the cylinder. In a realistic scenario, the Casimir-Polder potential undergoes a smooth transition from the non-retarded to the highly retarded limit and thus, the scattering process may be dominated by the transition regime. However, in many cases, the scattering process is dominated or can be approximated by the non-retarded or highly retarded limit, see Section 3.2.

Figure 3.1 and Fig. 3.2 show the modulus $|\mathfrak{a}|$ (in units of β, left panel) and phase $\arg(\mathfrak{a})$ (right panel) of the scattering length as a function of the ratio R/β, obtained from a numerical solution of the Schrödinger equation (3.3) at $E = 0$. The green line shows results for the scattering length obtained in the non-retarded limit ($\rho \to 0$) and the blue line shows results obtained in the highly retarded limit ($\rho \to \infty$) of the atom-cylinder interaction. The length β is the characteristic length scale β_{nr} (β_{hr}) in the non-retarded (highly retarded) limit. The scattering length shown in Fig. 3.1 is obtained for a perfectly conducting cylinder. The scattering length for a cylinder with a finite dielectric constant $\epsilon = 5$ is shown in Fig. 3.2; qualitatively similar results are obtained for other dielectric constants.

In the limit of large radii, $R \gg \beta$, the scattering length behaves qualitatively similar for a perfectly conducting and for a dielectric cylinder. While the modulus $|\mathfrak{a}|$ increases with increasing values of R/β, the phase $\arg(\mathfrak{a})$ vanishes in the limit of large R/β. This limit is discussed in Section 3.1.2.

Table 3.1: Modulus $|\mathfrak{a}|$, phase $\arg(\mathfrak{a})$, real- $\mathrm{Re}(\mathfrak{a})$ and imaginary $\mathrm{Im}(\mathfrak{a})$ part of the scattering length for the scattering at homogeneous potentials (3.6) in two dimensions [46].

α	3	4	5	6
$\lvert\mathfrak{a}\rvert/\beta_\alpha$	3.1722190	0.8905362	0.7063830	0.6672841
$\arg(\mathfrak{a})/\pi$	-1	$-\frac{1}{2}$	$-\frac{1}{3}$	$-\frac{1}{4}$
$\mathrm{Re}(\mathfrak{a})/\beta_\alpha$	-3.1722190	0	0.353192	0.471841
$\mathrm{Im}(\mathfrak{a})/\beta_\alpha$	0	-0.8905362	-0.611746	-0.471841

For small radii, $R \ll \beta$, the Casimir-Polder potential and therefore the scattering length shows a qualitative different behaviour for the scattering at a perfectly conducting nanotube compared to the scattering at a nanotube with finite dielectric constant. This behaviour of the modulus $|\mathfrak{a}|$ and for the phase $\arg(\mathfrak{a})$ is discussed in the following Section 3.1.1.

3.1.1 The scattering length in the limit of small radii

In the limit of a thin wire, $R \ll \beta$, the scattering length crucially depends on whether the cylinder is insulating (dielectric) or perfectly conducting (metallic), which is a result of the significantly different behaviour of the corresponding Casimir-Polder potentials in the limit of small radii R or large distances d.

Scattering at a perfectly conducting cylinder

For a perfectly conducting cylinder, the asymptotic behaviour of the Casimir-Polder potential for large radii $R \ll d$ is given in Eq. (2.19) for the non-retarded limit of the interaction potential,

$$V_{\mathrm{nr}}^{\epsilon\to\infty}(r) \overset{R/\beta_{\mathrm{nr}}\to 0}{\sim} -\frac{\hbar^2}{2\mu}\frac{\pi}{8}\frac{\beta_{\mathrm{nr}}}{r^3\ln(r/R)} \overset{R/\beta_{\mathrm{nr}}\to 0}{\sim} -\frac{\hbar^2}{2\mu}\frac{\pi}{8}\frac{\beta_{\mathrm{nr}}}{\ln(\beta_{\mathrm{nr}}/R)r^3}\,, \tag{3.4}$$

and for the highly retarded limit in Eq. (2.25),

$$V_{\mathrm{hr}}^{\epsilon\to\infty}(r) \overset{R/\beta_{\mathrm{hr}}\to 0}{\sim} -\frac{\hbar^2}{2\mu}\frac{2}{3\pi}\frac{\beta_{\mathrm{hr}}^2}{r^4\ln(r/R)} \overset{R/\beta_{\mathrm{hr}}\to 0}{\sim} -\frac{\hbar^2}{2\mu}\frac{2}{3\pi}\frac{\beta_{\mathrm{hr}}^2}{\ln(\beta_{\mathrm{hr}}/R)r^4}\,. \tag{3.5}$$

Assuming $\ln(r/R) = \ln(r/\beta) + \ln(\beta/R) \approx \ln(\beta/R)$ for large values of β/R, the behaviour in the thin-wire limit both in the non-retarded and in the highly retarded limit is given by a homogeneous potential of the form

$$V(r) = \frac{C_\alpha}{r^\alpha} = \frac{\hbar^2}{2\mu}\frac{\beta_\alpha^{\alpha-2}}{r^\alpha}\,, \quad \text{with} \quad \beta_\alpha = \left(\frac{2\mu}{\hbar^2}C_\alpha\right)^{1/(\alpha-2)}\,, \tag{3.6}$$

with $\alpha = 3$ in the non-retarded limit and $\alpha = 4$ in the highly retarded limit. The asymptotic form of the Casimir-Polder potential in Eqs. (2.17) and (2.25) falls off faster than the corresponding homogeneous potential only by a reciprocal logarithm.

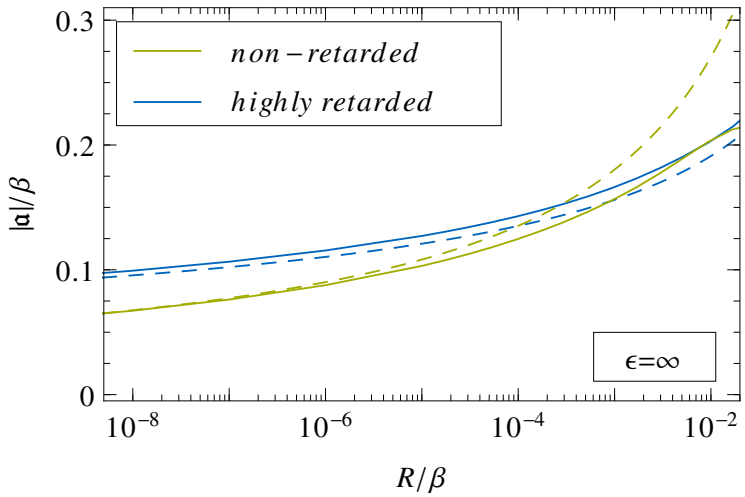

Figure 3.3: Modulus $|\mathfrak{a}|$ of the scattering length on a logarithmic scale for a perfectly conducting cylinder, in the non-retarded limit (green line) and in the highly retarded limit (blue line) of the atom-cylinder interaction. The dashed lines show the behaviour of the scattering length in the limit of small radii $R/\beta \to 0$ from Eqs. (3.7) and (3.8). The length β is the characteristic length scale $\beta_{\rm nr}$ or $\beta_{\rm hr}$ in the corresponding limit.

For a homogeneous potential, the scattering length $\mathfrak{a}$ is proportional to the characteristic length β_α in Eq. (3.6). Values of the scattering length $\mathfrak{a}$ for scattering at a homogeneous potential (3.6) in two dimensions are given in Tab. 3.1 for $\alpha = 3$, 4, 5, and 6. By comparing the asymptotic form of the Casimir-Polder potential for an atom facing a perfectly conducting cylinder in Eqs. (3.4) and (3.5) with Eq. (3.6) we obtain the behaviour of the scattering length $\mathfrak{a}$ in the limit $R/\beta \to 0$,

$$|\mathfrak{a}_{\rm nr}| \overset{R/\beta_{\rm nr}\to 0}{\approx} 3.1722190 \frac{\pi/8}{\ln(\beta_{\rm nr}/R)} \beta_{\rm nr} , \qquad \arg(\mathfrak{a}_{\rm nr}) \overset{R/\beta_{\rm nr}\to 0}{\sim} -\pi \tag{3.7}$$

in the non-retarded limit and

$$|\mathfrak{a}_{\rm hr}| \overset{R/\beta_{\rm hr}\to 0}{\approx} 0.8905362 \sqrt{\frac{2/(3\pi)}{\ln(\beta_{\rm hr}/R)}} \beta_{\rm hr} , \qquad \arg(\mathfrak{a}_{\rm hr}) \overset{R/\beta_{\rm hr}\to 0}{\sim} -\frac{\pi}{2} \tag{3.8}$$

in the highly retarded limit.

The asymptotic value of the phase $\arg(\mathfrak{a})$ of the scattering length from Eqs. (3.7) and (3.8) is accurately reproduced by the numerical calculation of the scattering length in the non-retarded and highly retarded limit, shown in Fig. 3.1. Figure 3.3 shows the modulus $|\mathfrak{a}|$ of the scattering length for small radii $R \ll \beta$ in the non-retarded (green line) and in the highly retarded limit (blue line) of the atom-nanotube interaction. The dashed lines show the behaviour of the scattering length in the limit of small radii, $R \ll \beta$, from Eqs. (3.7) and (3.8). Due to the approximation of the asymptotic form of the Casimir-Polder potential in Eqs. (2.17) and (2.25) by homogeneous potentials, the asymptotic behaviour remains a poor approximation to the exact scattering length for $R/\beta \neq 0$.

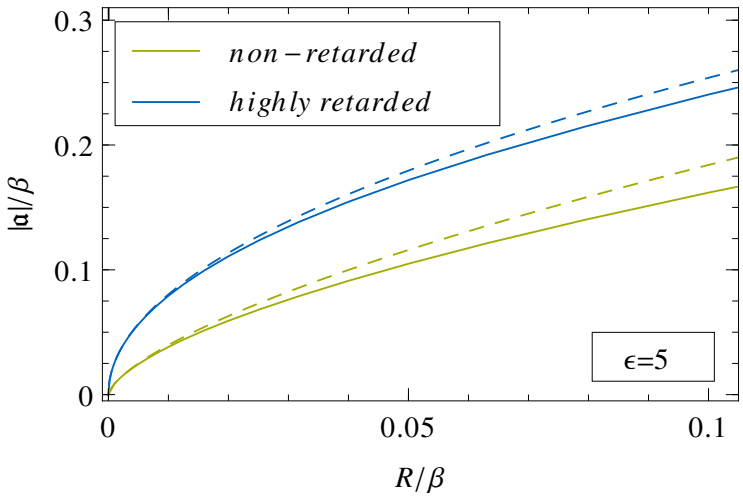

Figure 3.4: Modulus $|\mathfrak{a}|$ of the scattering length for a cylinder with dielectric constant $\epsilon = 5$, in the non-retarded limit (green line) and in the highly retarded limit (blue line) of the atom-cylinder interaction. The dashed lines show the behaviour of the scattering length in the limit of small radii $R \ll \beta$ from Eqs. (3.9) and (3.10). The length β is the characteristic length scale $\beta_{\rm nr}$ or $\beta_{\rm hr}$ in the corresponding limit.

Numerical tests indicate that in the non-retarded limit of the interaction the real part of the scattering length $\mathrm{Re}(\mathfrak{a}_{\rm nr})$ tends to 0 marginally slower than $[\ln(R/\beta_{\rm nr})]^{-1}$ whereas $\mathrm{Im}(\mathfrak{a}_{\rm nr})$ tends to 0 marginally faster than $[\ln(R/\beta_{\rm nr})]^{-1}$ in the limit $R/\beta_{\rm nr} \to 0$ [42, 47, 95]. In the highly retarded limit, both $\mathrm{Re}(\mathfrak{a}_{\rm hr})$ and $\mathrm{Im}(\mathfrak{a}_{\rm nr})$ tend to 0 marginally faster than $[\ln(R/\beta_{\rm hr})]^{-1/2}$.

Scattering at a dielectric cylinder

In contrast to the scattering at a perfectly conducting cylinder, the asymptotic from of the Casimir-Polder potential for an atom interacting with a dielectric cylinder is given by Eqs. (2.18) and (2.26). These asymptotic expressions can be identified with homogeneous potentials with $\alpha = 5$ in the non-retarded and $\alpha = 6$ in the highly retarded limit. By comparing the asymptotic form of the potential in Eqs. (2.18) and (2.26) with Eq. (3.6) we obtain the behaviour of the scattering length $\mathfrak{a}$ in the limit $R/\beta \to 0$,

$$|\mathfrak{a}_{\rm nr}| \overset{R/\beta_{\rm nr}\to 0}{\sim} 0.7063830 \left(\frac{9\pi}{128}\frac{(\epsilon-1)(\epsilon+7)}{\epsilon+1}\beta_{\rm nr}R^2\right)^{1/3}, \quad \arg(\mathfrak{a}_{\rm nr}) \overset{R/\beta_{\rm nr}\to 0}{\sim} -\frac{\pi}{3} \tag{3.9}$$

in the non-retarded limit and

$$|\mathfrak{a}_{\rm hr}| \overset{R/\beta_{\rm hr}\to 0}{\sim} 0.6672841 \left(\frac{2}{15\pi}\frac{(\epsilon-1)(7\epsilon+39)}{\epsilon+1}\beta_{\rm hr}^2R^2\right)^{1/4}, \quad \arg(\mathfrak{a}_{\rm hr}) \overset{R/\beta_{\rm hr}\to 0}{\sim} -\frac{\pi}{4} \tag{3.10}$$

in the highly retarded limit.

The numerical calculation of the scattering length for a dielectric cylinder with $\epsilon = 5$, shown in Fig. 3.2, reproduces the asymptotic value of the phase $\arg(\mathfrak{a})$ from Eqs. (3.9)

and (3.10). Figure 3.4 shows the modulus $|\mathfrak{a}|$ of the scattering length for small radii, $R \ll \beta$, of a cylinder with a dielectric constant of $\epsilon = 5$ in the non-retarded (green line) and in the highly retarded limit (blue line) of the atom-nanotube interaction. The dashed lines show the asymptotic behaviour of the scattering length from Eqs. (3.9) and (3.10). In contrast to the scattering at a perfectly conducting cylinder, the scattering length is accurately described by its thin-wire behaviour from Eqs. (3.9) and (3.10) for $R \ll \beta$.

3.1.2 The scattering length in the limit of large radii

For a thick wire, $R \gg \beta$, the asymptotic behaviour of the Casimir-Polder potential in the non-retarded and highly retarded limit is given by Eqs. (2.17), (2.25), (2.18), and (2.26) for an atom facing a perfectly conducting cylinder or a dielectric tube. The Schrödinger equation at zero energy, $E = 0$, which determines the scattering length, is

$$\left[-\frac{\mathrm{d}^2}{\mathrm{d}\varrho^2} - \frac{1/4}{\varrho^2} - \frac{(\beta_\alpha/R)^{\alpha-2}}{(\varrho-1)^\alpha}\right] u(\varrho) = 0 \tag{3.11}$$

where $\alpha = 3$ in the non-retarded limit and $\alpha = 4$ in the highly retarded limit of the Casimir-Polder potential and $\varrho = r/R$. The characteristic length scales β_α of the potential in the thick-wire limit are

$$\beta_3 = \frac{\epsilon-1}{\epsilon+1}\frac{\beta_{\mathrm{nr}}}{4} \qquad \text{and} \qquad \beta_4 = \sqrt{\frac{3}{4\pi}\frac{\epsilon-1}{\epsilon+1}\,\Phi(\epsilon)}\;\beta_{\mathrm{hr}}\,, \tag{3.12}$$

with the dielectric constant ϵ and $\Phi(\epsilon)$ defined in Eq. (2.27). In the limit of large radii, $R \gg \beta$ and thus $R \gg \beta_\alpha$, the Casimir-Polder potential becomes small and Eq. (3.11) almost corresponds to the free particle case, except for the region close to the surface, $\varrho \to 1$, where the interaction potential is dominant as long as

$$4(\beta_\alpha/R)^{\alpha-2} \ll (\varrho-1)^\alpha \tag{3.13}$$

and the centrifugal term can be neglected. The appropriate wave function obeying incoming boundary conditions for $\varrho \to 1$ is the Hankel function [59],

$$u_{\mathrm{inc}}(\varrho) \propto \sqrt{\frac{\varrho-1}{\beta_\alpha/R}}\; H^{(1)}_{\alpha-2}(y) \quad \text{with} \quad y = \frac{2}{\alpha-2}\left(\frac{\beta_\alpha/R}{\varrho-1}\right)^{(\alpha-2)/2}. \tag{3.14}$$

For sufficiently large values of R/β_α condition (3.13) remains fulfilled even for small values of $(\beta_\alpha/R)/(\varrho-1)$ where the the Hankel function in Eq. (3.14) is accurately represented by its small argument behaviour.

Non-retarded limit

In the non-retarded limit of the Casimir-Polder potential the wave function (3.14) in the limit of small values of $(\beta_\alpha/R)/(\varrho-1)$ is

$$u_{\mathrm{inc}}(\varrho) \overset{R/\beta_3\to\infty}{\propto} -\frac{\mathrm{i}}{\pi}\frac{\varrho-1}{\beta_3/R} + 1 + \frac{\mathrm{i}}{\pi}\left(2\gamma_{\mathrm{E}} + \ln\left(\frac{\beta_3/R}{\varrho-1}\right) - 1\right) + \mathcal{O}\left(\frac{\beta_3/R}{\varrho-1}\right). \tag{3.15}$$

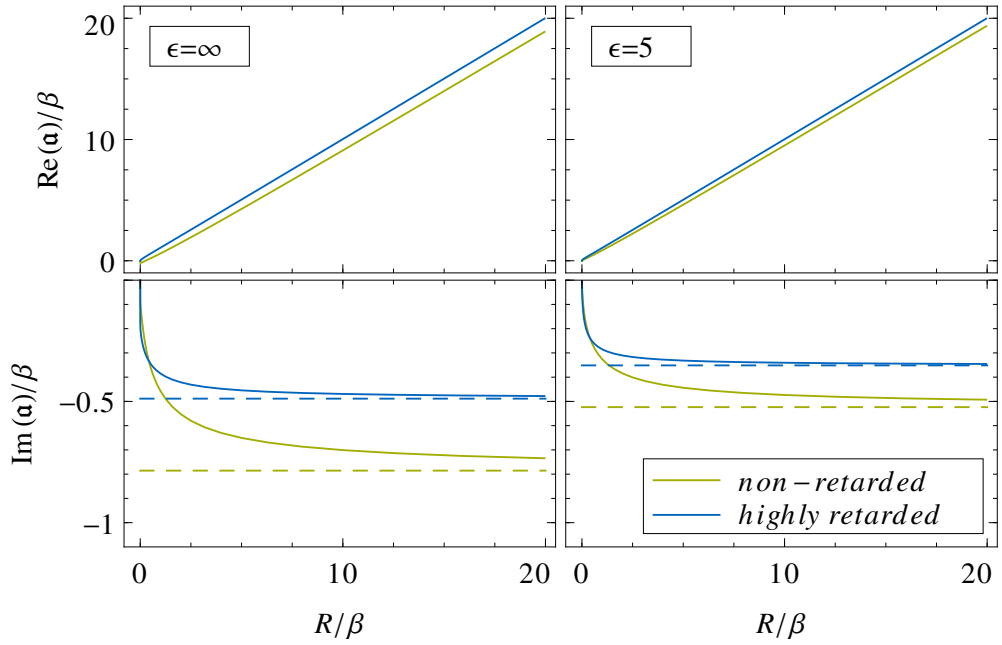

Figure 3.5: Real and imaginary part of the scattering length $\mathfrak{a}$ as a function of R/β for a perfectly conducting cylinder ($\epsilon = \infty$) and for a dielectric tube with $\epsilon = 5$. The green (blue) line shows the scattering length obtained in the non-retarded (highly retarded) limit of the atom-cylinder interaction and the length β is the characteristic length scale β_{nr} or β_{hr} in the corresponding limit. The real part increases linearly, with corrections on $\mathcal{O}(\beta_{\mathrm{nr}})$ in the non-retarded limit, while the imaginary part approaches a constant value (dashed lines) from Eqs. (3.19) and (3.23).

Matching this wave function to the asymptotic free-wave behaviour from Eq. (1.28) for $\varrho \to 1$,

$$u_{\mathrm{as}}(\varrho) \propto -\sqrt{\varrho}\ln\left(\frac{\varrho}{\mathfrak{a}/R}\right) \overset{\varrho\to 1}{\propto} \ln\left(\frac{\mathfrak{a}}{R}\right) - \left[1 - \frac{1}{2}\ln\left(\frac{\mathfrak{a}}{R}\right)\right](\varrho - 1) + \mathcal{O}\left([\varrho-1]^2\right)\,, \quad (3.16)$$

gives $\ln(\mathfrak{a}_{\mathrm{nr}}/R) = 0$ in leading order and

$$|\mathfrak{a}_{\mathrm{nr}}|/R \overset{R/\beta_3\to\infty}{\sim} 1 + \mathcal{O}(\beta_3/R)\,, \qquad \arg(\mathfrak{a}_{\mathrm{nr}}) \overset{R/\beta_3\to\infty}{\sim} -\pi\frac{\beta_3}{R}\,. \quad (3.17)$$

The behaviour of the scattering length $\mathfrak{a}_{\mathrm{nr}}$ in the limit of large radii $R/\beta_{\mathrm{nr}} \to \infty$ thus is [42, 95]

$$\mathfrak{a}_{\mathrm{nr}} \overset{R/\beta_{\mathrm{nr}}\to\infty}{\sim} [R + \mathcal{O}(\beta_{\mathrm{nr}})] \exp\left[-\mathrm{i}\frac{\pi}{4}\frac{\epsilon-1}{\epsilon+1}\frac{\beta_{\mathrm{nr}}}{R}\right] \quad (3.18)$$

or equivalently

$$\mathrm{Re}\,(\mathfrak{a}_{\mathrm{nr}}) \overset{R/\beta_{\mathrm{nr}}\to\infty}{\sim} R + \mathcal{O}(\beta_{\mathrm{nr}})\,, \qquad \mathrm{Im}\,(\mathfrak{a}_{\mathrm{nr}}) \overset{R/\beta_{\mathrm{nr}}\to\infty}{\sim} -\frac{\pi}{4}\frac{\epsilon-1}{\epsilon+1}\,\beta_{\mathrm{nr}}\,. \quad (3.19)$$

Highly retarded limit

In the highly retarded limit of the Casimir-Polder potential, the wave function (3.14) in the limit of small values of $(\beta_\alpha/R)/(\varrho-1)$ is

$$u_{\mathrm{inc}}(\varrho) \overset{R/\beta_4\to\infty}{\propto} \mathrm{i}\sqrt{\frac{2}{\pi}}\frac{\varrho-1}{\beta_4/R}+\sqrt{\frac{2}{\pi}}+\mathcal{O}\left(\frac{\beta_4/R}{\varrho-1}\right) \tag{3.20}$$

and matching to the asymptotic free-wave behaviour from Eq. (3.16) yields

$$|\mathfrak{a}_{\mathrm{hr}}|/R \overset{R/\beta_4\to\infty}{\sim} 1\,, \qquad \arg(\mathfrak{a}_{\mathrm{hr}}) \overset{R/\beta_4\to\infty}{\sim} -\frac{\beta_4}{R}\,. \tag{3.21}$$

The behaviour of the scattering length $\mathfrak{a}_{\mathrm{hr}}$ in the limit of large radii $R/\beta_{\mathrm{hr}}\to\infty$ thus is

$$\mathfrak{a}_{\mathrm{hr}} \overset{R/\beta_{\mathrm{hr}}\to\infty}{\sim} R\,\exp\left[-\mathrm{i}\sqrt{\frac{3}{4\pi}\frac{\epsilon-1}{\epsilon+1}\Phi(\epsilon)}\frac{\beta_{\mathrm{hr}}}{R}\right] \tag{3.22}$$

or equivalently

$$\mathrm{Re}\,(\mathfrak{a}_{\mathrm{hr}}) \overset{R/\beta_{\mathrm{hr}}\to\infty}{\sim} R\,, \qquad \mathrm{Im}\,(\mathfrak{a}_{\mathrm{hr}}) \overset{R/\beta_{\mathrm{hr}}\to\infty}{\sim} -\sqrt{\frac{3}{4\pi}\frac{\epsilon-1}{\epsilon+1}\Phi(\epsilon)}\;\beta_{\mathrm{hr}}\,. \tag{3.23}$$

Figure 3.5 shows the real- and imaginary part of the scattering length $\mathfrak{a}$ in the non-retarded (green line) and in the highly retarded limit (blue line) for a perfectly conducting cylinder (left panel) and for a dielectric tube with $\epsilon=5$ (right panel). The scattering length $\mathfrak{a}$ is plotted as a function of R/β where β is the characteristic length scale β_{nr} or β_{hr} in the corresponding limit. The imaginary part asymptotically approaches the constant value from Eqs. (3.19) and (3.23) which is shown by the dashed lines. The linear increase of the real part is clearly visible in Fig. 3.5 with deviations on $\mathcal{O}(\beta_{\mathrm{nr}})$ in the non-retarded limit.

Note that the imaginary part of the scattering length in the thick-wire limit, $R/\beta\to\infty$, [Eqs. (3.19) and (3.23)] is the value one would expect for the imaginary part of the scattering length in one-dimensional scattering or for s waves in the three-dimensional case for a homogeneous potential (3.6) with $\alpha=3$ (non-retarded case) and $\alpha=4$ in (highly retarded case) and the corresponding length scales from Eq. (3.12) [70, 96]. In fact, close to the surface where the curvature of the cylinder is negligible, the scattering process is effectively one-dimensional and the potential resembles the potential of an atom facing a plane wall, which is $\propto -1/d^3$ in the non-retarded and $\propto -1/d^4$ highly retarded limit [see Eqs. (2.26) and (2.18)]. Although the low-energy behaviour of the scattering process in one or three-dimensional scattering is very different from the two-dimensional case, the imaginary part of the scattering length derived from the one-dimensional near-surface scattering process agrees with the two-dimensional scattering length in the tick-wire limit, even though the real part of the scattering length does not exist for $1/r^3$ potentials in conventional one- or three-dimensional scattering.

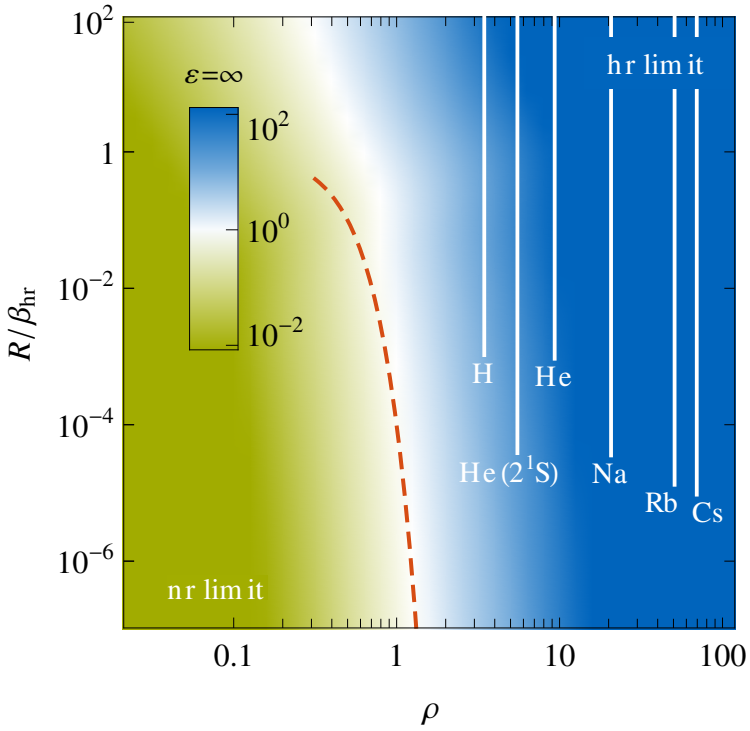

Figure 3.6: Characteristic quantity ξ_R (3.24) on a logarithmic scale as a function of the characteristic ratio ρ and the radius of the wire $R/\beta_{\rm hr}$ for a perfectly conducting cylinder. The green coloured area to the left shows systems where the scattering length has reached its non-retarded (nr) limit ($\xi_R \ll 1$) while the blue coloured area to the right shows systems where the scattering length has reached its highly retarded (hr) limit ($\xi_R \gg 1$). Realistic parameter configurations are shown as white lines. The red dashed line characterises the transition [ξ_R=1] between the non-retarded and highly retarded regime for small radii $R \ll \beta_{\rm hr}$ given in Eq. (3.27).

3.2 Influence of retardation on the scattering process

The behaviour of the atom-cylinder system in the low-energy regime, governed by the scattering length $\mathfrak{a}$, has been discussed in the previous section for the special cases where retardation is negligible (non-retarded limit, $\rho \to 0$) and for the case in which retardation effects are dominant (highly retarded limit, $\rho \to \infty$). In a realistic scenario the characteristic ratio ρ has a finite value, given by the properties of the projectile atom (see Tab. 2.3), and the Casimir-Polder potential undergoes a smooth transition from the non-retarded limit of the potential at short distances to the highly retarded limit of the potential far away from the surface.

The nature of the atom-cylinder scattering process can be characterised by the quantity

$$\xi_R(\rho) = \frac{|\mathfrak{a}(\rho) - \mathfrak{a}_{\rm nr}|}{|\mathfrak{a}(\rho) - \mathfrak{a}_{\rm hr}|}\,, \tag{3.24}$$

where $\mathfrak{a}(\rho)$ is the complex scattering length for a given atom with characteristic ratio ρ and

$\mathfrak{a}_{\mathrm{nr}}$ ($\mathfrak{a}_{\mathrm{hr}}$) is the scattering length obtained from the non-retarded (highly retarded) limit of the atom-cylinder interaction, see Section 3.1. If the scattering process is dominated by the non-retarded part of the interaction then $\xi_R \ll 1$ while if the highly retarded part is dominant then $\xi_R \gg 1$.

3.2.1 Influence of retardation for a perfectly conducting cylinder

For the scattering at a perfectly conducting cylinder ($\epsilon = \infty$) this has already been discussed in Ref. [41]. Figure 3.6 shows $\xi_R(\rho)$ as a function of the characteristic ratio ρ and the scaled radius of the wire R/β_{hr}. The green area shows combinations of R and ρ where the scattering length has reached the non-retarded limit while the blue area shows systems where the scattering length has reached the highly retarded limit. The scattering length $\mathfrak{a}(\rho)$ was calculated using the shape functions (2.36) and (2.37). Similar results were obtained in both cases and were averaged for the calculation of ξ_R. As expected, the scattering length undergoes a smooth transition from the non-retarded limit to the highly retarded limit, indicated by the increase of the function ξ_R from zero to infinity. This transition (white area in Fig. 3.6) takes place around $\rho \approx 1$ and shows only a weak dependence on the radius of the wire. For realistic systems the ratio R/β_{hr} obviously becomes unphysical for R below the Bohr radius. For all atoms listed in Tabs. 2.1 - 2.3, these realistic systems lie in the region where $\xi_R \gg 1$ and therefore are dominated by the highly retarded limit of the potential. This is illustrated in Figure 3.6, where realistic parameter configurations for some of these atoms are shown as white lines.

This result is in agreement with what has already been obtained for the interaction of a neutral atom and a plane surface [27]. The corresponding potential is reached by the atom-wire potential in the limit of large radii and it has already been shown that in this case the scattering process is dominated by the highly retarded part of the potential. Decreasing the radius of the wire has only a weak influence on the transition between the van der Waals and highly retarded limit. For finite and still physically meaningful values of the radius, the system is always dominated by the highly retarded limit. This result is not trivial and is in contrast to what has been obtained for an atom in front of an absorbing sphere [93]. In this case, the system can either lie in the highly retarded regime for large radii or, for small but still physically meaningful radii it can reach the non-retarded van der Waals regime.

Influence of retardation at finite energies

The influence of retardation on the scattering process has been studied via $\xi_R(\rho)$, which is based on the scattering length $\mathfrak{a}$, characterising the low-energy behaviour of the scattering process. To analyse the influence of retardation effects on the scattering process at higher energies where several partial waves contribute, we study in detail the scattering of hydrogen atoms in the ground state ($\rho = 3.45$) and helium atoms in the metastable 2^1S state ($\rho = 5.51$), representing the two systems closest to the transition region between the non-retarded and highly retarded limit in Fig. 3.6. We calculated the total elastic cross section λ_{el} and absorption cross sections λ_{abs} for the scattering at a perfectly conducting

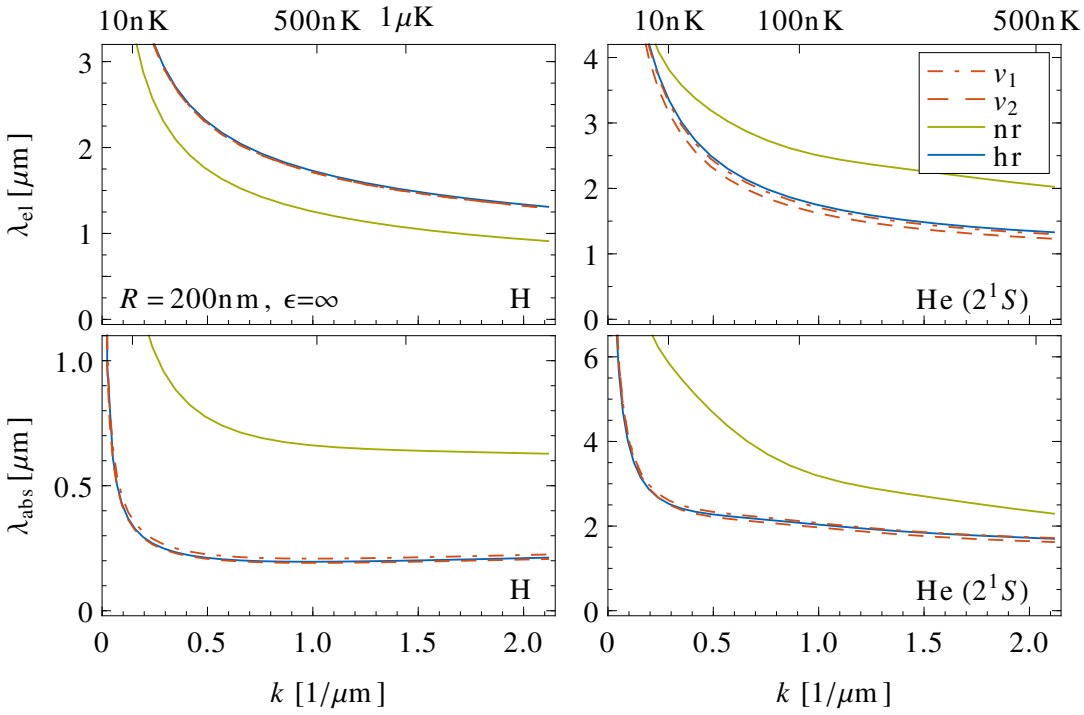

Figure 3.7: Elastic cross section λ_{el} and absorption cross section λ_{abs} as a function of the wave number k for hydrogen atoms in the ground state ($\rho = 3.45$) and helium atoms in the metastable 2^1S state ($\rho = 5.51$) scattered at a perfectly conducting ($\epsilon = \infty$) nanotube with $R = 200\,\mathrm{nm}$. The red dot-dashed [dashed] curve shows the cross section for a potential approximated with the shape function v_1 from Eq. (2.36) [v_2 from Eq. (2.37)] and the solid blue (green) curve shows the cross section in the highly retarded (non-retarded) limit.

nanowire with a radius of $R = 20\,\mathrm{nm}$ and $R = 200\,\mathrm{nm}$ as a function of the wave number k, up to $k = 2/\mu\mathrm{m}$. This corresponds to a temperature of $1.5\,\mu\mathrm{K}$ for hydrogen atoms and 500 nK for metastable helium atoms. Results for the elastic cross section λ_{el} and for the absorption cross section λ_{abs} for a radius of $R = 200\,\mathrm{nm}$ are shown in Fig. 3.7. The red dot-dashed [dashed] curve shows the results for a potential approximated with the shape function v_1 from Eq. (2.36) [v_2 from Eq. (2.37)] and the solid blue (green) line shows the total elastic cross section in the highly retarded (non-retarded) limit.

Figure 3.7 supports the observation from Fig. 3.6; both shape functions give results that differ significantly from the non-retarded limit while only small deviations from the highly retarded limit are observed. This still holds if the radius of the cylinder is decreased down to $R = 20\,\mathrm{nm}$. The elastic cross section λ_{el} and the absorption cross section λ_{abs} for this system are shown in Fig. 3.8. The deviations between the results obtained from both shape functions (red dashed and dot-dashed line) and the non-retarded limit (green line) are still large and the deviations from the highly retarded limit (blue line) have only increased slightly. Changing the projectile atom and going to higher characteristic ratios ρ further decreases the deviations from the highly retarded limit.

The contribution of the s wave to the cross sections is dominant in the low-energy

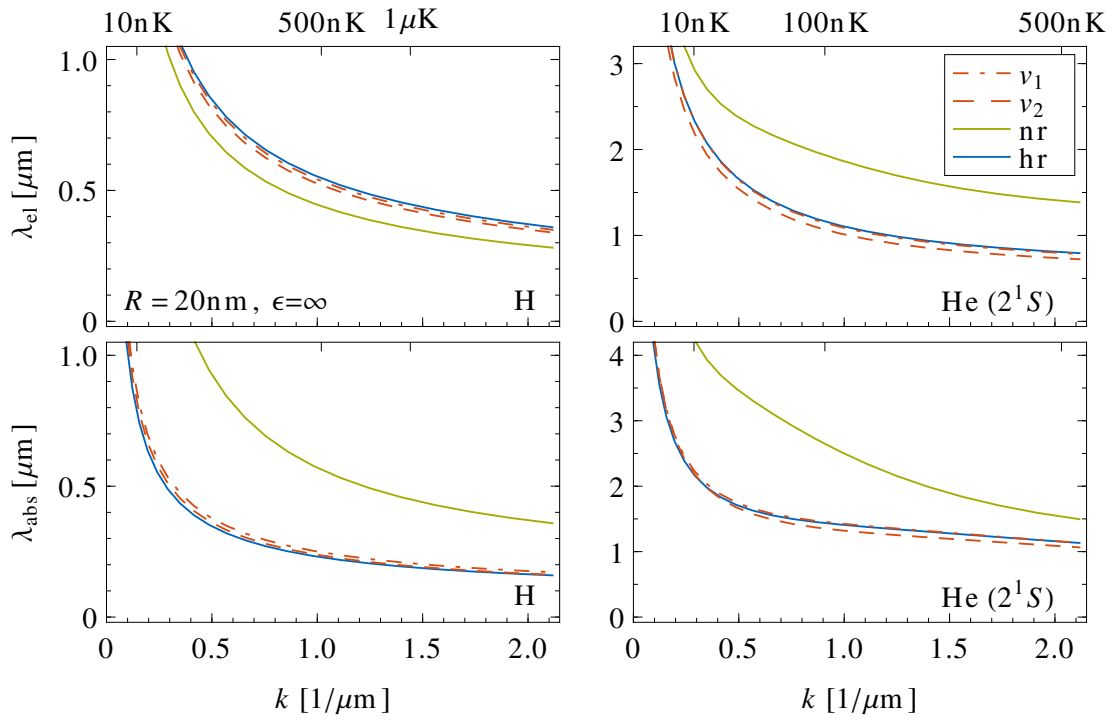

Figure 3.8: Elastic cross section λ_{el} and absorption cross section λ_{abs} as a function of the wave number k for hydrogen atoms in the ground state ($\rho = 3.45$) and helium atoms in the metastable 2^1S state ($\rho = 5.51$) scattered at a perfectly conducting ($\epsilon = \infty$) nanotube with $R = 20\,\mathrm{nm}$. The red dot-dashed [dashed] curve shows the cross section for a potential approximated with the shape function v_1 from Eq. (2.36) [v_2 from Eq. (2.37)] and the solid blue (green) curve shows the cross section in the highly retarded (non-retarded) limit.

regime and gives an isotropic contribution to the differential elastic cross section. The deviation from isotropy, governed by partial waves with $|m| \geq 1$, can be characterised via the dimensionless asymmetry ratio (see also Ref. [93])

$$\Sigma(k) = \frac{\frac{\mathrm{d}\lambda}{\mathrm{d}\phi}(\phi = 0) - \frac{\mathrm{d}\lambda}{\mathrm{d}\phi}(\phi = \pi)}{\frac{\mathrm{d}\lambda}{\mathrm{d}\phi}(\phi = 0) + \frac{\mathrm{d}\lambda}{\mathrm{d}\phi}(\phi = \pi)} \tag{3.25}$$

Figure 3.9 shows the asymmetry ratio (3.25) for hydrogen in the ground state and helium in the metastable 2^1S state scattered at a perfectly conducting nanotube with $R = 20\,\mathrm{nm}$ and $R = 200\,\mathrm{nm}$. The results obtained from the shape functions v_1 (red dot-dashed line) and v_2 (red dashed line) differ from the non-retarded limit (green curve) but show only small deviations from the highly retarded limit.

The results obtained for the elastic cross section and for the absorption cross section as well as for the asymmetry ratio support the observation of Fig. 3.6. The characterisation of the influence of retardation via $\xi_R(\rho)$ at threshold energy, $k = 0$, still holds for higher energies beyond the s-wave regime of the scattering process.

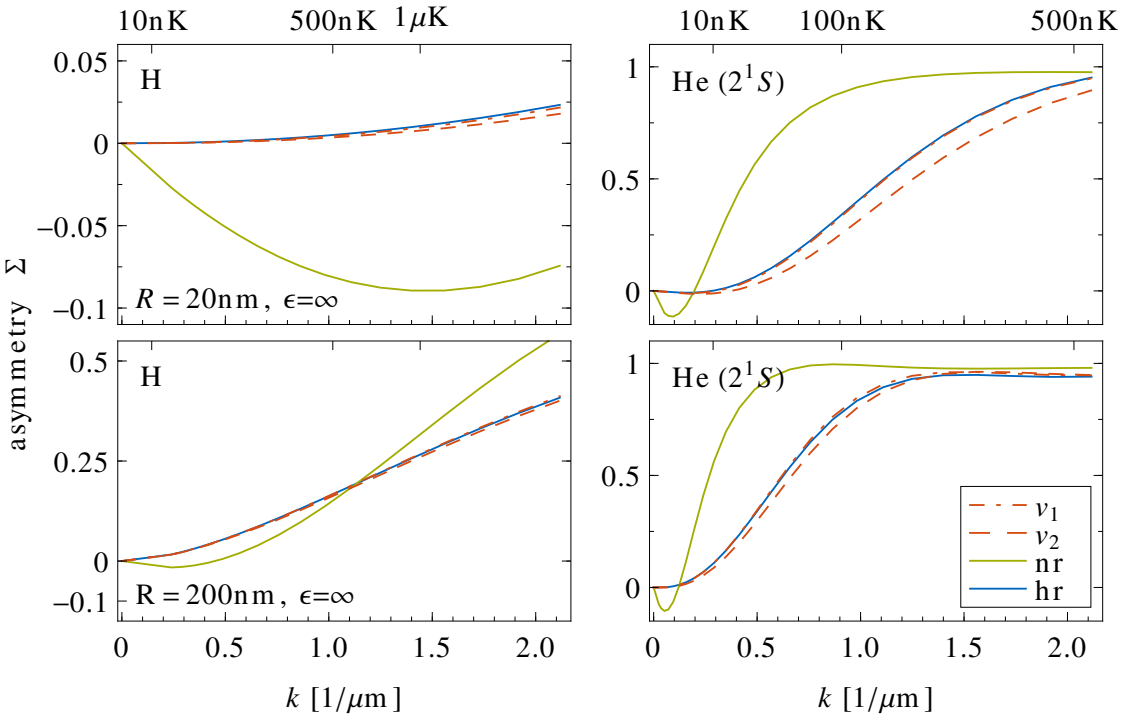

Figure 3.9: Dimensionless asymmetry ratio Σ, defined in Eq. (3.25), as a function of the wave number k for hydrogen atoms in the ground state ($\rho = 3.45$) and helium atoms in the metastable 2^1S state ($\rho = 5.51$) scattered at a nanotube with $R = 20\,\text{nm}$ and with $R = 200\,\text{nm}$. The red dot-dashed (dashed) curve shows results obtained for a potential approximated with the shape function v_1 from Eq. (2.36) [v_2 from Eq. (2.37)] and the solid blue (green) curve shows results obtained from the highly retarded (non-retarded) limit.

Influence of retardation and characteristic length scales of the potential

The key to understanding the influence of retardation on the scattering process lies in the characteristic length of the transition zone L (for $R \gg \beta$) and L' (for $R \ll \beta$) (see Section 2.4) and the characteristic length scales associated with the asymptotic behaviour of the Casimir-Polder potential.

For a thick wire, $R \gg \beta$,[3] the system is equivalent to the scattering of atoms at a plane wall, which has been studied in Ref. [27]. The characteristic length scales $\beta_3^{R\gg\beta}$ and $\beta_4^{R\gg\beta}$, see Eq. (3.12), associated with the asymptotic $1/r^3$ potential (non-retarded limit) and with the $1/r^4$ potential (highly retarded limit) are larger than the corresponding length scale L of the transition zone in the thick-wire limit (see Tab. 2.3) for all atoms listed in Tabs. 2.1 - 2.3. These lengths lie in the highly retarded region of the Casimir-Polder potential. Therefore the scattering process is dominated by the highly retarded limit of the interaction potential and the cross sections are similar to the results obtained in this limit, as it was already shown in Ref. [27].

[3]The length β is the characteristic length scale β_{nr} (β_{hr}) in the non-retarded (highly retarded) limit.

Table 3.2: Characteristic length scales $\beta_3^{R\ll\beta}$ and $\beta_4^{R\ll\beta}$, defined in Eq. (3.26), of the Casimir-Polder potential in the thin-wire limit for hydrogen atoms in the ground state and helium atoms in the metastable 2^1S state facing a perfectly conducting cylinder with radius $R = 200\,\text{nm}$ and $R = 20\,\text{nm}$.

	$\beta_3^{R\ll\beta}(20\text{nm})$	$\beta_4^{R\ll\beta}(20\text{nm})$	$\beta_3^{R\ll\beta}(200\text{nm})$	$\beta_4^{R\ll\beta}(200\text{nm})$	$L'_{\epsilon\to\infty}$
H [a.u.]	634	481	– [a]	– [a]	167
He (2^1S) [a.u.]	10171	6275	16466	9188	2775

[a] For hydrogen atoms and $R = 200\,\text{nm}$ the thin-wire limit ($R \ll \beta$) is not appropriate since $R > \beta$.

In the thin-wire limit, $R \ll \beta$,[3] the Casimir-Polder potential can be approximated by homogeneous potentials (3.4) and (3.5), neglecting logarithmic corrections (see Section 3.1.1). These asymptotic forms of the interaction potential define a characteristic length in the non-retarded ($\beta_3^{R\ll\beta}$) and in the highly retarded limit ($\beta_4^{R\ll\beta}$)

$$\beta_3^{R\ll\beta}(R) = \frac{\pi/8}{\ln(\beta_\text{nr}/R)}\beta_\text{nr}\,, \qquad \beta_4^{R\ll\beta}(R) = \sqrt{\frac{2/(3\pi)}{\ln(\beta_\text{hr}/R)}}\beta_\text{hr}\,. \tag{3.26}$$

Both length scales have a weak dependence on the radius R via $\ln(R/\beta)$ which leads to a weak dependence of the transition between the non-retarded and highly retarded regime on the radius (see Fig. 3.6). For all atoms listed in Tabs. 2.1 - 2.3 and physically meaningful radii in the thin-wire limit, these characteristic lengths are noticeably larger than $L'_{\epsilon\to\infty}$ and lie in the highly retarded regime of the Casimir-Polder potential. The scattering process is thus dominated by the highly retarded limit of the interaction potential and the cross sections resemble the expectations for this limit. Values of $\beta_3^{R\ll\beta}$ and $\beta_4^{R\ll\beta}$ are listen in Tab. 3.2 for hydrogen and helium in its metastable 2^1S state for $R = 20\,\text{nm}$ and $R = 200\,\text{nm}$.

From numerical calculations, it has been observed that the scattering length $\mathfrak{a}(\rho)$ for a realistic atom-cylinder system shows a behaviour similar to the Casimir-Polder potential in Eq. (2.34). When $\mathfrak{a}_\text{nr}$ (non-retarded limit) and $\mathfrak{a}_\text{hr}$ (highly retarded limit) are very different, the scattering length $\mathfrak{a}(\rho)$ is close to the asymptotic result with the smaller modulus and undergoes a smooth transition between these limits if $|\mathfrak{a}_\text{nr}|$ and $|\mathfrak{a}_\text{hr}|$ are similar. The transition regime can thus be estimated by $|\mathfrak{a}_\text{nr}| = |\mathfrak{a}_\text{hr}|$. Applying the analytical results for the scattering length obtained in the thin-wire limit in Eq. (3.7) (non-retarded limit) and in Eq. (3.8) (highly retarded limit), this yields,

$$(R/\beta_\text{hr})_{\xi=1} = \exp\left[-\left(\frac{3.1722190}{0.8905362}\right)^2\frac{3\pi^3}{128}\rho^2\right]. \tag{3.27}$$

This relation is valid for thin, perfectly conducting wires and gives an accurate estimate of the transition region between scattering processes in the low-energy regime that are dominated by the non-retarded or by the highly retarded limit of the Casimir-Polder

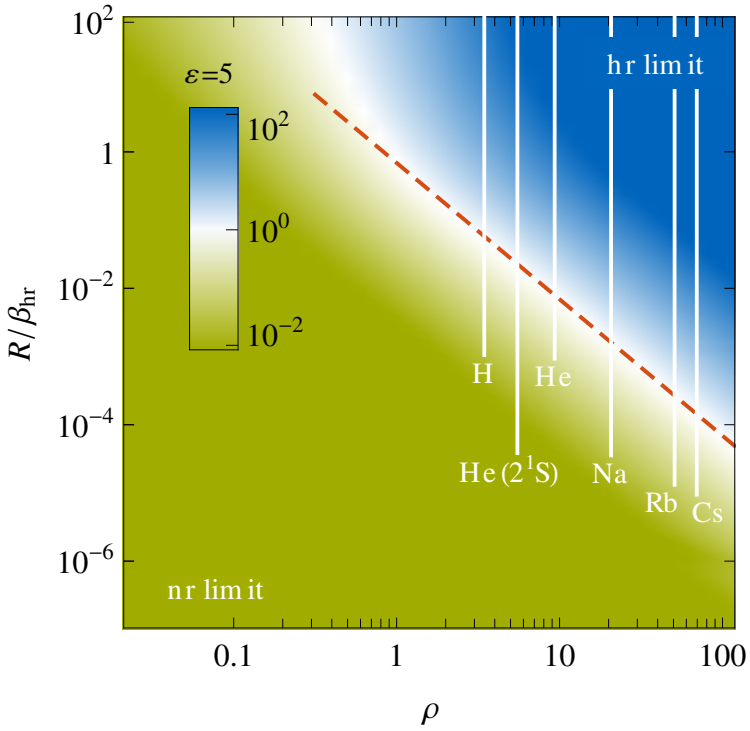

Figure 3.10: Characteristic quantity ξ_R (3.24) on a logarithmic scale as a function of the characteristic ratio ρ and the radius of the wire $R/\beta_{\rm hr}$ for a dielectric cylinder with $\epsilon = 5$. The green coloured area to the left shows systems where the scattering length has reached its non-retarded (nr) limit ($\xi_R \ll 1$) while the blue coloured area to the right shows systems where the scattering length has reached its highly retarded (hr) limit ($\xi_R \gg 1$). Realistic parameter configurations are shown as white lines. The red dashed line characterises the transition [$\xi_R(\rho)$=1] between the non-retarded and highly retarded regime for small radii $R \ll \beta_{\rm hr}$ via Eq. (3.27).

potential. This is illustrated in Fig. 3.6 where Eq. (3.27) is shown as a red dashed line that follows the transition regime (white region in Fig. 3.6) in the limit of small radii. [4]

3.2.2 Influence of retardation for a dielectric cylinder

The scattering of atoms at a dielectric cylinder differs from the perfectly conducting counterpart in particular for small radii $R \ll \beta$.[3] Figure 3.10 shows $\xi_R(\rho)$ as a function of the characteristic ratio ρ and the scaled radius of the wire $R/\beta_{\rm hr}$ for a cylinder with dielectric constant $\epsilon = 5$.

In the limit of large radii, where the Casimir-Polder potential resembles the interaction between an atom and a plane surface, the scattering process is dominated by the highly retarded limit of the potential (blue area in Fig. 3.10) – similar to the scattering at a

[4] If we assume $|\arg(\mathfrak{a}) - \arg(\mathfrak{a}_{\rm nr})| \approx |\arg(\mathfrak{a}) - \arg(\mathfrak{a}_{\rm hr})|$, which seems reasonable in the transition regime, we can directly deduce $\xi_R(\rho) = 1$ from $|\mathfrak{a}_{\rm nr}| = |\mathfrak{a}_{\rm hr}|$, which characterises the transition region in Fig. 3.6 (white area).

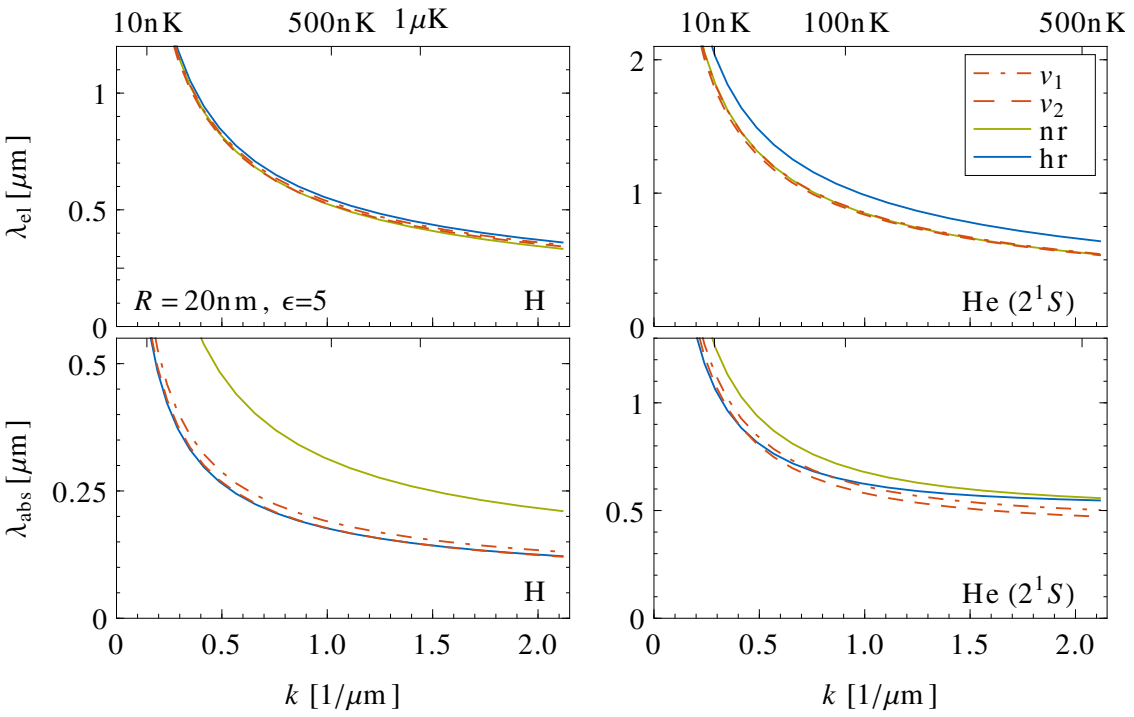

Figure 3.11: Elastic cross section λ_{el} and absorption cross section λ_{abs} as a function of the wave number k for hydrogen atoms in the ground state ($\rho = 3.45$) and helium atoms in the metastable 2^1S state ($\rho = 5.51$) scattered at a dielectric nanotube with $\epsilon = 5$ and $R = 20\,\mathrm{nm}$. The red dot-dashed (dashed) curve shows the cross section for a potential approximated with the shape function v_1 from Eq. (2.36) [v_2 from Eq. (2.37)] and the solid blue (green) curve shows the cross section in the highly retarded (non-retarded) limit.

perfectly conducting cylinder. In contrast, in the limit of small radii, the influence of retardation on the scattering process changes. For small but still physically meaningful radii (see white lines in Fig. 3.10) the scattering of atoms at a dielectric cylinder can be dominated by the transition zone or even by the non-retarded limit (green area in Fig. 3.10). This is in contrast to what has been observed for a perfectly conducting cylinder and resembles the behaviour of the scattering at a spherical geometry [93].

Influence of retardation at finite energies

Similar to the perfect-conductor case (see Section 3.2.1), the scattering of atoms at a thick dielectric tube, $R \gg \beta$, is dominated by the highly retarded limit of the Casimir-Polder potential even for higher energies where several partial waves contribute. In order to study the significantly different behaviour of the scattering process in the thin-wire limit at higher energies, we analyse the scattering of ground state hydrogen atoms and helium atoms in their metastable 2^1S state, scattered at a dielectric cylinder with $\epsilon = 5$ and $R = 20\,\mathrm{nm}$. With $R/\beta_{\mathrm{hr}} = 0.36$ for hydrogen atoms and $R/\beta_{\mathrm{hr}} = 0.013$ for 2^1S helium atoms, these systems are close to the transition region; while the hydrogen system

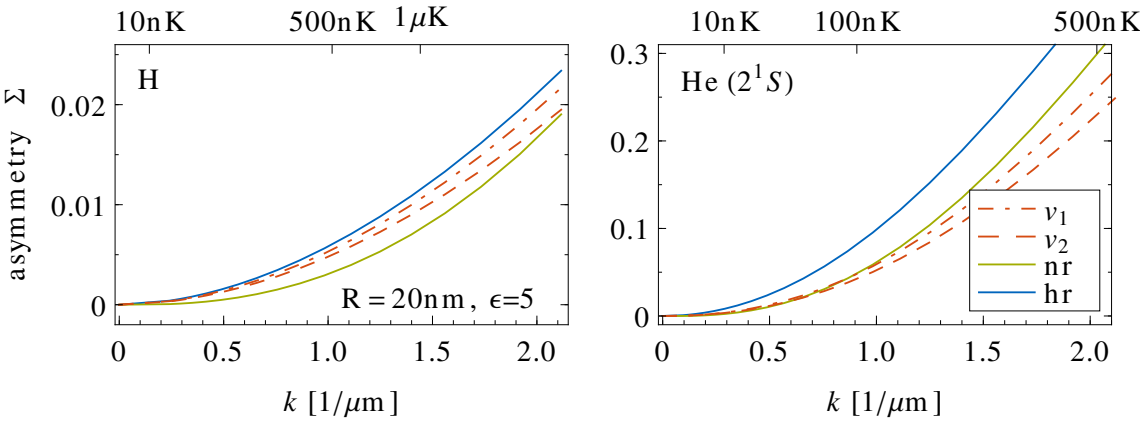

Figure 3.12: Dimensionless asymmetry ratio Σ, defined in Eq. (3.25), as a function of the wave number k for hydrogen atoms in the ground state ($\rho = 3.45$) and helium atoms in the metastable 2^1S state ($\rho = 5.51$) scattered at a dielectric nanotube with $\epsilon = 5$ and $R = 20\,\text{nm}$. The red dot-dashed (dashed) curve shows results obtained for a potential approximated with the shape function v_1 from Eq. (2.36) [v_2 from Eq. (2.37)] and the solid blue (green) curve shows results obtained in the highly retarded (non-retarded) limit.

($\xi \approx 5.2$) is closer to the highly retarded regime, the helium system ($\xi \approx 0.67$) is closer to the non-retarded one. Figure 3.11 shows the elastic cross section λ_{el} and the absorption cross section λ_{abs} as a function of the wave number k in the same regime as in Fig. 3.8, up to $k = 2/\mu\text{m}$. The asymmetry ratio (3.25) for the dielectric case is shown in Fig. 3.12 for hydrogen and helium atoms and a cylinder with $\epsilon = 5$ and $R = 20\,\text{nm}$.

For the absorption of hydrogen atoms, both shape functions (red dashed and dot-dashed line) give results that differ from the non-retarded limit (green line) and show only small deviations from the highly retarded limit (blue line) of the absorption cross section λ_{abs}. For the elastic scattering, the asymmetry ratio obtained from both shape functions is still closer to the highly retarded limit but also shows only small deviations from the non-retarded limit. The total elastic cross sections λ_{el} gives similar results in the non-retarded and in the highly retarded limit and all cross sections are almost indistinguishable.

In contrast, for metastable helium atoms, the results obtained from both shape functions for the elastic cross section λ_{el} differ significantly from the highly retarded limit and are almost indistinguishable from the non-retarded limit. The asymmetry ratio resembles this behaviour; the results obtained from the two shape functions differ from the highly retarded limit and are closer to the non-retarded limit. However, for the absorption cross section λ_{abs} the dominating limit is unclear as results obtained from the two shape functions show similar deviations from both the non-retarded and from the highly retarded limit.

As obtained in Fig. 3.10 for threshold energy, $k = 0$, the scattering of atoms at a thin dielectric cylinder with $R = 20\,\text{nm}$ is dominated by the highly retarded limit in the case of hydrogen atoms and is dominated by the non-retarded limit for helium atoms in their metastable 2^1S state for finite energies beyond the near-threshold regime. However both

Table 3.3: Characteristic length scales $\beta_5^{R\ll\beta}$ and $\beta_6^{R\ll\beta}$, defined in Eq. (3.28), in the thin-wire limit of the Casimir-Polder potential for hydrogen atoms in the ground state and helium atoms in the metastable 2^1S state facing a cylinder with radius $R = 200\,\text{nm}$ and $R = 20\,\text{nm}$ and a dielectric constant of $\epsilon = 5$.

$\epsilon = 5$	$\beta_5^{R\ll\beta}$(20nm)	$\beta_6^{R\ll\beta}$(20nm)	$\beta_5^{R\ll\beta}$(200nm)	$\beta_6^{R\ll\beta}$(200nm)	$L'_{\epsilon=5}$
H [a.u.]	975	682	– [a]	– [a]	365
He (2^1S) [a.u.]	3402	2038	15791	9459	6084

[a] For hydrogen atoms and $R = 200\,\text{nm}$ the thin-wire limit ($R \ll \beta$) is not appropriate since $R > \beta$.

systems are quite close to the transition region and the dominance is less pronounced, e.g. for the elastic cross section for hydrogen or for the absorption cross section for helium atoms. By further decreasing the radius, both systems reach the non-retarded regime and the scattering process is dominated by the non-retarded limit of the interaction potential.

Influence of retardation and characteristic length scales of the potential

The scattering of atoms at a dielectric cylinder in the thick-wire limit resembles the previous case of a perfect conductor and is thus dominated by the highly retarded limit. In contrast, in the thin-wire limit, the influence of retardation on the scattering of atoms at a dielectric cylinder crucially differs from the scattering at a perfectly conducting tube. This can be understood by the significantly different behaviour of the Casimir-Polder potential in the thin-wire limit. The Casimir-Polder potential for a thin wire is given in Eqs. (2.20) and (2.30) which define two characteristic length scales $\beta_5^{R\ll\beta}$ (non-retarded limit) and $\beta_6^{R\ll\beta}$ (highly retarded limit), see Eq. (3.6),

$$\beta_5^{R\ll\beta}(\epsilon, R) = \left(\frac{9\pi}{128}\frac{(\epsilon-1)(\epsilon+7)}{(\epsilon+1)}\beta_{\text{nr}}R^2\right)^{1/3}, \tag{3.28}$$

$$\beta_6^{R\ll\beta}(\epsilon, R) = \left(\frac{2}{15\pi}\frac{(\epsilon-1)(7\epsilon+39)}{(\epsilon+1)}\beta_{\text{hr}}^2R^2\right)^{1/4}, \tag{3.29}$$

depending on the radius R and on the dielectric constant ϵ. For all atoms listed in Tabs. 2.1 - 2.3 and relatively large radii in the thin-wire limit, these length scales are larger than the characteristic length of the transition zone $L'(\epsilon)$, similar to the scattering at a perfect conductor (see Section 3.2.1). However, for sufficiently small radii $\beta_5^{R\ll\beta}$ and $\beta_6^{R\ll\beta}$ can be smaller than $L'(\epsilon)$. Therefore, the characteristic length scales for a thin dielectric cylinder can either lie in the highly retarded or in the non-retarded regime of the Casimir-Polder potential and the scattering process is dominated by the corresponding limit.

Values of $\beta_5^{R\ll\beta}$ and $\beta_6^{R\ll\beta}$ are listen in Tab. 3.3 for hydrogen atoms and a dielectric cylinder ($\epsilon = 5$) of $R = 20\,\text{nm}$ and helium in its metastable 2^1S state and a radius of $R = 20\,\text{nm}$ and $R = 200\,\text{nm}$. For hydrogen atoms and $R = 20\,\text{nm}$ both $\beta_5^{R\ll\beta}$ and $\beta_6^{R\ll\beta}$ are larger than the characteristic length $L'(\epsilon)$ of the transition zone. The scattering process is thus dominated by the highly retarded regime and results are close to the highly retarded limit.

For helium atoms in the metastable 2^1S state, the characteristic length scales $\beta_5^{R\ll\beta}$ and $\beta_6^{R\ll\beta}$ of the asymptotic potential are smaller than $L'(\epsilon)$ for $R = 20\,\mathrm{nm}$ and larger than $L'(\epsilon)$ for $R = 200\,\mathrm{nm}$. The scattering process is thus dominated by the highly retarded limit for $R = 200\,\mathrm{nm}$ but for $R = 20\,\mathrm{nm}$ $\beta_5^{R\ll\beta}$ and $\beta_6^{R\ll\beta}$ lie in the non-retarded regime of the Casimir-Polder potential and the scattering process reaches the non-retarded limit.

The transition regime can again be characterised by $|\mathfrak{a}_{\mathrm{nr}}| = |\mathfrak{a}_{\mathrm{hr}}|$ (see Section 3.2.1). Applying the analytical results for the scattering length in the thin-wire limit from Eqs. (3.9) and (3.10) yields,

$$(R/\beta_{\mathrm{hr}})_{\xi=1} = \left(\frac{0.6672841}{0.7063830}\right)^6 \frac{\left(\frac{9\pi}{128}\frac{(\epsilon-1)(\epsilon+7)}{(\epsilon+1)}\right)^2}{\left(\frac{2}{15\pi}\frac{(\epsilon-1)(7\epsilon+39)}{(\epsilon+1)}\right)^{3/2}} \frac{1}{\rho^2} \tag{3.30}$$

This relation is valid for thin dielectric wires and gives an accurate estimate whether a scattering processes in the low-energy regime is dominated by the non-retarded or by the highly retarded limit of the Casimir-Polder potential. This is illustrated in Fig. 3.10 where Eq. (3.30) is shown as a red dashed line that follows the transition regime (white region in Fig. 3.6) in the limit of small radii.

The influence of retardation on the scattering process clearly reflects the behaviour of the interaction potential. For a thick wire, the atom-cylinder interaction resembles the reflection of an atom from a plane surface, which gives similar results for a dielectric and a perfectly conducting cylinder. For realistic systems in the thick-wire limit, the scattering process is always dominated by the highly retarded limit of the Casimir-Polder potential. In contrast, for a thin wire, the asymptotic behaviour of the atom-cylinder Casimir-Polder potential crucially depends on whether the cylinder is insulating (dielectric) or perfectly conducting (metallic). Thus, the influence of retardation on the scattering at a dielectric cylinder significantly differs from the scattering at a metallic tube. While, in the latter case, retardation still dominates the scattering process in all realistic situations, the scattering at a dielectric cylinder, can be dominated by the transition regime or even by the non-retarded limit for sufficiently small but still physically meaningful radii. An accurate estimate whether a scattering process is dominated by the non-retarded or by the highly retarded limit of the interaction is given in Eqs. (3.27) and (3.30).

3.3 Electromagnetic and non-electromagnetic limit

In the last part of this chapter we compare the scattering of atoms to the diffraction of light at a cylindrical geometry. This is of interest in particular for the diffraction and interference of atoms or large molecules [13, 14] where the wave nature of matter is in the focus of attention. The diffraction of light at a cylinder goes back to Lord Rayleigh [97, 98] and is described by the scattering of electromagnetic waves [97–100]. This scattering process is qualitatively different from the scattering of matter waves. While the latter is governed by the Casimir-Polder interaction, the scattering of electromagnetic waves is determined solely by the boundary conditions at the surface of the cylinder.

3.3.1 Scattering of electromagnetic waves at a cylinder

The propagation of electromagnetic waves in free space is determined by Maxwell's Equations [99, 101]

$$\boldsymbol{\nabla} \times \boldsymbol{B} = \frac{1}{c^2} \frac{\partial \boldsymbol{E}}{\partial t}\,, \qquad \boldsymbol{\nabla} \times \boldsymbol{E} = \frac{\partial \boldsymbol{B}}{\partial t}\,, \tag{3.31}$$

with the electric field $\boldsymbol{E}(\boldsymbol{r},t)$ and magnetic field $\boldsymbol{B}(\boldsymbol{r},t)$ being

$$\boldsymbol{E}(\boldsymbol{r},t) = \boldsymbol{E}_0(\boldsymbol{r})\mathrm{e}^{\mathrm{i}\omega t}\,, \qquad \boldsymbol{B}(\boldsymbol{r},t) = \boldsymbol{B}_0(\boldsymbol{r})\mathrm{e}^{\mathrm{i}\omega t}\,. \tag{3.32}$$

The z derivatives in Eq. (3.31) vanish due to translational invariance along the axis of the cylinder (z-axis). Thus, Eq. (3.31) breaks up into two uncoupled sets, which can be simplified to

$$\left(\partial_x^2 + \partial_y^2 + \frac{\omega^2}{c^2}\right) B_z(\boldsymbol{r}) = 0\,, \qquad (\boldsymbol{e}_z \times \boldsymbol{\nabla}) B_z(\boldsymbol{r}) = \mathrm{i}\frac{\omega}{c^2}\boldsymbol{E}_\perp(\boldsymbol{r})\,, \tag{3.33}$$

$$\left(\partial_x^2 + \partial_y^2 + \frac{\omega^2}{c^2}\right) E_z(\boldsymbol{r}) = 0\,, \qquad (\boldsymbol{e}_z \times \boldsymbol{\nabla}) E_z(\boldsymbol{r}) = \mathrm{i}\omega\boldsymbol{B}_\perp(\boldsymbol{r})\,. \tag{3.34}$$

The subscript $\perp$ denotes the (transversal) components perpendicular to the axis of the cylinder, x and y in Cartesian coordinates or ϕ and r in cylindrical coordinates. Each set of equations consists of a Helmholtz wave-equation for the z component of the magnetic (electric) field and a second equation connecting the z component of the magnetic (electric) field with the perpendicular component of the electric (magnetic) field. The Helmholtz wave-equation is equivalent to the Schrödinger equation (1.1) and the solution for a scattering process can be derived similar to the scattering solution of the Schrödinger equation (see Section 1.1.1 and Refs. [99, 100]). The boundary condition at the surface of the cylinder, $r = R$, is determined by the component of the electric field which is parallel to the surface. Due to the continuity condition at the perfectly conducting surface this component of the electric field vanishes at $r = R$.

Transverse electric mode

Equation (3.33) describes the transverse electric (TE) mode of the electromagnetic field where the electric (magnetic) field is polarised perpendicular (parallel) to the axis of the cylinder. The boundary condition at the surface requires $E_\phi(r = R) = 0$ which leads, via Eq. (3.33), to a von Neumann boundary condition for the magnetic field

$$\left.\frac{\partial B_z}{\partial r}\right|_{r=R} = 0\,. \tag{3.35}$$

Matching the free solution (1.16) of the Helmholtz equation for the z component of the magnetic field (3.33) to this boundary condition gives

$$\tan\delta_m^{(\mathrm{TE})} = \frac{J'_{|m|}(kR)}{Y'_{|m|}(kR)} \tag{3.36}$$

with the wave number $k = \omega/c$.

Transverse magnetic mode

The transverse magnetic (TM) mode of the electromagnetic field where the magnetic (electric) field is polarised perpendicular (parallel) to the axis of the cylinder is described by Eq. (3.34). The boundary condition at the surface leads to a Dirichlet boundary condition for the electric field

$$E_z(r = R) = 0\,. \tag{3.37}$$

Matching the free solution (1.16) for the z component of the electric field from Eq. (3.34) to this boundary condition gives

$$\tan\delta_m^{(\mathrm{TM})} = \frac{J_{|m|}(kR)}{Y_{|m|}(kR)}\,. \tag{3.38}$$

At low incident energies, $kR \to 0$, the s-wave scattering phase shift $\delta_0^{(\mathrm{TE})}$ in the TE mode is of $\mathcal{O}(kR)^2$ while the scattering phase shift $\delta_0^{(\mathrm{TM})}$ in the TM mode is of $\mathcal{O}(1/\ln[kR])$ and the scattering process is dominated by the latter polarisation mode. Comparing the low-energy behaviour of Eq. (3.38) with the near-threshold behaviour of a scattering process in two dimensions, given in Eq. (1.26), we can identify a scattering length in the transverse magnetic mode, $a^{(\mathrm{TM})} = R$, see Ref. [102]. In the transverse electric case, the von Neumann boundary condition violates the preconditions of the scattering process presented in Chapter 1 and shows a qualitatively different behaviour in particular in the low energy regime.[5] A detailed discussion of the scattering of electromagnetic waves at a cylindrical geometry is given in Ref. [100].

3.3.2 Comparing the scattering of atoms with the scattering of electromagnetic waves

In the low-energy regime where the scattering process is governed by the scattering length $\mathfrak{a}$ (see Section 3.1) we can identify two regimes of qualitatively different behaviour in the atom-cylinder scattering process. In the thin-wire limit, $R/\beta \to 0$,[3] the scattering length $\mathfrak{a}$ is mainly determined by the long-range Casimir-Polder interaction, depending both on the properties of the cylinder and on the properties of the atom. In contrast, in the thick-wire limit, $R/\beta \to \infty$,[3] the scattering length $\mathfrak{a}$ is governed primarily by the position of the surface of the cylinder and $\mathfrak{a} \to R$. Thus, in the thick-wire limit, the near-threshold behaviour of the atom-cylinder scattering process approaches the result obtained for the scattering of electromagnetic waves in the transverse magnetic mode scattered at a perfectly conducting cylinder, where $a^{(\mathrm{TM})} = R$.

At finite energy $E = \hbar^2k^2/(2\mu)$, the Schrödinger equation of the scattering process in the limit of a thick cylinder is

$$\left[-\frac{\mathrm{d}^2}{\mathrm{d}\varrho^2} - \frac{m^2 - 1/4}{\varrho^2} - \frac{(\beta_\alpha/R)^{\alpha-2}}{(\varrho-1)^\alpha}\right] u_m(\varrho) = (kR)^2\, u_m(\varrho)\,, \tag{3.39}$$

[5] For a dielectric cylinder an energy-dependent potential term appears in Eq. (3.33) and (3.34). This energy-dependent potential violates the preconditions in Chapter 1 and causes a different behaviour of the scattering process at low energies [100].

where $\alpha = 3$ in the non-retarded limit and $\alpha = 4$ in the highly retarded limit of the Casimir-Polder potential and $\varrho = r/R$. The characteristic length scales β_α are related to β_{nr} and β_{hr} via Eq. (3.12). Similar to Section 3.1.2, the Casimir-Polder potential becomes small in the limit $R/\beta_\alpha \to \infty$ and Eq. (3.39) almost corresponds to the free particle case except for the region close to the surface, $\varrho \to 1$ where the interaction potential is dominant as long as

$$\frac{(\beta_\alpha/R)^{\alpha-2}}{|m^2 - 1/4|} \gg (\varrho - 1)^\alpha \,. \tag{3.40}$$

In this region the centrifugal term $(m^2 - 1/4)/\varrho^2$ in Eq. (3.39) is negligible and the Schrödinger equation corresponds to a one-dimensional scattering process at a homogeneous $-1/(\varrho - 1)^\alpha$ potential. Expressing this one-dimensional Schrödinger equation in dimensionless quantities leads to a dimensionless spatial coordinate $z = (\varrho - 1)/(\beta_\alpha/R)$ and a dimensionless energy term $k\beta_\alpha$. Keeping kR constant, condition (3.40) remains fulfilled while taking the limit $k\beta_\alpha z \to 0$ and simultaneously $z \to \infty$ where we can express the radial wave function $u_m(\varrho)$ by the asymptotic low-energy behaviour of the solution of the one-dimensional Schrödinger equation [52],

$$u_{1\mathrm{D}}(\varrho) \sim k\beta_\alpha \left[1 - \frac{R}{\beta_\alpha}\frac{\varrho - 1}{\mathfrak{a}_{1\mathrm{D}}}\right] \underset{\varrho\to 1}{\overset{R/\beta_\alpha\to\infty}{\sim}} 0 + \mathcal{O}\left(\frac{\beta_\alpha}{R}\right) , \tag{3.41}$$

where $\mathfrak{a}_{1\mathrm{D}}$ is the (complex) scattering length in the one-dimensional scattering process. A detailed discussion of the scattering in one dimension or for s-waves in three dimensions is given in Refs. [52–54]. Matching this wave function to the asymptotic free-wave behaviour from Eq. (1.16) for $\varrho \to 1$,

$$u_m(\varrho) \propto J_{|m|}(kR\varrho) - \tan\delta_m Y_{|m|}(kR\varrho) \,, \tag{3.42}$$

gives

$$\tan\delta_m \overset{R/\beta_\alpha\to\infty}{\sim} \frac{J_{|m|}(kR)}{Y_{|m|}(kR)} + \mathcal{O}\left(\frac{\beta_\alpha}{R}\right) . \tag{3.43}$$

This result is, in leading order, independent of α and is therefore valid not only for the non-retarded and highly retarded limit of the interaction but also for more realistic interaction potentials which exhibit a smooth transition between both limits. In the limit of a thick wire $R/\beta \to \infty$, the scattering phase shift δ_m – and therefore the elastic cross section – depends solely on the dimensionless product kR and is in particular independent – in leading order – of the Casimir-Polder interaction potential, which depends on the properties of the projectile atom and on the dielectric properties of the cylinder. This asymptotic behaviour is illustrated in Fig. 3.13.

Figure 3.13 shows the total elastic cross section λ_{el} (in units of R) for the scattering of atoms at a perfectly conducting cylinder as a function of kR. The solid black line shows the asymptotic cross section reached in the thick-wire limit from Eq. (3.43). The blue (green) lines show results for the scattering of atoms at a perfectly conducting cylinder in the highly retarded (non-retarded) limit. With increasing values of R/β from $R/\beta = 1$ (dashed line), $R/\beta = 5$ (dot-dashed line) to $R/\beta = 50$ (dotted line), the corresponding cross section approaches the asymptotic result in the limit $R/\beta \to \infty$. The length β is the characteristic length scale β_{nr} (β_{hr}) in the non-retarded (highly retarded) limit. Similar

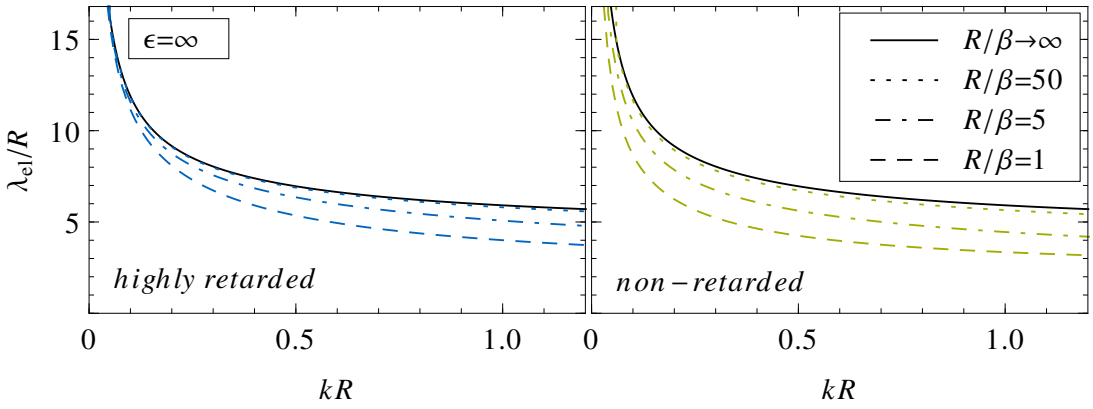

Figure 3.13: Total elastic cross section λ_{el} (in units of R) for the scattering of atoms at a perfectly conducting cylinder as a function of kR for various values of R/β ranging from $R/\beta = 1$ (dashed line), $R/\beta = 5$ (dot-dashed line) to $R/\beta = 50$ (dotted line). The green (blue) line shows the scattering cross section obtained in the non-retarded (highly retarded) limit of the atom-cylinder interaction and the length β is the characteristic length scale β_{nr} or β_{hr} in the corresponding limit. The electromagnetic limit which is obtained at large radii, $R/\beta \to \infty$, is shown as a black solid line.

results are obtained for the scattering of atoms at a dielectric cylinder which shows the same asymptotic behaviour.

Compared to the scattering of electromagnetic waves, the scattering of atoms at a (dielectric or perfectly conducting) cylinder at finite energy is identical to the scattering process of electromagnetic waves in the transverse magnetic mode scattered at a perfectly conducting cylinder of the same radius [see Eq. (3.38) and Eq. (3.36)]. Therefore the thick-wire limit, $R \gg \beta$ can be identified with the *electromagnetic limit* of the atom-cylinder scattering process, which is thus dominated – in leading order – by the energy of the projectile atom and by the radius R of the cylinder only. In contrast, the thin-wire limit $R \ll \beta$ crucially depends on the Casimir-Polder interaction potential and the scattering process deviates from the electromagnetic counterpart. The thin-wire limit $R \ll \beta$ is thus called the *non-electromagnetic limit* of the scattering process, which enables a detailed study of the Casimir-Polder interaction depending on the characteristic ratio ρ as well as on the dielectric properties of the cylinder ϵ and the radius R.

Both limits, the electromagnetic and the non-electromagnetic limit, are within the range of realistic parameter configurations. For a cylinder with a radius R ranging from few nanometres up to several micrometres and different projectile atoms like hydrogen, helium or various alkali atoms (listed in Tab. 2.1 and 2.2) the ratio R/β varies from 10^{-5} (non-electromagnetic limit) up to 100 (electromagnetic limit).

Summary

In this chapter, a dependable approach has been presented to describe the scattering and absorption of ultracold atoms at a nanowire, taking properly into account the two-

dimensional nature of the scattering process as well as the exact Casimir-Polder interaction.

The scattering length – characterising the scattering in the low-energy regime – has been calculated numerically as a function of the radius R and analytical expressions in the limit of a thin and of a thick wire have been derived (Section 3.1). In the limit of large radii, $R \to \infty$, the real part of the scattering length is governed by the position of the surface of the cylinder and thus $\mathrm{Re}(\mathfrak{a}) \sim R$. The imaginary part of the scattering length resembles the results obtained in one-dimensional scattering of an atom at a plane surface and is governed by the corresponding Casimir-Polder potential.

For small radii, $R \to 0$, the behaviour of the scattering length reflects the crucial dependence of the Casimir-Polder potential on the dielectric properties of the cylinder at large distances. For a dielectric cylinder, the modulus $|\mathfrak{a}|$ of the scattering length is $\propto (R^2\beta_{\mathrm{nr}})^{1/3}$ in the non-retarded, and is $\propto (R\beta_{\mathrm{hr}})^{1/2}$ in the highly retarded limit of the interaction. In contrast, for the scattering of atoms at a perfectly conducting cylinder, the modulus of the scattering length is approximately proportional to $[\ln(R/\beta_{\mathrm{nr}})]^{-1}$ in the non-retarded, and to $[\ln(R/\beta_{\mathrm{hr}})]^{-1/2}$ in the highly retarded limit.

In a realistic scenario, the Casimir-Polder potential undergoes a smooth transition between the non-retarded limit at small distances to highly retarded limit at large distances. We have introduced the quantity $\xi_R(\rho)$, which characterises the nature of the low-energy atom-cylinder scattering process (Section 3.2). In the thick-wire limit, the scattering process resembles the reflection of an atom from a plane surface, which is dominated by the highly retarded limit [25, 28]. In the thin-wire limit, the different behaviour of the potential for a dielectric (insulating) and perfectly conducting (metallic) cylinder affects the influence of retardation on the scattering process. While the scattering of atoms at a thin ($R \to 0$) perfectly conducting tube is dominated by the highly-retarded limit for all (realistic) radii, the scattering at a dielectric cylinder can be dominated by the transition zone or even by the non-retarded limit of the potential for sufficiently small, but still physically meaningful, radii. The key to understanding these different behaviours of the scattering process is given by the comparison of the characteristic length scales of the transition zone with characteristic length scales of the asymptotic behaviour of the potential. An accurate estimate whether a scattering process is dominated by the non-retarded or by the highly retarded limit of the interaction is given in Eqs. (3.27) and (3.30).

In the last part of this chapter we have focused on the comparison between the diffraction of light and the scattering of ultracold atoms at a cylindrical geometry (Section 3.3). Both scattering processes are described by the scattering of (electromagnetic or matter) waves. However, the latter case is governed by the Casimir-Polder dispersion force acting between the atom and the solid-state surface. It is found that for large radii, $R \to \infty$, of the cylinder, both scattering processes approach the same result. In contrast, in the limit of small radii, $R \to 0$, the atom-cylinder scattering process depends crucially on the Casimir-Polder potential and differs from the electromagnetic result. These limit are thus called the electromagnetic ($R \to \infty$) and the non-electromagnetic ($R \to 0$) limit of the scattering process.

Table 3.4 summarises the main results for the interaction and scattering of ultracold atoms at a nanotube obtained in Chapter 2 and 3.

	perfectly conducting cylinder		dielectric cylinder	
	thin-wire limit $R \to 0$	thick-wire limit $R \to \infty$	thin-wire limit $R \to 0$	thick-wire limit $R \to \infty$
non-retarded limit	$V_{\mathrm{nr}}(r) \sim -\frac{\hbar^2}{2\mu}\frac{\pi}{8}\frac{\beta_{\mathrm{nr}}}{r^3 \ln(r/R)}$	$V_{\mathrm{nr}}(r) \sim -\frac{\hbar^2}{2\mu}\frac{1}{4}\frac{\beta_{\mathrm{nr}}}{(r-R)^3}$	$V_{\mathrm{nr}}(r) \sim -\frac{\hbar^2}{2\mu}\frac{9\pi}{128}\frac{(\epsilon-1)(\epsilon+7)}{\epsilon+1}\frac{\beta_{\mathrm{nr}}R^2}{r^5}$	$V_{\mathrm{nr}}(r) \sim -\frac{\hbar^2}{2\mu}\frac{\epsilon-1}{\epsilon+1}\frac{1}{4}\frac{\beta_{\mathrm{nr}}}{(r-R)^3}$
	$\lvert\mathfrak{a}_{\mathrm{nr}}\rvert \sim 3.17222\frac{\pi/8}{\ln(\beta_{\mathrm{nr}}/R)}\beta_{\mathrm{nr}}$	$\lvert\mathfrak{a}_{\mathrm{nr}}\rvert \sim R + \mathcal{O}(\beta_{\mathrm{nr}})$	$\lvert\mathfrak{a}_{\mathrm{nr}}\rvert \sim 0.70638\left(\frac{9\pi}{128}\frac{(\epsilon-1)(\epsilon+7)}{\epsilon+1}\beta_{\mathrm{nr}}R^2\right)^{1/3}$	$\lvert\mathfrak{a}_{\mathrm{nr}}\rvert \sim R + \mathcal{O}(\beta_{\mathrm{nr}})$
	$\arg(\mathfrak{a}_{\mathrm{nr}}) \sim -\pi$	$\arg(\mathfrak{a}_{\mathrm{nr}}) \sim -\frac{\pi}{4}\frac{\beta_{\mathrm{nr}}}{R}$	$\arg(\mathfrak{a}_{\mathrm{nr}}) \sim -\frac{\pi}{3}$	$\arg(\mathfrak{a}_{\mathrm{nr}}) \sim -\frac{\pi}{4}\frac{\epsilon-1}{\epsilon+1}\frac{\beta_{\mathrm{nr}}}{R}$
highly retarded limit	$V_{\mathrm{hr}}(r) \sim -\frac{\hbar^2}{2\mu}\frac{2}{3\pi}\frac{\beta_{\mathrm{hr}}^2}{r^4 \ln(r/R)}$	$V_{\mathrm{hr}}(r) \sim -\frac{\hbar^2}{2\mu}\frac{3}{4\pi}\frac{\beta_{\mathrm{hr}}^2}{(r-R)^4}$	$V_{\mathrm{hr}}(r) \sim -\frac{\hbar^2}{2\mu}\frac{2}{15\pi}\frac{(\epsilon-1)(7\epsilon+39)}{\epsilon+1}\frac{\beta_{\mathrm{hr}}^2R^2}{r^6}$	$V_{\mathrm{hr}}(r) \sim -\frac{\hbar^2}{2\mu}\frac{\epsilon-1}{\epsilon+1}\frac{3}{4\pi}\Phi(\epsilon)\frac{\beta_{\mathrm{hr}}^2}{(r-R)^4}$
	$\lvert\mathfrak{a}_{\mathrm{hr}}\rvert \sim 0.89054\sqrt{\frac{2/(3\pi)}{\ln(\beta_{\mathrm{hr}}/R)}}\beta_{\mathrm{hr}}$	$\lvert\mathfrak{a}_{\mathrm{hr}}\rvert \sim R$	$\lvert\mathfrak{a}_{\mathrm{hr}}\rvert \sim 0.66728\left(\frac{2}{15\pi}\frac{(\epsilon-1)(7\epsilon+39)}{\epsilon+1}\beta_{\mathrm{hr}}^2R^2\right)^{1/4}$	$\lvert\mathfrak{a}_{\mathrm{hr}}\rvert \sim R$
	$\arg(\mathfrak{a}_{\mathrm{hr}}) \sim -\frac{\pi}{2}$	$\arg(\mathfrak{a}_{\mathrm{hr}}) \sim -\sqrt{\frac{3}{4\pi}}\frac{\beta_{\mathrm{hr}}}{R}$	$\arg(\mathfrak{a}_{\mathrm{hr}}) \sim -\frac{\pi}{4}$	$\arg(\mathfrak{a}_{\mathrm{hr}}) \sim -\sqrt{\frac{3}{4\pi}\frac{\epsilon-1}{\epsilon+1}\Phi(\epsilon)}\frac{\beta_{\mathrm{hr}}}{R}$
influence of retardation	$L'_{\epsilon\to\infty} = \frac{16}{3\pi^2}\frac{\beta_{\mathrm{hr}}^2}{\beta_{\mathrm{nr}}}$	$L(\infty) = \frac{3}{\pi}\frac{\beta_{\mathrm{hr}}^2}{\beta_{\mathrm{nr}}}$	$L'(\epsilon) = \frac{256}{135\pi^2}\frac{(7\epsilon+39)}{(\epsilon+7)}\frac{\beta_{\mathrm{hr}}^2}{\beta_{\mathrm{nr}}}$	$L(\epsilon) = \frac{3}{\pi}\frac{\beta_{\mathrm{hr}}^2}{\beta_{\mathrm{nr}}}\Phi(\epsilon)$
	$\beta_3^{R\ll\beta} = \frac{\pi/8}{\ln(\beta_{\mathrm{nr}}/R)}\beta_{\mathrm{nr}}$	$\beta_3^{R\gg\beta} = \frac{1}{4}\beta_{\mathrm{nr}}$	$\beta_5^{R\ll\beta} = \left(\frac{9\pi}{128}\frac{(\epsilon-1)(\epsilon+7)}{(\epsilon+1)}\beta_{\mathrm{nr}}R^2\right)^{1/3}$	$\beta_3^{R\gg\beta} = \frac{1}{4}\frac{\epsilon-1}{\epsilon+1}\beta_{\mathrm{nr}}$
	$\beta_4^{R\ll\beta} = \sqrt{\frac{2/(3\pi)}{\ln(\beta_{\mathrm{hr}}/R)}}\,\beta_{\mathrm{hr}}$	$\beta_4^{R\gg\beta} = \sqrt{\frac{3}{4\pi}}\,\beta_{\mathrm{hr}}$	$\beta_6^{R\ll\beta} = \left(\frac{2}{15\pi}\frac{(\epsilon-1)(7\epsilon+39)}{(\epsilon+1)}\beta_{\mathrm{hr}}^2R^2\right)^{1/4}$	$\beta_4^{R\gg\beta} = \sqrt{\frac{3}{4\pi}\frac{\epsilon-1}{\epsilon+1}\Phi(\epsilon)}\,\beta_{\mathrm{hr}}$
	dominant limit for realistic systems		dominant limit for realistic systems	
	highly retarded limit ($L < \beta$)	highly retarded limit ($L < \beta$)	non-retarded limit ($\beta < L$) highly retarded limit ($L < \beta$)	highly retarded limit ($L < \beta$)

Table 3.4: Summary of the results obtained in Chapter 2 and 3 for the scattering of ultracold atoms at a perfectly conducting and at a dielectric cylinder in the thin-wire limit, $R \to 0$, and in the highly retarded limit, $R \to \infty$. The behaviour of the potential $V(r)$ and the corresponding scattering lengths $\mathfrak{a}$ is shown in the non-retarded and highly retarded limit of the Casimir-Polder potential. The characteristic length scales β and L, determining the influence of retardation, are given, as well as the dominant limit for realistic atom-cylinder systems.

Chapter 4

Application to a Complex Hybrid System

In the previous chapter the fundamental scattering process of an atom interacting with a cylindrical geometry has been studied. This system forms the basis for understanding more nanotube-based hybrid systems of higher complexity. Particular attention is currently being given to the fundamental system of a single carbon nanotube (CNT) interacting with a cold gas of atoms, such as a Bose-Einstein condensate (BEC) or a thermal cloud of atoms (see Fig. 4.1) [49–51, 74]. This is by far not a trivial problem and raises the question of the applicability of established scattering theory and non-dynamical approaches [51].

In this chapter, we present an accurate description for the absorption of atoms from ultracold quantum gases by a carbon nanotube (see also Ref. [50]). The approach is based on the underlying scattering process and on the atom-cylinder Casimir-Polder potential that has been discussed in detail in the previous chapter. Within our description, we are able to understand and describe recent experiments, where the trap loss induced by a CNT immersed in a thermal cloud (Section 4.2 and 4.3) and in a Bose-Einstein condensate (Section 4.4) has been measured by Schneeweiss *et al.* [49]. In contrast to fitting an arbitrarily chosen model potential to the experimental data which has been done in Ref. [49], our parameter-free approach gives insight into the underlying physics (Section 4.5) and offers a basis for extensions to more complex hybrid systems, which can be useful for the design of CNT based nanodevices.

The interaction potential between an atom and an actual CNT of finite length L and varying radius $R(z)$ obviously differs in a non-trivial fashion from the Casimir-Polder potential obtained in Chapter 2 for an atom facing an ideal cylinder of infinite length. The interaction potential of such a nanotube remains in general unknown. Approximative methods such as pairwise-summation approaches [103] can, in general, not reproduce the correct Casimir-Polder forces [104] and are only guaranteed to become accurate in the limit of rarefied media [51]. Variations of the interaction energy along the tube axis are, however, small as long as the radius $R(z)$ of the CNT varies smoothly. In this case, the longitudinal free motion of an atom along the CNT may be separated from the two-dimensional dynamics perpendicular to the tube, as in Chapter 3. The dynamics

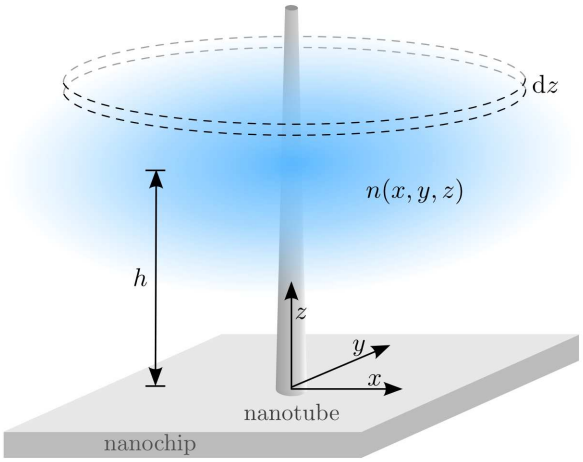

Figure 4.1: Schematic view of a carbon nanotube immersed into a cloud of trapped atoms with a density $n(x, y, z)$. The nanotube is grown on top of a nanochip and the centre of the cloud is held at a distance h to this surface.

perpendicular to the tube is thus governed by the Casimir-Polder potential of the atom interacting with a cylinder of radius $R(z)$ which has been discussed in Chapter 2. The contribution of a single perpendicular plane to the total loss rate γ can be given in a differential form

$$\mathrm{d}\gamma(z) = n(0,0,z)K_{\mathrm{in}}^{\mathrm{2D}}\mathrm{d}z\,, \tag{4.1}$$

with the density of particles $n(x, y, z)$ around the nanotube, located at $(x, y) = (0, 0)$ and the loss rate constant $K_{\mathrm{in}}^{\mathrm{2D}}$ for inelastic and reactive scattering in this two-dimensional (2D) subsystem. The loss rate constant depends on the absorption cross section λ_{abs} of the underlying scattering process which has been discussed in Chapter 1. The total trap loss γ of the full system is obtained by integration over all two-dimensional planes along the nanotube,

$$\gamma = \int_0^L n(0,0,z)K_{\mathrm{in}}^{\mathrm{2D}}\mathrm{d}z\,. \tag{4.2}$$

Deviations from this description might be expected at the tip of the nanotube where on the one hand, the dynamics along the tube axis is influenced by the atom-nanotube potential and on the other hand, the potential differs from the potential of an atom facing an ideal, infinite cylinder. However, these deviations will only give small corrections to the total trap loss (see Section 4.2).

The Casimir-Polder potential for the interaction of an atom with a multiwall carbon nanotube depends on the non-trivial dielectric properties $\epsilon(\mathrm{i}\omega)$ of the CNT [24, 105, 106]. For the actual nanotube used in the experimental setup of Schneeweiss *et al.* [49] these are not known. In our ansatz we assume a frequency independent dielectric constant ϵ ranging from $\epsilon = 2.5$ (insulator) to $\epsilon = 100$ (almost metallic), which includes the range of realistic values. Thermal contributions to the Casimir-Polder interaction become important at distances larger than the thermal wave length $\lambda_{\mathrm{T}} = \hbar c/(k_{\mathrm{B}}T)$ [107]. For a thin tube with a dielectric constant in the given regime ($2.5 \leq \epsilon \leq 100$) and with a radius in the nanometre

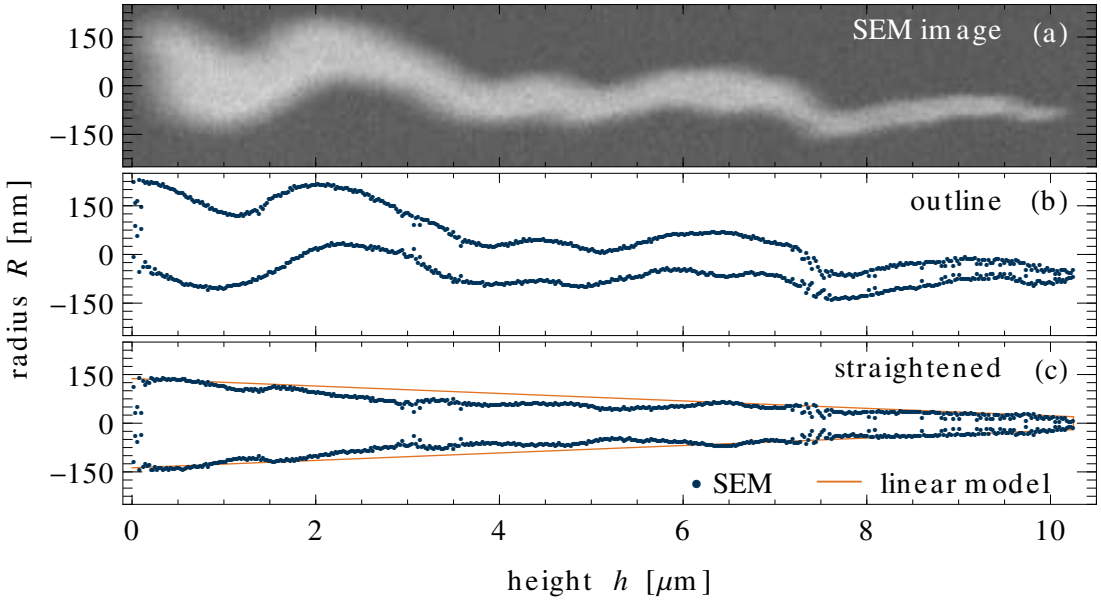

Figure 4.2: Shape of the carbon nanotube used in the experimental setup of Ref. [49]. The exact shape (blue dots) of the nanotube has been determined from an SEM (scanning electron microscope) image (a) in Ref. [108]. Panel (b) shows the profile of the nanotube in the x-z plane and exhibits a slightly distorted shape of the CNT, see Ref. [108]. In panel (c) the shape of the tube has been straightened and the orange curve shows a linear model of the shape of the nanotube. Notice that the length scale of the ordinate has been stretched.

regime the characteristic length scales in this thin-wire limit $\beta_5^{R\ll\beta}(R)$ and $\beta_6^{R\ll\beta}(R)$, given in Eq. (3.28), are smaller than the thermal wave length at room temperature, which is $\lambda_T \approx 7.6\,\mu$m. Thermal contributions are thus negligible.

Within this description, we are able to calculate the trap loss of a cloud of atoms interacting with a CNT.

4.1 Experimental setup

In a recent experiment [49] Schneeweiss *et al.* measured the losses of ^{87}Rb atoms absorbed by a multiwall carbon nanotube, which was grown on top of a nanochip. The CNT was immersed into a BEC and into a cloud of thermal atoms and the trap loss γ was measured as a function of the distance h between the centre of the trap and the surface of the nanochip (see Fig. 4.1). The nanotube used in the experimental setup has a length of $L = 10.25\,\mu$m and a diameter ranging from 275 nm at the bottom to 40 nm at the tip. Figure 4.2 shows the actual shape of the carbon nanotube determined from a scanning electron microscope (SEM) image [panel (a) in Fig. 4.2] from Ref. [108]. Panel (b) in Fig. 4.2 shows the profile of the nanotube in the x-z plane which exhibits a slightly

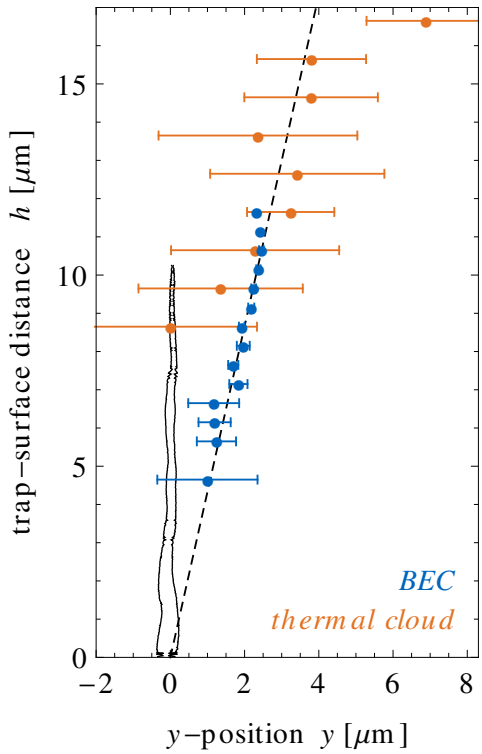

Figure 4.3: Shift of the centre of the atom-cloud in y-direction varying with the trap-surface distance h. The blue (orange) circles show results obtained from a fit of the experimental data from Ref. [49] to the trap loss calculated from Eq. 4.2 for a Bose-Einstein condensate (thermal cloud). The results from the fit are in agreement with a simulation of the magnetic fields of the trap, which predicts an angle of 13° between the tube axis and the ray on which the centre of the cloud lies (dashed line) [109]. The trap-surface distance where the cloud is centred over the nanotube is $h \approx 0$ which is determined by fitting the positions.

distorted shape of the CNT, see Ref. [108]. This distortion has been smoothed and the straightened outline of the tube is shown in panel (c) together with a linear model of the CNT (orange curve) which is used in the theoretical description,

$$R(z) = 135.5\,\mathrm{nm} - z \times 0.011463\,. \tag{4.3}$$

The carbon nanotube together with its carrier nanochip is placed on top of an atom chip. The rubidium atoms are kept in a magnetic Ioff-Pichard trap, which can be moved in all spatial directions and allows a precise positioning of the atom cloud. A detailed discussion in presented in Refs. [108, 110]. The magnetic trapping potential is accurately approximated by a harmonic potential [108, 110, 111],

$$V_{\mathrm{trap}}(x,y,z) = \frac{\mu}{2}\left[\omega_x^2(x-x_0)^2 + \omega_y^2(y-y_0)^2 + \omega_z^2(z-z_0)^2\right]\,. \tag{4.4}$$

around the potential minimum at (x_0, y_0, z_0). The frequencies of the harmonic trapping

potential are [109]

$$\omega_x = 2\pi\ 16\,Hz\,, \qquad \omega_y = \omega_z = 2\pi\,[87.72\,\mathrm{Hz} - h \times 0.77\,\mathrm{Hz}/\mu\mathrm{m}]\,; \tag{4.5}$$

note that ω_y and ω_z slightly change with the distance h of the trap centre to the surface of the nanochip. Furthermore, the centre of the cloud is shifted away from the tube in y-direction with increasing distance h. The centre of the cloud lies on a ray forming an angle of 13° with the z-axis, which has been obtained from a simulation of the magnetic trap-fields [109] but was not included in the discussion of Ref. [49]. This shift (shown as a dashed line in Fig. 4.3) is in agreement with a fit of the y-position of the cloud via Eq. (4.2) to the experimental data from Ref. [49]; see Sections 4.3 and 4.4 for a detailed description of the calculation. This fit of the y-position is shown in Fig. 4.3 where the blue (orange) circles show results obtained for the trap loss from a Bose-Einstein condensate (thermal cloud); in this calculation a dielectric constant of $\epsilon = 5$ is assumed for the nanotube. The error bars, which result from the uncertainty of the experimental data, show that this shift has to be accounted for in order to describe the experimental measurement accurately within the given uncertainty. The trap-surface distance h where the cloud is centred over the nanotube remains unknown in the experimental setup and in the simulation of the magnetic trap-fields [109]. However, the fit shown in Fig. 4.3 indicates that the trap is centred over the tube at $h \approx 0$.

The experimental data from Ref. [49] are, for both cases (BEC and thermal cloud), assigned to trap-surface distances measured separately with a BEC. Notice that the authors of Ref. [49] relate their data for the thermal cloud to a different calibration [108], imposing an artificial shift of $2.05\,\mu$m on the trap-surface distance. This calibration is based on a simplified classical model and neglects quantum mechanical effects like tunnelling or quantum reflection which play a non-negligible role. This observation is supported by Ref. [112] which accurately describes the calibration system and which remarks the necessity to account for quantum mechanical effects.

4.2 A classical time-dependent simulation

In a first approach, we study the hybrid system of a nanotube immersed in a cloud of thermal atoms within a classical time-dependent three-dimensional simulation, similar to a molecular dynamics simulation. In this simulation we can precisely control the hybrid system and verify our ansatz and the assumptions made in Eq. (4.2). A cloud of $N_0 = 1000$ particles at constant temperature is placed in a harmonic trapping-potential. The interaction potential between the atoms and the tube is approximated by the highly retarded limit of the Casimir-Polder potential for a thin cylinder from Eq. (2.30). The approximation of the thin-wire limit is appropriate as $R/\beta < 0.04$ (both for $\beta = \beta_{\mathrm{nr}}$ and $\beta = \beta_{\mathrm{hr}}$) for the given nanotube of Fig. 4.2. Furthermore, it is reasonable to apply the highly retarded limit as the characteristic length scales $\beta_5^{R\ll\beta}(R)$ and $\beta_5^{R\ll\beta}(R)$ from Eq. (3.28) are significantly larger than the corresponding length scale of the transition zone $L'(\epsilon)$ for the given nanotube and a dielectric constant in the range of $\epsilon = 2.5$ up to $\epsilon = 100$, see Section 3.2.2. In contrast to the sharp cutoff indicated by Eq. (4.2), the effect of the finite length of the tube has been taken into account by a smooth decrease of the potential at the endings of the tube,

$$V(r,z) = V_{L=\infty}[r; R(z)]\ F(r,z)\,. \tag{4.6}$$

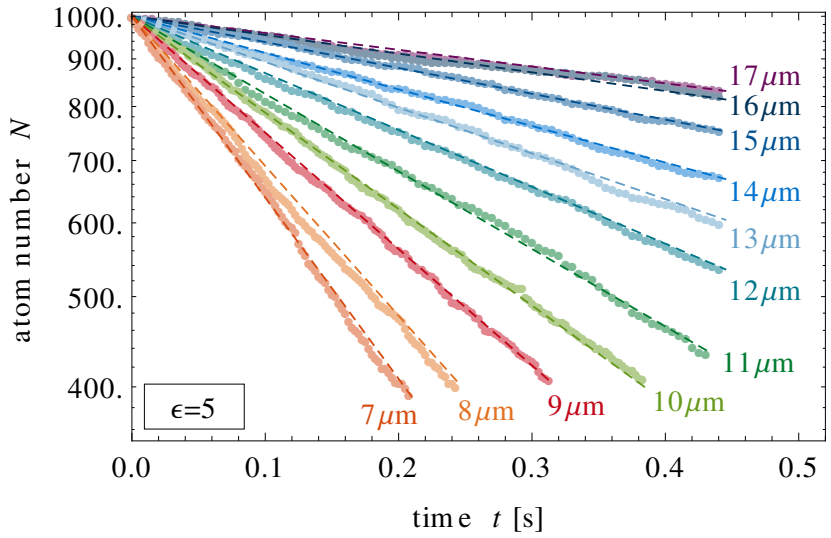

Figure 4.4: Atom number N as a function of time t for a thermal cloud of rubidium atoms absorbed by a nanotube for different trap-surface separations h ranging from $7\,\mu$m up to $17\,\mu$m. The radius $R(z)$ from Eq. (4.3) and the length L of the tube are chosen in accordance with the experimental setup from Ref. [49] and the dielectric constant is assumed to be $\epsilon = 5$. An exponential decay (4.9) is fitted to the atom losses and shown as dashed lines.

The potential $V_{L=\infty}[r; R(z)]$ of a cylinder with infinite length (in the highly retarded thin-wire limit) is given in Eq. (2.30); the smooth decay around the tip is described by the z-dependent function,

$$F(r,z) = \frac{\int_0^L \left[r^2 + (z-z_0)^2\right]^{-7/2} \mathrm{d}z_0}{\int_{-\infty}^{+\infty} \left[r^2 + (z-z_0)^2\right]^{-7/2} \mathrm{d}z_0}\,, \tag{4.7}$$

which is based on a simple pairwise summation approximation [103]. In this approximation, the interaction of the atom with a solid-state object is calculated by dividing the nanotube into infinite elements and summing up the interaction energies of the atom with each of these infinite elements. The interaction of an atom with an infinite element, in the highly retarded limit, is $\propto -1/s^7$, where s is the distance of the atom to the element. The function $F(r,z)$ is given by the ratio of a pairwise summation potential for an infinitesimal-thin ($R \to 0$) cylinder of length L and for a cylinder of infinite length. This model potential becomes exact in the limit $L \to \infty$, however, numerical tests show that the decay of the potential at the tip of the nanotube has no significant effect on the obtained trap loss and the assumption of a sharp cutoff gives accurate results.

The temperature T of the cloud is kept constant in the simulation using an Andersen-type thermostat [113], where the momenta of the atoms are repeatedly reset according to the Boltzmann distribution at temperature T after a time t that is randomly chosen with a Poisson distribution. This method is a common and well-established procedure in molecular dynamic simulations. In the experimental situation, the temperature of the atom cloud stays constant over time due to cooling by surface evaporation [114] at

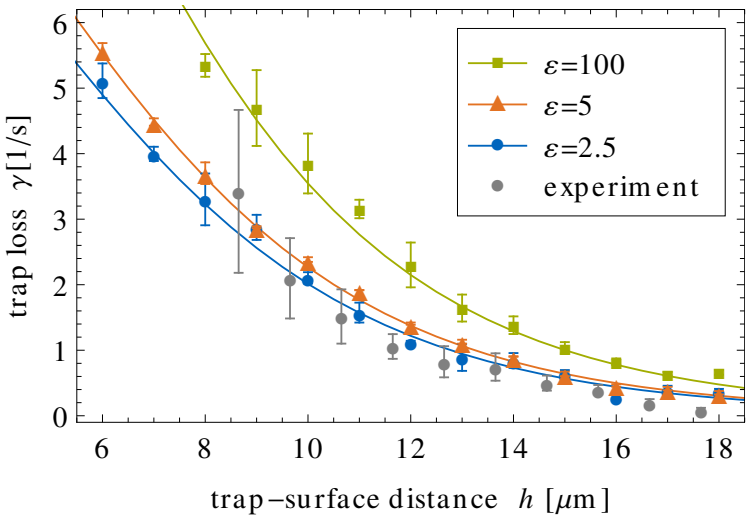

Figure 4.5: Trap loss γ for a thermal cloud of rubidium atoms overlapping with a carbon nanotube of dielectric constant $\epsilon = 2.5$ (blue), $\epsilon = 5$ (orange), and $\epsilon = 100$ (green). The geometry of the tube is chosen according to Ref. [49]. The solid lines show the trap loss obtained from a classical calculation via Eq. (4.2) and the atom-cylinder potential in the highly retarded thin-wire limit, as it is assumed for the classical three-dimensional time-dependent simulation (blue circles, orange triangles and green boxes and corresponding error bars). The calculated trap loss is in good agreement with the experimental results in [49] (grey circles and error bars) in particular for $\epsilon = 2.5$ and $\epsilon = 5$.

the surface of the nanochip. Nevertheless, the evaporative cooling at the surface of the nanochip causes the temperature of the cloud to vary with the distance of the trap-centre to the nanotube, which can be approximated linearly [108]

$$T = 12.4\,\mathrm{nK} + h \times 4.64\,\mathrm{nK}/\mu\mathrm{m}\,. \tag{4.8}$$

Numerical tests show that the van der Waals interaction of the atoms in the cloud with each other has no significant effect on the decay and can thus be neglected.

According to the Langevin model (see Section 1.2) the atoms are removed from the cloud when they reach the surface of the nanotube. Figure 4.4 shows the total number N of atoms in the cloud evolving in time t for different distances h of the cloud to the bottom of the nanotube on a logarithmic scale. The radius $R(z)$ from Eq. (4.3) and the length L of the nanotube are chosen in accordance with the experimental setup and the dielectric constant is $\epsilon = 5$. Temperature and trap frequencies are chosen according to Eqs. (4.5) and (4.8).

As expected from the experimental observation, the number of atoms in the cloud shows an exponential decay,

$$N(t) = N_0\,\mathrm{e}^{-\gamma t}\,. \tag{4.9}$$

By fitting Eq. (4.9) with $N_0 = 1000$ to the numerical outcome of the simulation (dashed lines in in Fig. 4.4) we obtain a loss rate γ, which is shown in Fig. 4.5 for different trap-

surface distances h and for a dielectric constant $\epsilon = 2.5$ (blue circles), $\epsilon = 5$ (orange triangles), and $\epsilon = 100$ (green squares). A meaningful estimate for the error of the decay rate γ from the classical simulation is obtained by generating many virtual simulation samples based on the simulated decay [108, 115]. These samples are randomly distributed around the exponential fit obtained from the simulation with the width of the spread is chosen to be the standard deviation of the simulated system from the exponential decay. Analysing and fitting these virtual samples (for the present analysis 25 samples are generated for each simulation) gives a standard deviation σ_γ of the decay constant γ obtained from the exponential fit. In accordance with Ref. [49] the error is estimated by $\Delta\gamma = 2\sigma_\gamma$ corresponding to a 95% confidence interval.

4.3 Absorption of a thermal cloud

The trap loss for a thermal cloud of rubidium atoms is shown in Fig. 4.5 and in Fig. 4.7. The density of the atoms in the thermal cloud is given by a Gaussian distribution [116],

$$n(x,y,z) = \frac{1}{(2\pi)^{3/2}\sigma_x\sigma_y\sigma_z} \exp\left[-\frac{x^2}{2\sigma_x^2} - \frac{y^2}{2\sigma_y^2} - \frac{z^2}{2\sigma_z^2}\right] , \tag{4.10}$$

with the σ_i given by the trap frequencies ω_i, the mass μ of a ^{87}Rb atom and temperature T of the cloud,

$$\sigma_i = \sqrt{\frac{k_B T}{\mu\omega_i^2}} . \tag{4.11}$$

The velocity of the atoms in a two-dimensional plane, perpendicular to the nanotube, is given by a Maxwell-Boltzmann distribution in two dimensions,

$$n_v(v) = \frac{v}{\sigma_v^2} \exp\left[-\frac{v^2}{2\sigma_v^2}\right] , \tag{4.12}$$

with σ_v given by the temperature T of the cloud from Eq. (4.8) and by the mass μ of the ^{87}Rb atoms,

$$\sigma_v = \sqrt{\frac{k_B T}{\mu}} . \tag{4.13}$$

For the experimental setup of Ref. [49], the values of σ_i and σ_v are $\sigma_x \approx 27\,\mu$m, $\sigma_y = \sigma_z \approx 5.5\,\mu$m and $\sigma_v \approx 3\,$mm/s with a weak dependence on the trap-surface distance h according to Eqs. (4.5) and (4.8). For the scattering of projectiles with a uniform velocity, the loss rate constant is simply given by the product of velocity v and absorption cross section λ_{abs} [117]. Taking into account the Maxwell-Boltzmann distribution, the loss rate constant of a thermal cloud of atoms is given by the thermal average

$$K_{\text{in}}^{\text{2D}} = \langle v_\perp \lambda_{\text{abs}}(v_\perp) \rangle , \tag{4.14}$$

where $v_\perp$ is the velocity in the plane perpendicular to the nanotube and λ_{abs} is the absorption cross section of an atom scattered at a cylinder or infinite length and radius $R(z)$.

4.3.1 Classical approach

In the classical Langevin model (see Section 1.2) the absorption cross section is given by $\lambda_{\mathrm{abs}}^{\mathrm{class}} = 2b_{\mathrm{c}}$ [see Eq. (1.35)]. The critical impact parameter b_{c} is determined by

$$V_{\mathrm{eff}}(r_0, b_{\mathrm{c}}) = E \qquad \text{and} \qquad \frac{\mathrm{d}}{\mathrm{d}r} V_{\mathrm{eff}}(r, b_{\mathrm{c}})\Big|_{r=r_0} = 0\,, \tag{4.15}$$

with the energy E of the incoming particle and the (classical) effective potential

$$V_{\mathrm{eff}} = \frac{\Lambda^2}{2\mu r^2} + V(r) = E\frac{b^2}{r^2} + V(r)\,, \tag{4.16}$$

given by the centrifugal potential $\Lambda^2/(2\mu r^2)$ and the interaction potential $V(r)$. For the special case of an attractive homogeneous potential $V(r) = -C_\alpha/r^\alpha$ (with $\alpha > 2$) the critical impact parameter b_{c} is [118].

$$\left(b_{\mathrm{c}}^{(\alpha)}\right)^\alpha = \frac{C_\alpha}{E}\ \frac{\alpha}{2}\left(1 - \frac{2}{\alpha}\right)^{1-\frac{\alpha}{2}}\,. \tag{4.17}$$

For the asymptotic Casimir-Polder potential of a thin-wire in the highly retarded limit of the atom-cylinder interaction, given in Eq. (2.30), the critical impact parameter is

$$b_{\mathrm{c}} = \left[\frac{9}{10\pi}\frac{(\varepsilon-1)(7\varepsilon+39)}{\varepsilon+1}\frac{\hbar^2}{\mu^2}\frac{\beta_{\mathrm{hr}}^2 R^2}{v^2}\right]^{1/6}\,, \tag{4.18}$$

which represents a characteristic atom-surface distance in the classical absorption process. For the system studied in Ref. [49], $R \ll b_{\mathrm{c}}$, which supports the assumption that the thin-wire limit is appropriate.

Figure 4.5 shows the trap loss γ as a function of the trap-nanochip distance h for the absorption of a cloud of thermal atoms by a nanotube with a dielectric constant of $\epsilon = 2.5$ (blue), $\epsilon = 5$ (orange), and $\epsilon = 100$ (green). The geometry of the tube is chosen according to Ref. [49], see Eq. (4.3). The trap loss obtained within the classical calculation via Eqs. (4.2), (4.14), and (4.18) perfectly reproduces the corresponding results from the three-dimensional classical simulation in Section 4.2 (blue circles, orange triangles, green squares and corresponding error bars). This supports the assumptions made for the calculation of the trap loss γ in Eq. (4.2) and confirms the validity of our approach, which is crucial for any further application of this method. Furthermore, the calculated trap loss is in good agreement with the experimental results from Ref. [49] (gray circles and error bars) in particular for $\epsilon = 2.5$ and $\epsilon = 5$ while $\epsilon = 100$ seems to overestimate the experimental results.

4.3.2 Quantum mechanical approach

Treating the absorption process quantum mechanically, the absorption cross section λ_{abs} for the single-atom scattering process in two dimensions, which enters the loss rate constant $K_{\mathrm{in}}^{\mathrm{2D}}$ in Eq. (4.14), has already been given in Eq. (1.23). The absorption cross section

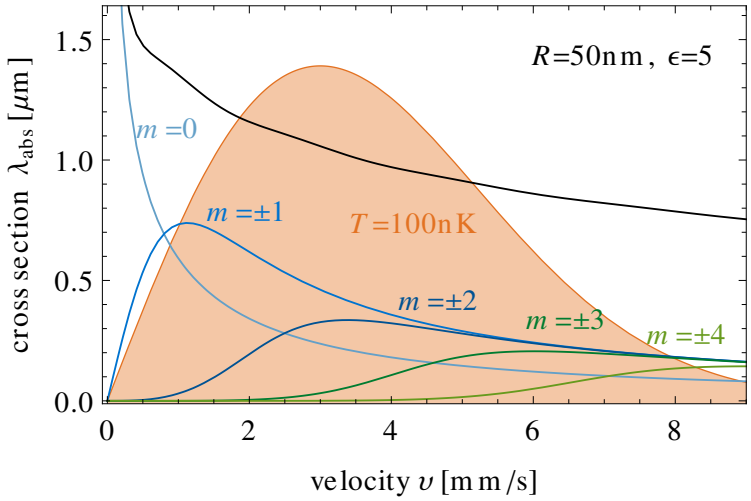

Figure 4.6: Absorption cross section for rubidium atoms scattered at a cylinder with a radius $R = 50\,\mathrm{nm}$ and a dielectric constant of $\epsilon = 5$. The black curve shows the full absorption cross section λ_{abs} including all contributing partial waves. The blue and green curves show the individual contribution of each partial wave from $m = 0$ (s wave) up to $|m| = 4$ (g wave). The orange region in the background shows the velocity distribution perpendicular to the tube (in arbitrary units) for a cloud of 100 nK.

λ_{abs} in two dimensions for rubidium atoms scattered by a cylinder of infinite length, radius $R = 50\,\mathrm{nm}$ and dielectric constant $\epsilon = 5$ is illustrated in Fig. 4.6. The cross section has been calculated using the full interaction potential, accurately represented via Eq. (2.34), which is close to the highly retarded, thin-wire limit (see discussion in Section 4.2). Similar results are obtained from both shape functions (2.36) and (2.37) and were averaged for the calculation of λ_{abs}. For a cloud with $T = 100\,\mathrm{nK}$, angular momenta up to the g wave ($|m| = 4$) contribute significantly to the absorption cross section λ_{abs} for the scattering at a cylinder with a radius of 50 nm, while higher partial waves ($|m| > 4$) are negligible. This is in contrast to simpler (classical) models as used in Ref. [49].

Figure 4.7 shows the trap loss γ for a thermal cloud of rubidium atoms absorbed by a carbon nanotube as a function of the trap-surface distance h. The trap loss obtained via Eq. (4.2) is based on a quantum mechanical calculation of the absorption cross section λ_{abs} for a cylinder with a frequency-independent dielectric constant $\epsilon = 2.5$ (dot-dashed line), $\epsilon = 5$ (solid line), and $\epsilon = 100$ (dashed line). The geometry of the cylinder is chosen in accordance with the one used in Ref. [49], see Eq. (4.3). The experimental data from Ref. [49] (full circles and error bars) are well reproduced by the calculated trap loss within the presented range of static dielectric constants from $\epsilon = 2.5$ (insulator) up to $\epsilon = 100$ (almost metallic). Although the dielectric properties of a multiwall carbon nanotube remain in general unknown, variations of a frequency-independent dielectric constant ϵ in this wide range of realistic values lead to rather small variations of the calculated results compared to the experimental error bars. Therefore a fit of a dielectric constant or a detailed knowledge of the dielectric properties is not essential to describe the experimental results in Ref. [49]. Explicit values of the trap loss γ are given in Tab. 4.1.

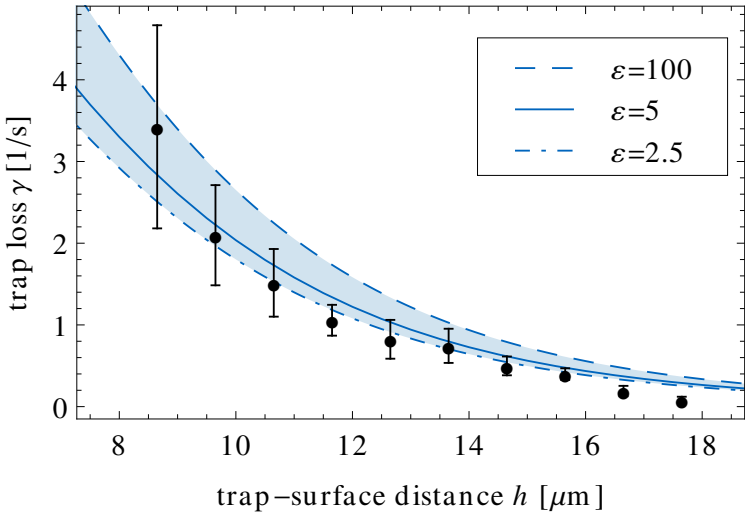

Figure 4.7: Trap loss γ for a thermal cloud of rubidium atoms overlapping with a carbon nanotube. The calculated trap loss (4.2) for a dielectric constant $\epsilon = 2.5$ (dot-dashed line), $\epsilon = 5$ (solid line) and $\epsilon = 100$ (dashed line) reproduces the data given in Ref. [49] (full circles and error bars) within this wide range of dielectric constants. Variations of ϵ in this range lead to rather small variations of the calculated results compared to the experimental error bars.

Table 4.1: Trap loss γ for a thermal cloud of rubidium atoms overlapping with a carbon nanotube at various trap surface distances h (see Fig. 4.1). The experimental data are taken from Ref. [49] and compared to a calculation via Eq. (4.2) for a cylinder with a dielectric constant ranging from $\epsilon = 2.5$, $\epsilon = 5$ up to $\epsilon = 100$.

h [μm]	γ [1/s]			
	Ref. [49]	$\epsilon = 2.5$	$\epsilon = 5$	$\epsilon = 100$
8.65	3.4244 ± 1.243	2.5084	2.8344	3.6952
9.65	2.0978 ± 0.61297	1.9664	2.2222	2.8946
10.65	1.5151 ± 0.41402	1.5293	1.7283	2.2477
11.65	1.0572 ± 0.18854	1.1832	1.3373	1.7354
12.65	0.82402 ± 0.23747	0.91318	1.0321	1.3358
13.65	0.74406 ± 0.209	0.70439	0.79616	1.0273
14.65	0.49852 ± 0.1151	0.54399	0.61488	0.79071
15.65	0.39782 ± 0.07116	0.42119	0.47611	0.61001
16.65	0.19073 ± 0.06343	0.32732	0.37002	0.47223
17.65	0.08692 ± 0.03413	0.25553	0.28889	0.36718

The comparison of the experimental data with the full quantum mechanical calculation and with the classical calculation shows a good agreement in both cases. The behaviour of the thermal cloud at $T \approx 100\,\mathrm{nK}$ can thus be considered to be essentially determined by classical dynamics.

4.4 Absorption of a Bose-Einstein condensate

In contrast to the classical behaviour of a thermal cloud, the scattering and absorption of a Bose-Einstein condensate at a carbon nanotube shows an extremely non-classical behaviour. The BEC is described by a macroscopic wave function in the ground state of the trap and the presence of an absorbing impurity inside of the cloud leads to a local depletion of its density. As a result, the condensate readjusts with the characteristic speed of sound v_s [119], which causes a flux toward the nanotube [120]. Due to the symmetry in the region close to the nanotube this flux is symmetric around the tube axis. Only s waves ($m = 0$) reflect this symmetry and contribute to the absorption cross section λ_abs. An additional factor of 2π, accounting for the isotropy of the incoming flux, needs to be considered and the loss rate constant thus is

$$K_\mathrm{in}^\mathrm{2D} = 2\pi\, v_\mathrm{s} \lambda_\mathrm{abs}^{(m=0)}(v_\mathrm{s})\,, \tag{4.19}$$

where $\lambda_\mathrm{abs}^{(m=0)}$ is the s-wave contribution to the absorption cross section in Eq. (1.23). The density of the BEC in a harmonic trap is given by a Thomas-Fermi distribution [119],

$$n(x,y,z) = \frac{15}{8\pi} \frac{1}{r_x^\mathrm{TF} r_y^\mathrm{TF} r_z^\mathrm{TF}} \,\mathrm{Max}\left[1 - \sum_{i=x,y,z} \left(\frac{i}{r_i^\mathrm{TF}}\right)^2, 0\right]\,, \tag{4.20}$$

with the characteristic Thomas-Fermi radii,

$$r_i^\mathrm{TF} = \sqrt{\frac{2\bar{\mu}}{\mu\omega_i^2}}\,, \tag{4.21}$$

depending on the mass μ of an atom, on the frequencies ω_i of the trap, given in Eq. (4.5), and on the chemical potential

$$\bar{\mu} = \frac{1}{2}\left(15\hbar^2 \mu^{1/2} N \omega_x \omega_y \omega_z a\right)^{2/5}\,, \tag{4.22}$$

where N is the total number of atoms in the Bose-Einstein condensate ($N = 10^4$ for the BEC in Refs. [49, 108]). The scattering length a describes the two-body interaction of the ^{87}Rb atoms inside of the condensate; $a = 5.77\,\mathrm{nm}$ for ^{87}Rb [4]. The Thomas-Fermi radii are $r_x^\mathrm{TF} \approx 16\,\mu\mathrm{m}$, $r_y^\mathrm{TF} = r_z^\mathrm{TF} \approx 3.2\,\mu\mathrm{m}$ for the experimental setup in Ref. [49] and show a weak dependence on the trap-surface distance h according to Eq. (4.5). The speed of sound in the Bose-Einstein condensate at the position of the nanotube is

$$v_\mathrm{s} = \sqrt{\frac{4\pi\hbar^2 a}{\mu^2}\, n(0,0,z)}\,, \tag{4.23}$$

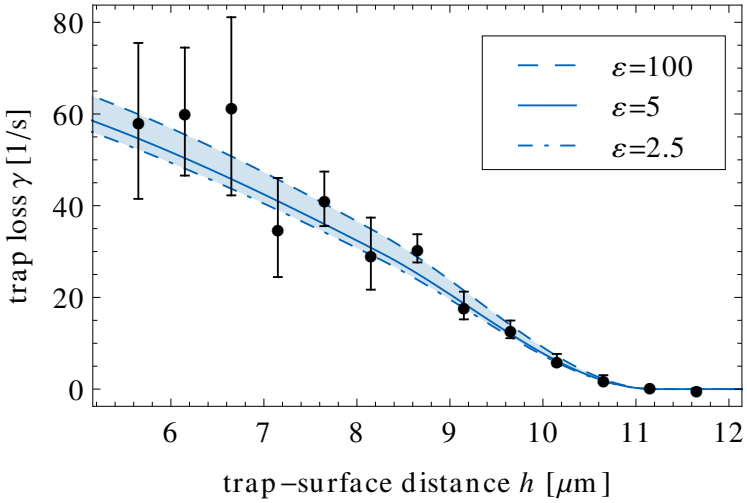

Figure 4.8: Trap loss γ for a Bose-Einstein condensate of rubidium atoms overlapping with a carbon nanotube. The calculated trap loss (4.2) for a dielectric constant $\epsilon = 2.5$ (dot-dashed line), $\epsilon = 5$ (solid line) and $\epsilon = 100$ (dashed line) reproduces the data given in [49] (full circles and error bars) within this wide range of dielectric constants. Variations of ϵ in this range lead to rather small variations of the calculated results compared to the experimental error bars.

depending on the density of the BEC, $n(x, y, z)$, from Eq. (4.20). As the number of atoms in the condensate decreases during the absorption process, the Thomas-Fermi radii and the speed of sound do not stay constant over time, which leads to an *algebraic* instead of an exponential decay for the loss of atoms from the condensate [120]. These corrections and possible fluctuations due to collective oscillations [49, 51] lie within the experimental error bars. The influence of the nanochip on the trap loss can be neglected for distances h larger than $5\,\mu$m (see Fig. 4 of Ref. [49]).

Figure 4.8 shows the trap loss γ for a Bose-Einstein condensate of rubidium atoms absorbed by a carbon nanotube as a function of the trap-surface distance h. The blue lines show the trap loss obtained via Eqs. (4.2) and (4.19) for a cylinder with a static dielectric constant $\epsilon = 2.5$ (dot-dashed line), $\epsilon = 5$ (solid line), and $\epsilon = 100$ (dashed line). The geometry of the cylinder is chosen according to Ref. [49], see Eq. (4.3). The experimental data from Ref. [49] (full circles and error bars) are in good agreement with the trap loss from Eq. (4.2) within the presented range of static dielectric constants from $\epsilon = 2.5$ (insulator) up to $\epsilon = 100$ (almost metallic). Similar to the absorption of a cloud of thermal atoms (see Section 4.3), variations of ϵ in this range of realistic values lead to rather small variations of the calculated results compared to the experimental error bars. A detailed knowledge of the dielectric properties of the nanotube is thus not essential to describe the experimental results. Explicit values of the trap loss γ are given in Tab. 4.2.

Table 4.2: Trap loss γ for a Bose-Einstein condensate of rubidium atoms overlapping with a carbon nanotube at various trap surface distances h (see Fig. 4.1). The experimental data are taken from Ref. [49] and compared to a calculation via Eq. (4.2) for a cylinder with a dielectric constant ranging from $\epsilon = 2.5$, $\epsilon = 5$ up to $\epsilon = 100$.

h [μm]	γ [1/s]			
	Ref. [49]	$\epsilon = 2.5$	$\epsilon = 5$	$\epsilon = 100$
5.65	58.4919 ± 17.0006	52.2367	54.6366	59.9341
6.15	60.5244 ± 13.9536	48.1012	50.3691	55.5232
6.65	61.6800 ± 19.4241	43.6912	45.8092	50.7757
7.15	35.2399 ± 10.7969	39.0479	40.9981	45.7287
7.65	41.4942 ± 5.9427	34.2219	35.987	40.429
8.15	29.5464 ± 7.8557	29.2726	30.836	34.9323
8.65	30.6964 ± 3.0729	23.8647	25.1851	28.7894
9.15	18.2332 ± 3.0207	17.6544	18.6616	21.5089
9.65	13.0319 ± 1.9203	11.3777	12.0453	13.9939
10.15	6.37320 ± 1.2982	5.81326	6.16358	7.2186
10.65	2.20710 ± 0.8167	1.75676	1.86547	2.20359
11.15	0.66406 ± 0	0.0154563	0.0164388	0.0195998
11.65	0.02674 ± 0.1837	0	0	0

4.5 Influence of retardation

The fundamental question of the influence of retardation on a scattering process has already been addressed in Section 3.2. The nature of the low-energy atom-cylinder scattering process has been characterised by the quantity $\xi_R(\rho)$, with $\xi_R(\rho) \ll 1$ ($\xi_R \gg 1$) if the scattering process is dominated by the non-retarded (highly retarded) limit. For the present system the characteristic value $\xi_R(\rho)$ ranges from $\xi_R(\rho) \approx 10$ ($\epsilon = 2.5$ and $R = 20\,\text{nm}$) up to $\xi_R(\rho) \approx 100$ ($\epsilon = 100$ and $R = 137.5\,\text{nm}$). The scattering process is thus dominated by the highly retarded limit of the Casimir-Polder interaction, as it has been assumed in the classical description of the hybrid system in Section 4.2. However, it remains unclear whether the effect of retardation becomes important in the description of the trap loss in a realistic hybrid system.

4.5.1 Influence of retardation on the absorption of a BEC

The absorption of a Bose-Einstein condensate by a nanotube is a highly non-classical process and due to the symmetry of the scattering process only s waves contribute to the absorption cross section and thus to the trap loss γ. The s-wave contribution to the absorption cross section is related to the reflection probability P_R for the s wave via Eq. (1.23). For s waves the effective potential $V_{\text{eff}}(r)$ in Eq. (1.11) is purely attractive and reflection is classically forbidden. However, the reflection probability, in particular in the low-energy regime, is governed by quantum mechanical effects and the reflection probability reaches unity for $k \to 0$. If k becomes much larger than the inverse characteristic length scale $1/\beta$ of the potential, or equivalently if $k\beta$ becomes larger than unity, the reflection probability

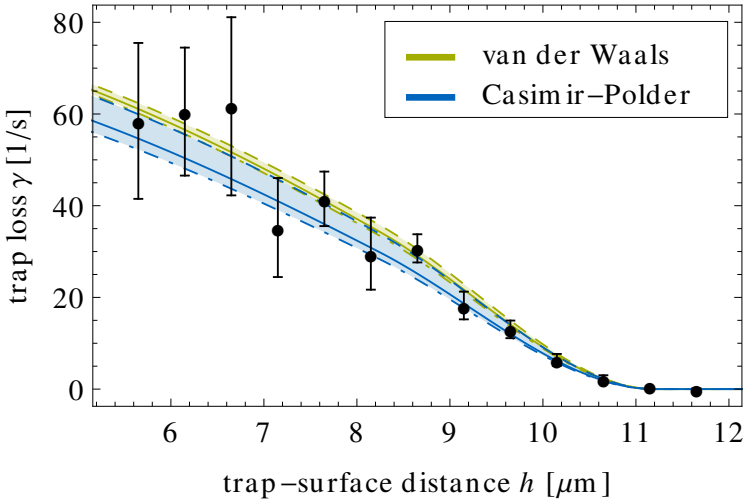

Figure 4.9: Influence of retardation on the trap loss γ for a Bose-Einstein condensate of rubidium atoms. The loss rates has been calculated via Eq. (4.2) based on the full Casimir-Polder potential (blue curves) and on the non-retarded van der Waals potential only, where retardation effects are neglected (green curves). The shaded area shows loss rates for dielectric constant of the nanotube in a regime from $\varepsilon = 2.5$ (dot-dashed line) up to $\varepsilon = 100$ (dashed line). The solid line shows the trap loss for a dielectric constant of $\varepsilon = 5$. The differences between the results obtained by using the full potential or the van der Waals potential are rather small and cannot be resolved with in the experimental data [49] (full circles).

vanishes.

For the present system, the velocity of the incoming wave is given by the speed of sound $v_s \approx 8\text{mm/s}$ which corresponds to $k \approx 1.1/\mu\text{m}$. In the non-retarded limit of the atom-cylinder interaction $k\beta_{\text{nr}} \approx 243$ while in the highly retarded limit $k\beta_{\text{hr}} \approx 4.8$. In both cases $k\beta_{\text{nr/hr}} > 1$ and the reflection probability P_R is small. Therefore almost all incoming flux is absorbed and the absorption cross section reaches its limit, $\lambda_{\text{abs}}^{(m=0)} \to 1/k$, given in Eq. (1.23). This is true in particular for the non-retarded limit where k is significantly larger than the inverse characteristic length $1/\beta_{\text{nr}}$.

Figure 4.9 shows the trap loss γ from a Bose-Einstein condensate obtained for the non-retarded limit of the Casimir-Polder interaction (green lines) as well as from the full Casimir-Polder potential (blue lines). The results, that have been obtained using only the highly retarded limit of the interaction (not shown in Fig. 4.9), are almost indistinguishable from the results obtained by using the full potential. For the non-retarded limit of the potential, where $k\beta_{\text{nr}} \gg 1$, the absorption cross section $\lambda_{\text{abs}}^{(m=0)}$ is close to its $1/k$ limit and thus the trap loss shows almost no dependence on the Casimir-Polder potential and thus on the dielectric properties of the cylinder. In the highly retarded limit where $1 < k\beta_{\text{hr}} < k\beta_{\text{nr}}$ the reflection probability is slightly larger compared to the non-retarded case and the trap loss thus depends slightly on the dielectric constant ϵ. However, in both cases $\lambda_{\text{abs}}^{(m=0)}$ is close to its $1/k$ limit and the differences between the loss rates obtained from the van der Waals potential and from the full Casimir-Polder potential are rather small. Thus, the

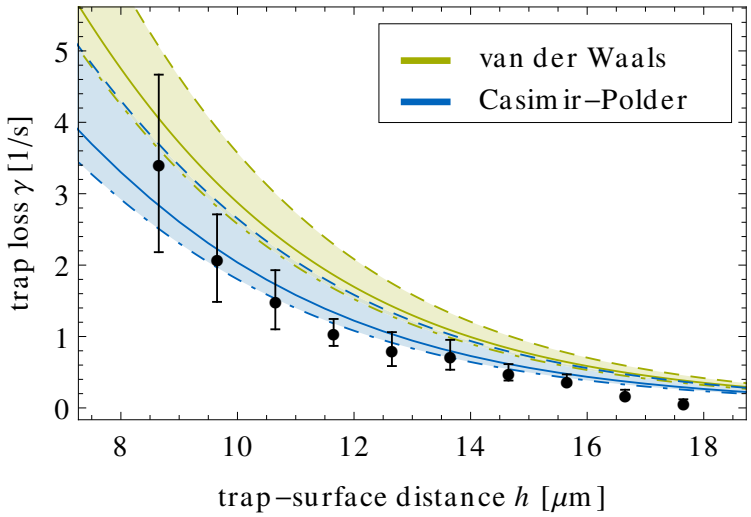

Figure 4.10: Influence of retardation on the trap loss γ for a thermal cloud of rubidium atoms. The loss rate γ has been calculated via Eq. (4.2) based on the full Casimir-Polder potential (blue curves) and on the non-retarded van der Waals potential only, where retardation effects are neglected (green curves). The shaded area shows loss rates for dielectric constant of the nanotube in a regime from $\varepsilon = 2.5$ (dot-dashed line) up to $\varepsilon = 100$ (dashed line). The solid line shows the trap loss for a dielectric constant of $\varepsilon = 5$. The experimental data [49] (full circles) clearly deviate from the prediction calculated with the van der Waals potential only.

effect of retardation is not resolvable by the experimental measurement (black circles and error bars) in the given range of dielectric constants $2.5 \leq \epsilon \leq 100$.

The difference between the results obtained from the non-retarded and from the full or highly retarded potential is more pronounced for a smaller speed of sound v_s, which leads to an increasing reflection probability P_R. This can be realized by exchanging the atom-type and lowering the density of the condensate.

4.5.2 Influence of retardation on the absorption of a thermal cloud

For a thermal cloud the (mean) velocity of the atoms is even larger than the speed of sound in the Bose-Einstein condensate and the (quantum) reflection probability of the s wave is almost zero. However, for the absorption of a thermal cloud several partial waves contribute to the absorption cross section (see Section 4.3). For $|m| \geq 1$ the corresponding effective potential $V_{\text{eff}}(r)$ in Eq. (1.11) is no longer purely attractive, and the reflection probabilities are > 0, even for $k\beta > 1$. The reflection probabilities and therefore the absorption cross section λ_{abs} thus depends crucially on the Casimir-Polder interaction potential.

Figure 4.10 shows the trap loss γ for a thermal cloud obtained from the non-retarded limit of the Casimir-Polder interaction (green lines) as well as from the full Casimir-Polder potential (blue lines). In contrast to the BEC, the non-retarded van der Waals potential fails to describe the trap loss (green lines), within a wide range of dielectric constants from $\epsilon = 2.5$ (dot-dashed line), $\epsilon = 5$ (solid line) up to $\epsilon = 100$ (dashed line). The results

obtained with the full Casimir-Polder potential (blue lines) match the experimental data (black circles and error bars) within the same range of dielectric constants. The trap loss obtained from the highly retarded limit of the Casimir-Polder potential (not shown in Fig. 4.10) is almost indistinguishable from the result from the full interaction potential.

The trap loss of a thermal cloud presented in Fig. 4.10 shows that retardation effects can play a crucial role in realistic hybrid systems. In the system studied by Schneeweiss *et al.* [49] the scattering process is dominated by the highly retarded limit of the interaction and retardation effects can be resolved within the experimental measurements. Furthermore, it is feasible to explore the transition regime or even the non-retarded limit of the atom-cylinder interaction. For helium atoms in the metastable 2^1S state and a cylinder with $R = 32\,\mathrm{nm}$ (for $\epsilon = 100$) or $R = 131\,\mathrm{nm}$ (for $\epsilon = 2.5$) the transition zone between the non-retarded and highly retarded limit of the Casimir-Polder interaction governs the scattering process, see Eq. (3.30). Nanotubes of these dimensions (or even with lower radii) are accessible for experimental setups and offer a practicable tool to probe the different regimes of the Casimir-Polder potential.

Summary

In this chapter, an accurate parameter-free ab-initio description of the trap loss in a hybrid system consisting of a single carbon nanotube immersed in an ultracold atomic quantum gas has been presented. An accurate description of this hybrid system is achieved with a proper description of the underlying scattering process (see Chapter 3) together with the exact Casimir-Polder potential of an atom facing an infinite dielectric cylinder (see Chapter 2). Our approach has proven its validity within a three-dimensional, time-dependent classical simulation of a thermal cloud of atoms, where we have precise control over the hybrid system and could verify the assumptions made in our ansatz (Section 4.2).

A classical and quantum mechanical calculation of the trap loss from a thermal cloud of atoms, has been found to be in good agreement with recent experiments by Schneeweiss *et al.* [49] (Section 4.3). The trap loss from a Bose-Einstein condensate, which shows an extremely non-classical behaviour, is obtained within a quantum mechanical calculation of the absorption cross section and leads to perfect agreement with the experiments results of Ref. [49] (Section 4.4).

Furthermore, it has been shown that the non-retarded van der Waals potential fails to reproduce the loss rates of a thermal cloud of atoms and that retardation effects that are accounted for in the Casimir-Polder potential need to be considered. For a BEC, the influence of retardation effects on the trap loss are rather small an not resolvable within the experimental uncertainty of Ref. [49] (Section 4.5).

In contrast to previous attempts [49, 51] to describe the results of Ref. [49], the present approach gives insight into the underlying processes, offers a basis for extensions to more complex hybrid systems and therefore promotes a deeper understanding of hybrid systems, which is essential for the design of future nanodevices.

Chapter 5

Conclusions and Outlook

In this thesis a detailed analysis of the fundamental hybrid quantum system consisting of ultracold atoms interacting with a cylindrical geometry has been presented. It has been shown that a proper description of this seemingly simple system is a non-trivial problem due to the two-dimensional nature of the scattering process and due to the intricacy of the Casimir-Polder interaction potential. A reliable approach needs to take into account both, the reduced dimensionality of the system and the exact interaction potential.

The scattering and absorption in an (effectively) two-dimensional system is described within the two-dimensional scattering theory, which has been presented in Chapter 1. The scattering of atoms at solid-state structures can be separated into elastic dynamics and reactive processes, constituting an elastic and an inelastic channel. The concept of an elastic cross section and absorption cross section has been introduced to describe the scattering in these channels. Particular attention has been given to the low-energy regime, where the two-dimensional scattering process differs significantly from its better-known one- or three-dimensional counterparts. The low-energy scattering process is dominated by the scattering of the s wave and can be characterised by the complex scattering length $\mathfrak{a}$. The dynamics of the scattering process at large distances is governed by the long-range Casimir-Polder potential. At short atom-surface separations the interaction becomes complicated and remains in general unknown. However, inelastic or reactive collisions are practically certain in this regime. This short-range behaviour is properly described by the Langevin model [58] leading to total absorption at the surface. In a quantum mechanical picture this is ensured by the use of incoming boundary conditions. This allows an accurate, model-independent description of the complicated short-range behaviour.

The long-range Casimir-Polder interaction between a polarisable atom and a cylindrical geometry, which was first derived by Nabutovskii *et al.* [48], has been presented in Chapter 2. The crucial difference at large atom-surface separations between the interaction of an atom with a dielectric (insulating) cylinder or with a perfectly conducting (metallic) tube has already been emphasised by Barash and Kyasov [84]. However, we have shown that the potential derived in Ref. [48] accurately describes both cases as long as the limit of perfect conductivity is treated properly. Particular attention has been given to the non-retarded and to the highly retarded limit of the Casimir-Polder potential where retardation can either be neglected or is dominant. In these limits the potential substantially simplifies and allows an accurate numerical evaluation, as shown in Appendix A. Furthermore, the behaviour of the Casimir-Polder potential at large and small distances

has been discussed. In the limit of short atom-surface separations $(r - R)$, the curvature of the cylinder becomes unimportant and the potential resembles the well-known interaction of an atom facing a plane surface. At large distances of the atom from the cylinder, the interaction potential shows a significantly different behaviour for the interaction of atoms with a perfect conductor and with a dielectric cylinder. In a realistic situation, the Casimir-Polder potential undergoes a smooth transition from the non-retarded limit at small distances to the highly retarded limit at large distances. A proper description of the full potential has been presented within a generalised shape-function approach. This method has been shown to be reliable and has successfully been applied to the Casimir-Polder potential of a ground-state hydrogen atom interacting with a perfectly conducting cylinder.

These first two chapters form the basis for a dependable approach to describe the scattering and absorption of ultracold atoms at a nanowire, taking properly into account the two-dimensional nature of the scattering process as well as the exact Casimir-Polder interaction. This scattering process has been analysed in Chapter 3. The scattering and absorption of ultracold atoms has been studied by analysing the behaviour of the complex scattering length $\mathfrak{a}$, which characterises the scattering process in the low-energy regime. The scattering length has been calculated numerically and analytical expressions in the limit of a thin and of a thick wire have been derived. In the limit of large radii, $R \to \infty$, the real part of the scattering length is determined by the position of the surface of the cylinder while the imaginary part resembles the one-dimensional scattering process of an atom reflected from a plane surface, governed by the corresponding Casimir-Polder potential. For small radii, $R \to 0$, the behaviour of the scattering length reflects the crucial dependence of the asymptotic behaviour of the Casimir-Polder potential on whether the cylinder is dielectric or perfectly conducting. For a dielectric cylinder, the modulus $|\mathfrak{a}|$ of the scattering length is $\propto (R^2\beta_{\mathrm{nr}})^{1/3}$ in the non-retarded, and $\propto (R\beta_{\mathrm{hr}})^{1/2}$ in the highly retarded limit. In contrast, the low-energy scattering of atoms at a perfect conductor shows a logarithmic dependence on the radius R; the modulus $|\mathfrak{a}|$ of the scattering length is, in leading order, approximately proportional to $[\ln(R/\beta_{\mathrm{nr}})]^{-1}$ in the non-retarded, and to $[\ln(R/\beta_{\mathrm{hr}})]^{-1/2}$ in the highly retarded limit.

In a realistic scenario, the Casimir-Polder potential undergoes a smooth transition between the non-retarded limit at short distances to the highly retarded limit at large atom-surface separations. We have introduced the quantity $\xi_R(\rho)$, which characterises the nature of the atom-cylinder scattering process in the low-energy regime. In the thick-wire limit, the scattering process resembles the reflection of an atom from a plane surface, and is thus governed by the highly retarded limit [25, 28]. This still holds for a thin, perfectly conducting cylinder. However, for a dielectric tube the scattering process undergoes a smooth transition between the highly retarded limit and the non-retarded limit and can be dominated by the latter for sufficiently small radii. The key to understanding this behaviour of the scattering process is given by the comparison of the characteristic length scales of the transition zone with the characteristic length scales of the asymptotic behaviour of the potential, which crucially depend on whether the cylinder is dielectric or perfectly conducting.

Furthermore, we have compared the diffraction of light to the scattering of ultracold atoms at a cylindrical geometry. Both scattering processes are described by the scattering of (electromagnetic or matter) waves. However, the latter case is governed by the Casimir-

Polder dispersion force acting between the atom and the solid-state surface, while the former one is determined solely by the boundary conditions at the surface of the cylinder. For a thick cylinder, $R \to \infty$, the scattering of matter waves resembles the diffraction of an electromagnetic wave and thus constitutes the electromagnetic limit of the scattering process. In contrast, the scattering of atoms at a thin cylinder, $R \to 0$, differs significantly from the electromagnetic result and is thus called the non-electromagnetic limit.

The thorough understanding of the fundamental scattering process of a single atom scattered at a cylindrical geometry forms the basis for understanding hybrid systems of higher complexity. In Chapter 4 the results obtained in the previous chapters have been applied to the quantum hybrid system constituted by a carbon nanotube immersed in a cold quantum gas, such as a Bose-Einstein condensate or a thermal cloud of atoms. A dependable approach has been derived, which accurately relates the trap loss coefficient of this hybrid system to the absorption cross section of the underlying scattering process. This approach has proven its validity within a three-dimensional, time-dependent classical simulation of a thermal cloud of atoms, which gives precise control over the hybrid system and where the assumptions made in our approach have been shown to be valid. A quantum mechanical calculation of the trap loss is found to be in perfect agreement with recent experimental results obtained by Schneeweiss *et al.* [49] for a thermal cloud of ^{87}Rb atoms, governed mainly by classical dynamics, and for a Bose-Einstein condensate, which shows an extremely non-classical behaviour.

Particular attention has also been given to the influence of retardation on the observed trap loss. Consistently with the results of Chapter 3, the absorption is governed by the highly retarded limit of the Casimir-Polder potential. Nevertheless, the effect of retardation cannot be resolved by the absorption of the Bose-Einstein condensate. However, the non-retarded van der Waals potential fails to reproduce the trap loss of a thermal cloud of atoms and retardation effects that are accounted for in the Casimir-Polder potential need to be considered. The well-founded approach to describe this system gives insight into the underlying processes and therefore promotes a deeper understanding of hybrid systems of higher complexity.

Outlook

The present work has focused on the fundamental hybrid system of an atom interacting with a cylindrical geometry and on the corresponding scattering and absorption processes. This forms the basis for a thorough understanding and for the design of nanowire based hybrid quantum systems of higher complexity.

We have shown that the radius of the cylinder can serve as a control knob to tune the regime of the interaction potential, which dominates the scattering process, in particular for an insulating tube. This offers a practicable tool to study the Casimir-Polder potential at various distances. It has been shown that the experimental results of Ref. [49] give insight into the highly retarded limit of the interaction; however, the transition zone or the non-retarded limit can be studied in similar setups.

Furthermore, the scattering of atoms at a nanotube forms the basis for an accurate description of the diffraction of matter waves at a nanograting, which is used for the diffraction and interference of atoms or large molecules [13, 14]. We have shown the

existence of an electromagnetic and a non-electromagnetic limit for the scattering at a single nanowire. Therefore, for an array of nanotubes forming a diffraction grating, the diffraction of atoms in the electromagnetic limit resembles the diffraction of light, while in the non-electromagnetic limit, it might serve as further a tool to study the properties of the Casimir-Polder interaction and its influence on the diffraction of matter waves at nanogratings.

Recent progress in the field of microfabrication techniques has brought forth mesoscopic structures with a mechanical degree of freedom, such as a nanomechanical oscillator [121]. This leads to a new type of quantum hybrid systems, coupling an atomic system to a mechanical degree of freedom [21]. Hybrid systems of a single atom or an atomic sample, coupled to a mechanical oscillator via Casimir-Polder dispersion forces have been proposed [40] and the excitation of a Bose-Einstein condensate by an oscillating nanotube has already been shown, using a simplified model potential [51]. On the basis of the present work an accurate description of the scattering and absorption of atoms by an oscillating nanowire can be developed.

A thorough understanding of the scattering and absorption of ultracold atoms by nanotubes, which has been studied in the present work, forms the basis for extensions to various nanowire-based hybrid systems of higher complexity, which is essential for the design of future nanodevices.

Appendix A

Accurate Treatment of the Atom-Cylinder Potential

The Casimir-Polder interaction between an atom and a cylindrical geometry, which has been discussed in detail in Chapter 2 has, in general, a very complicated form [see Eq. (2.2)]. Nevertheless, it can be substantially simplified in the non-retarded (see Chapter 2.2) and highly retarded limit (see Chapter 2.3). An explicit evaluation remains a non-trivial task and requires a sophisticated treatment in order to reproduce the correct behaviour for all atom-surface distances $0 < d < \infty$.

A.1 Accurate treatment of the non-retarded limit

For any explicit evaluation of the interaction potential (2.14) in the non-retarded limit, the summation over n, from $-\infty$ to $+\infty$, needs to be truncated. From the low-argument behaviour of the modified Bessel functions, it follows that the terms with $n \neq 0$ in Eq. (2.14) behave as $1/\varrho^{2|n|}$ for large distances of the atom to the surface of the cylinder, $\varrho \to \infty$, with $\varrho = r/R$. The $n = 0$ term behaves as $1/\varrho^2$ for an dielectric cylinder with a finite dielectric constant ϵ and behaves as $1/\ln(\varrho)$ in the case of a perfectly conducting tube. At small distances of the atom to the surface, $\varrho \to 1$ or equivalently $d/R \to 0$, each term in the sum in Eq. (2.14) behaves as (d/R), regardless of the index n.

The truncation of the summation over n in Eq. (2.14) to a finite range from $-n_{\max}$ to $+n_{\max}$, approximates the non-retarded potential exactly up to terms of $\mathcal{O}(1/\varrho^{4+2n_{\max}})$ for large distances but is a poor approximation close to the surface of the cylinder where all terms contribute equally. A detailed discussion of the consequences of such a truncation, in particular for the scattering of ultracold atoms, is given in Ref. [42, 47, 95] for the special case of a perfectly conducting cylinder. An improvement suggested in Ref. [92], for a perfectly conducting cylinder, involves explicitly retaining the $n = 0$ term and treating the residual sum with the help of the uniform large-order approximation for the Bessel functions [59]. Here we generalise this ansatz for a cylinder with arbitrary dielectric properties. In contrast to Ref. [92], we allow an arbitrary finite number of terms to be retained in the sum in Eq. (2.14) and apply the large-order approximation to the residual sum containing terms with $|n| > n_{\max}$. Hence, the non-retarded atom-cylinder potential

is

$$V_{\rm nr}(r) = -\frac{\hbar^2}{2\mu}\frac{\beta_{\rm nr}}{d^3}\left\{ \sum_{n=-n_{\max}}^{+n_{\max}} \int_0^\infty {\rm d}x\, x^2 \frac{(\epsilon-1)}{\pi}\left[\epsilon\frac{K_n(x_1)}{I_n(x_1)} - \frac{K_n'(x_1)}{I_n'(x_1)}\right]^{-1} \times \right.$$
$$\left. \left[K_n^{'2}(\varrho x_1) + \left(\frac{n^2}{\varrho^2 x_1^2}+1\right) K_n^2(\varrho x_1)\right] + X_{\rm nr}^{n_{\max}}(r)\right\}. \quad \text{(A.1)}$$

Notice that the terms in Eq. (2.14) only depend on $n^2 = |n|^2$ and the residual contribution thus is,

$$X_{\rm nr}^{n_{\max}}(r) = \frac{2(\epsilon-1)}{\pi}\sum_{n=\nu}^{+\infty}\int_0^\infty {\rm d}x\, x^2 \frac{(\epsilon-1)}{\pi}\left[\epsilon\frac{K_n(x_1)}{I_n(x_1)} - \frac{K_n'(x_1)}{I_n'(x_1)}\right]^{-1} \times$$
$$\left[K_n^{'2}(\varrho x_1) + \left(\frac{n^2}{\varrho^2 x_1^2}+1\right) K_n^2(\varrho x_1)\right] \quad \text{(A.2)}$$

with $\nu = n_{\max}+1$. Changing the integration variable to $\xi = \varrho x_1/n$ gives

$$X_{\rm nr}^{n_{\max}}(r) = \frac{2(\epsilon-1)}{\pi}\left(\frac{\varrho-1}{\varrho}\right)^3 \sum_{n=\nu}^{+\infty}\int_0^\infty {\rm d}\xi\, n^3 \left[\epsilon\frac{K_n(n\xi/\varrho)}{I_n(n\xi/\varrho)} - \frac{K_n'(n\xi/\varrho)}{I_n'(n\xi/\varrho)}\right]^{-1} \times$$
$$\left[\xi^2 K_n^{'2}(n\xi) + (1+\xi^2)K_n^2(n\xi)\right]. \quad \text{(A.3)}$$

Using the uniform large-order approximation of the Bessel functions; see Eqs. (9.7.7)-(9.7.11) of Ref. [59]

$$I_n(nz) \approx \frac{1}{\sqrt{2\pi n}}\frac{{\rm e}^{mn\zeta}}{(1+z^2)^{1/4}}, \qquad I_n'(nz) \approx \frac{1}{\sqrt{2\pi n}}\frac{{\rm e}^{m\zeta}}{z}\left(1+z^2\right)^{1/4}, \quad \text{(A.4a)}$$

$$K_n(nz) \approx \sqrt{\frac{\pi}{2n}}\frac{{\rm e}^{-n\zeta}}{(1+z^2)^{1/4}}, \qquad K_n'(nz) \approx -\sqrt{\frac{\pi}{2n}}\frac{{\rm e}^{-n\zeta}}{z}\left(1+z^2\right)^{1/4}, \quad \text{(A.4b)}$$

with

$$\zeta(z) = \sqrt{1+z^2} + \ln\left(\frac{z}{1+\sqrt{1+z^2}}\right). \quad \text{(A.4c)}$$

The residual sum contribution in Eq. (A.3) thus simplifies to

$$X_{\rm nr}^{n_{\max}}(r) = \frac{2}{\pi}\frac{(\epsilon-1)}{(\epsilon+1)}\left(\frac{\varrho-1}{\varrho}\right)^3 \sum_{n=\nu}^{+\infty}\int_0^\infty {\rm d}\xi\, n^2 A(\xi,\varrho)^n \sqrt{1+\xi^2}\,, \quad \text{(A.5)}$$

where A is a function of the integration variable ξ and of the ratio $\varrho = r/R$,

$$A(\xi,\varrho) = \varrho^{-2}{\rm e}^{-2\left(\sqrt{1+\xi^2}-\sqrt{1+\xi^2/\varrho^2}\right)}\left(\frac{1+\sqrt{1+\xi^2}}{1+\sqrt{1+\xi^2/\varrho^2}}\right)^2. \quad \text{(A.6)}$$

The integration and the summation in Eq. (A.5) commute, which allows an explicit evaluation of the sum. This yields

$$X_{\rm nr}^{n_{\max}}(r) = \frac{2}{\pi}\frac{(\epsilon-1)}{(\epsilon+1)}\left(\frac{\varrho-1}{\varrho}\right)^3 \int_0^\infty {\rm d}\xi\, J_2(\nu,\xi,\varrho)\sqrt{1+\xi^2}\,. \quad \text{(A.7)}$$

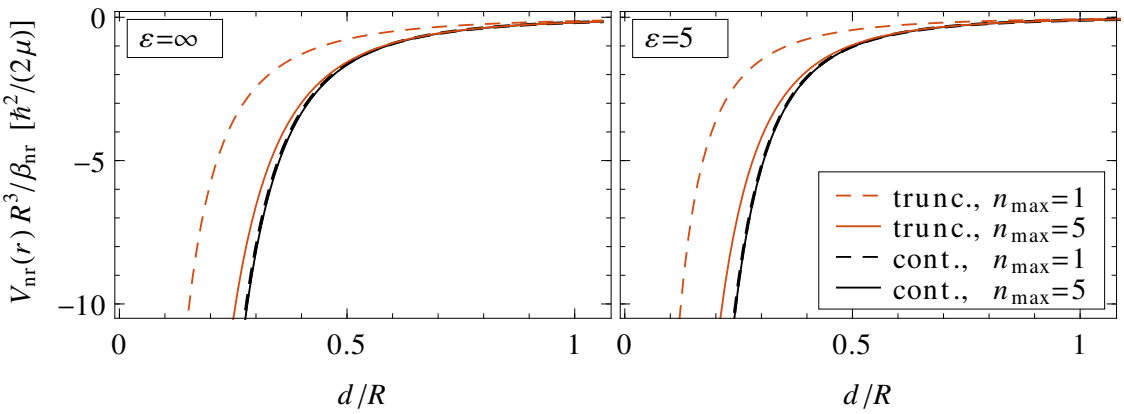

Figure A.1: Numerical calculation of the non-retarded atom-cylinder potential for a perfectly conducting cylinder (left panel) and for a cylinder with dielectric constant $\epsilon = 5$ (right panel). The solid black line shows the result of the approximation via Eqs. (A.1) and (A.9), where the contributions in Eqs. (2.14) and (2.15) are included exactly for $|n| \leq 5$, while terms with higher $|n|$ are approximated via the uniform large-order behaviour of the Bessel functions according to Eqs. (A.7) and (A.10). The dashed black line shows the corresponding result for $n_{\max} = 1$ which is almost indistinguishable from the approximation with $n_{\max} = 5$. The orange dashed (solid) line shows results obtained when the sum in Eqs. (2.14) and (2.15) is truncated after $n_{\max} = 1$ ($n_{\max} = 5$) and the contribution from $|n| > 1$ ($|n| > 5$) are neglected. Notice that the expression $V_{\mathrm{nr}}(r)R^3/\beta_{\mathrm{nr}}$ depends only on the dimensionless ratio d/R and the dielectric constant ϵ.

The function J_2 is given by

$$J_2(\nu,\xi,\varrho) = \sum_{n=\nu}^{+\infty} n^2 A^n = \frac{A^\nu \left(A^2(\nu-1)^2 + A\left(1+2\nu-2\nu^2\right)+\nu^2\right)}{(1-A)^3}\,. \tag{A.8}$$

This defines a hierarchy of approximations to the exact atom-wire potential with levels characterised by the index $n_{\max}$ up to which the terms in the sum in Eq. (2.14) are included exactly. For the case of a dielectric cylinder, the lowest meaningful index is $n_{\max} = 1$, as the terms in with $n = 0$ and $|n| = 1$ in Eq. (2.14) are of the same $\mathcal{O}(1/\varrho^2)$ at large distances.

In the special case of a perfectly conducting cylinder, $\epsilon \to \infty$ (see also Ref. [42, 47, 95]), the approximation of the full potential in Eq. (A.1) simplifies to

$$V_{\mathrm{nr}}^{\epsilon\to\infty}(r) = -\frac{\hbar^2}{2\mu}\frac{\beta_{\mathrm{nr}}}{d^3}\left\{\sum_{n=-n_{\max}}^{+n_{\max}}\int_0^\infty \mathrm{d}x\, x^2 \frac{1}{\pi}\frac{I_n(x_1)}{K_n(x_1)}\times \right.$$
$$\left.\left[K_n'^2(\varrho x_1) + \left(\frac{n^2}{\varrho^2 x_1^2}+1\right)K_n^2(\varrho x_1)\right] + X_{\mathrm{nr},\epsilon\to\infty}^{n_{\max}}(r)\right\}. \tag{A.9}$$

and the residual contribution yields

$$X_{\mathrm{nr},\epsilon\to\infty}^{n_{\max}}(r) = \frac{2}{\pi}\left(\frac{\varrho-1}{\varrho}\right)^3 \int_0^\infty \mathrm{d}\xi\; J_2(\nu,\xi,\varrho)\sqrt{1+\xi^2}\,. \tag{A.10}$$

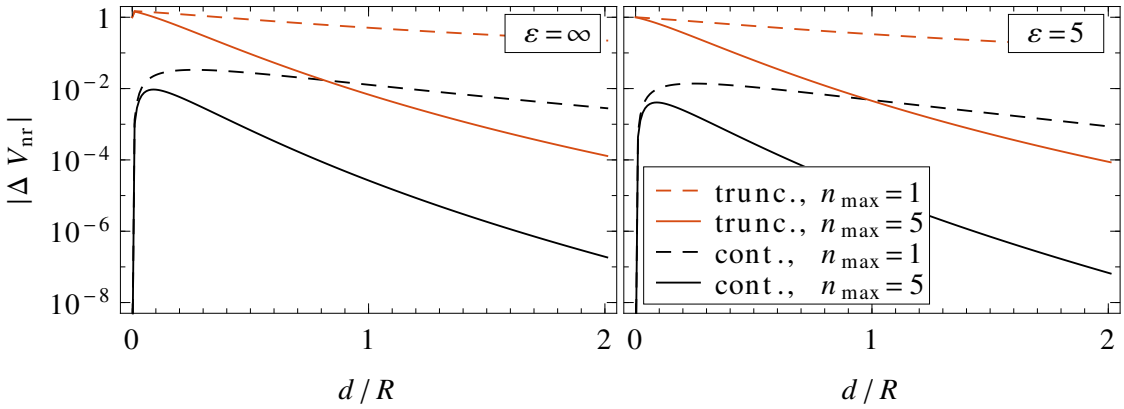

Figure A.2: Absolute value of the relative deviation of various approximations to the atom-cylinder potential V_{nr} in the non-retarded limit for a perfectly conducting cylinder (left panel) and a dielectric cylinder with $\epsilon = 5$ (right panel). The black dashed line is the result of approximations (A.1) and (A.9), when only the $n = 1$ contributions are included exactly, while the sums are continued to higher $|n|$ via the uniform large-order approximation of the Bessel functions according to Eqs. (A.10) and (A.7). The orange dashed (solid) line shows the result obtained by truncating the sum after $n_{\max} = 1$ ($n_{\max} = 5$) and neglecting contributions from $|n| > 1$ ($|n| > 5$).

In contrast to the potential of a dielectric cylinder, Eq. (A.9) is also applicable for $n_{\max} = 0$ and the leading contribution to the potential (2.15), given solely by the $n = 0$ term, is proportional to $1/(r^3 \ln \varrho)$ for large values of ϱ.

The approximations (A.1) and (A.9) smoothly converge to the exact potentials (2.14) and (2.15) in the limit $n_{\max} \to \infty$. At large distances, $d/R \to \infty$, the behaviour of the non-retarded potential, is treated exactly up to and including therms of $\mathcal{O}(1/\varrho^{4+2n_{\max}})$. In contrast to a simple truncation where terms with $|n| > n_{\max}$ are neglected, the behaviour of the potential close to the surface, $d/R \to 0$, is also included properly, as all terms – all of them are of $\mathcal{O}(d/R)$ – are taken into account exactly ($|n| \leq n_{\max}$) or approximately ($|n| > n_{\max}$).

Figure A.1 shows numerical results for the non-retarded potential $V_{\mathrm{nr}}(r)$ obtained in various approximations for a perfectly conducting cylinder (left panel) and for a cylinder with a dielectric constant $\epsilon = 5$ (right panel), which gives typical results. For $n_{\max} \geq 2$, the potential, accurately approximated via Eqs. (A.1) and (A.9), has converged to a relative accuracy better than 1% in the whole range $0 < d/R < \infty$. Even for $n_{\max} = 1$, Eqs. (A.1) and (A.9) approximate the exact potential quite well, as shown by the dashed black line in Fig. A.1, and are almost indistinguishable from the results obtained for higher $n_{\max}$, e.g., $n_{\max} = 5$ (solid black line in Fig. A.1). However, truncating the sum in Eqs. (2.14) and (2.15) without including the contributions of the residual terms even approximately gives a poor approximation, in particular if only contributions up to $n_{\max} = 1$ are included. Increasing the number of terms included exactly seems to give better results (solid orange line in Fig. A.1 with $n_{\max} = 5$). Nevertheless, neglecting the contribution of terms with

$|n| > n_{\max}$ always fails to approximate the potential close to the surface as all terms contribute equally in this limit. To illustrate this, Fig. A.2 shows the relative deviation,

$$\Delta V_{\mathrm{nr}}(r) = \frac{V_{\mathrm{nr}}^{\mathrm{approx}}(r) - V_{\mathrm{nr}}(r)}{V_{\mathrm{nr}}(r)} \tag{A.11}$$

of various approximations $V_{\mathrm{nr}}^{\mathrm{approx}}(r)$ to the exact non-retarded atom-cylinder potential $V_{\mathrm{nr}}(r)$ for a perfectly conducting cylinder (left panel) and for a dielectric cylinder (right panel). The dielectric constant of the cylinder is chosen to be $\epsilon = 5$. The relative deviations of the approximations in Eqs. (A.1) and (A.9) are on the order of a few percent for $n_{\max} = 1$ (black dashed line) and better than 1% for $n_{\max} = 5$ (black solid line) in the whole range $0 < d < \infty$. Neglecting contributions from terms with $|n| \geq n_{\max}$ gives a rather poor approximation, in particular for $n_{\max} = 1$ where the relative deviations approache unity (solid orange line). By increasing the number of included terms the relative deviation decreases for large values of d/R but always reaches unity for $d/R \to 0$. Thus the behaviour of the non-retarded potential close to the surface of the cylinder is not reproduced correctly by truncating the sum in Eqs. (2.14) and (2.15) at a finite $n_{\max}$, while an approximate treatment of the terms with $|n| > n_{\max}$ according to Eqs. (A.1) and (A.9) describes the potential accurately in the whole range $0 < d < \infty$, in particular for $d/R \to 0$ where the approximations (A.1) and (A.9) become exact (see black lines in Fig. A.2).

A.2 Accurate treatment of the highly retarded limit

For an explicit evaluation of the Casimir-Polder potential (2.22) in the highly retarded limit, the sum over n, from $-\infty$ to $+\infty$, needs to be truncated. Analysing the behaviour of the contributing terms of the sum in Eq. (2.22) shows a behaviour similar to that of the non-retarded case. For large distances of the atom to the surface of the cylinder, $\varrho = r/R \to \infty$, terms with $n \neq 0$ in Eq. (2.22) behave as $1/\varrho^{2|n|}$. The $n = 0$ term behaves as $1/\varrho^2$ for an dielectric cylinder with a finite dielectric constant ϵ and behaves asymptotically as $1/\ln(\varrho)$ in the case of a perfect conductor. At small atom-surface separations, $\varrho \to 1$ or equivalently $d/R \to 0$, each term in the sum in Eq. (2.22) behaves as (d/R), regardless of the index n.

A truncation of the infinite sum in Eq. (2.22) to a finite range from $-n_{\max}$ to $+n_{\max}$ is needed to enable an explicit evaluation of the highly retarded potential. This truncated potential is exact up to and including terms of $\mathcal{O}(1/\varrho^{5+2n_{\max}})$ for large distances. Close to the surface of the cylinder all terms contribute equally and neglecting the truncated terms is a poor approximation.

We follow the idea presented for the proper approximation of the non-retarded limit, presented in Appendix A.1, and truncate the sum in Eq. (2.22) to a finite range from $-n_{\max}$ to $+n_{\max}$ while the residual sum, containing terms with $|n| > n_{\max}$ is included via the uniform large-order behaviour of the modified Bessel functions [59]. Doing so, the highly retarded atom-cylinder potential is

$$\begin{aligned} V_{\mathrm{hr}}(r) = -\frac{\hbar^2}{2\mu}\frac{2\beta_{\mathrm{hr}}^2}{\pi^2 d^4}\Bigg\{ \sum_{n=-n_{\max}}^{+n_{\max}} \int_0^\infty \mathrm{d}q \int_0^\infty \mathrm{d}x \, \frac{I_n(z_1)}{\delta_0^0 \, K_n(z_1)} K_n^2(\varrho z_1) \Big\{ q^2 \left(\delta_1^0 + \delta_0^1\right) \\ + \left(x^2\delta_1^0 - q^2\delta_0^1\right)\left(\frac{n^2}{\varrho^2 z_1^2} + 1 + \Phi_n^2(\varrho z_1)\right) \\ + 4n^2\varrho^{-1}q_1^4 x^2 z_2^2(\epsilon - 1)\Phi_n(\varrho z_1)\left[\Phi_n(z_1) - \Psi_n(z_1)\right] \Big\} + X_{\mathrm{hr}}^{n_{\max}} \Bigg\}. \end{aligned} \tag{A.12}$$

By changing the integration variables to $\chi = x/n$ and $\eta = q/n$ and using the uniform large-order behaviour of the modified Bessel functions, Eq. (A.4a) - (A.4c), the contribution of the residual sum simplifies to

$$\begin{aligned} X_{\mathrm{hr}}^{n_{\max}} = 2\sum_{n=\nu}^{+\infty} \int_0^\infty \mathrm{d}\chi \int_0^\infty \mathrm{d}\eta \, n^3 A^n \frac{1}{\sqrt{1+\xi^2}} \Bigg\{ \frac{\eta^2}{2}\left(\frac{\gamma_1^0}{\gamma_0^0} + \frac{\gamma_0^1}{\gamma_0^0}\right) \\ + \frac{\xi^2+1}{\xi^2}\left(\chi^2\frac{\gamma_1^0}{\gamma_0^0} - \eta^2\frac{\gamma_0^1}{\bar{\delta}_0^0}\right) + \frac{4\eta_1^4\chi^2\xi_2^2(\epsilon-1)}{\gamma_0^0}\frac{\sqrt{1+\xi^2}\sqrt{1+\xi^2/\varrho^2}}{\xi^2} \Bigg\} \end{aligned} \tag{A.13}$$

where $\nu = n_{\max} + 1$ and the following abbreviation have been introduced,

$$\xi = \frac{\varrho\sqrt{\chi^2+\eta^2}}{\varrho - 1}, \qquad \xi_2 = \frac{\sqrt{\chi^2+\epsilon\eta^2}}{\varrho - 1}, \tag{A.14a}$$

$$\eta_1 = \frac{\eta}{\varrho - 1} = q_1/n, \qquad \chi_1 = \frac{\chi}{\varrho - 1} = x_1/n, \tag{A.14b}$$

$$\gamma_0^0 \approx [\chi_1\eta_1^2(\epsilon-1)]^2 + [\eta_1\xi_2\xi/\varrho]^2\left(\bar{\Psi}_{12}+\bar{\Psi}_{21}\right)\left(\epsilon\bar{\Psi}_{12}+\bar{\Psi}_{21}\right), \tag{A.14c}$$

$$\gamma_1^0 \approx [\chi_1\eta_1^2(\epsilon-1)]^2 + [\eta_1\xi_2\xi/\varrho]^2\left(\bar{\Psi}_{12}+\bar{\Psi}_{21}\right)\left(\epsilon\bar{\Psi}_{12}-\bar{\Psi}_{21}\right), \tag{A.14d}$$

$$\gamma_0^1 \approx [\chi_1\eta_1^2(\epsilon-1)]^2 + [\eta_1\xi_2\xi/\varrho]^2\left(\bar{\Psi}_{12}-\bar{\Psi}_{21}\right)\left(\epsilon\bar{\Psi}_{12}+\bar{\Psi}_{21}\right), \tag{A.14e}$$

$$\bar{\Psi}_{ik} \approx \bar{z}_i\frac{\sqrt{1+\bar{z_k}^2}}{\bar{z}_k}, \tag{A.14f}$$

which do not depend on the summation index n. The quantity A is a function of the of the ratio $\varrho = r/R$ and ξ which depends on the integration variable χ and η,

$$A(\xi,\varrho) = \varrho^{-2}\mathrm{e}^{-2\left(\sqrt{1+\xi^2}-\sqrt{1+\xi^2/\varrho^2}\right)}\left(\frac{1+\sqrt{1+\xi^2}}{1+\sqrt{1+\xi^2/\varrho^2}}\right)^2. \tag{A.15}$$

The integration and the summation in Eq. (A.13) commute and an explicit execution of the sum gives

$$X_{\mathrm{hr}}^{n_{\max}} = \int_0^\infty \mathrm{d}\chi \int_0^\infty \mathrm{d}\eta\; J_3(\nu,\xi,\varrho)\frac{2}{\sqrt{1+\xi^2}}\left\{\frac{\eta^2}{2}\left(\frac{\gamma_1^0}{\gamma_0^0}+\frac{\gamma_0^1}{\gamma_0^0}\right)\right.$$
$$\left. + \frac{\xi^2+1}{\xi^2}\left(\chi^2\frac{\gamma_1^0}{\gamma_0^0}-\eta^2\frac{\gamma_0^1}{\bar{\delta}_0^0}\right) + \frac{4\eta_1^4\chi^2\xi_2^2(\epsilon-1)}{\gamma_0^0}\frac{\sqrt{1+\xi^2}\sqrt{1+\xi^2/\varrho^2}}{\xi^2}\right\}. \tag{A.16}$$

The function J_3 is given by,

$$J_3(\nu,\xi,\varrho) = \sum_{n=\nu}^{+\infty} n^3A^n =$$
$$\frac{A^\nu\left(A\left(1+3\nu+3\nu^2-3\nu^3\right)+A^2\left(4-6\nu^2+3\nu^3\right)-A^3\left(\nu-1\right)^3+\nu^3\right)}{\left(1-A\right)^4}. \tag{A.17}$$

This defines a hierarchy of approximations of the exact highly retarded atom-cylinder potential with levels characterised by $n_{\max}$ up to which the terms in Eq. (2.22) are included exactly. The lowest useful approximation in the case of a dielectric cylinder is obtained for $n_{\max} = 1$ as the $n = 0$ term and the terms with $|n| = 1$ are of the same order.

In the special case of a perfectly conducting cylinder, $\epsilon \to \infty$ the approximation of the full potential in Eq. (A.12) simplifies to

$$V_{\mathrm{hr}}^{\epsilon\to\infty}(r) = -\frac{\hbar^2}{2\mu}\frac{\beta_{\mathrm{hr}}^2}{2\pi d^4}\left\{\sum_{n=-n_{\max}}^{+n_{\max}}\int_0^\infty \mathrm{d}z\, z^3\left(\frac{I_n(z_1)}{K_n(z_1)}\left[K_n^{'2}(\varrho z_1)+\left(\frac{n^2}{\varrho^2 z_1^2}+2\right)K_n^2(\varrho z_1)\right]\right.\right.$$
$$\left.\left. - \frac{I_n^{'}(z_1)}{K_n^{'}(z_1)}\left[K_n^{'2}(\varrho z_1)+\frac{n^2}{\varrho^2 z_1^2}K_n^2(\varrho z_1)\right]\right) + X_{\mathrm{hr},\epsilon\to\infty}^{n_{\max}}\right\}. \tag{A.18}$$

and the residual contribution yields

$$X_{\mathrm{hr},\epsilon\to\infty}^{n_{\max}} = 4\left(\frac{\varrho-1}{\varrho}\right)^4\int_0^\infty \mathrm{d}\xi\; J_3(\nu,\xi,\varrho)\xi\sqrt{1+\xi^2}, \tag{A.19}$$

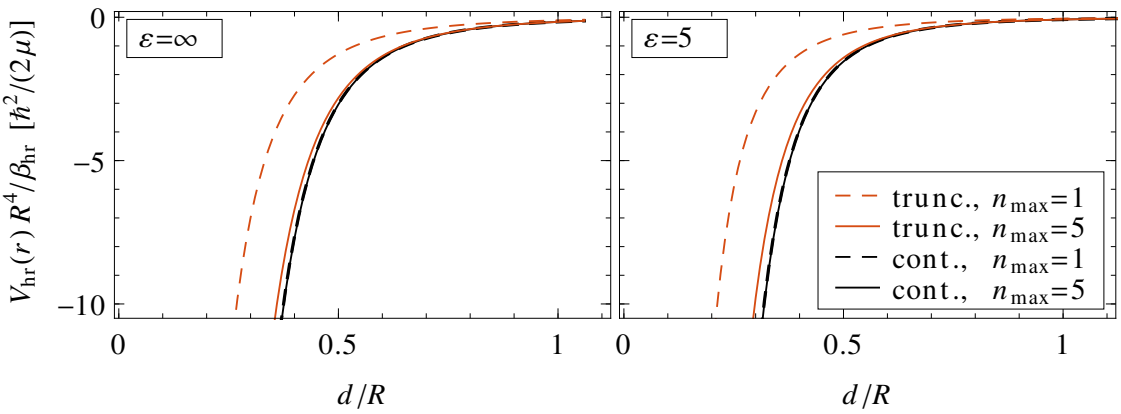

Figure A.3: Numerical calculation of the highly retarded atom-cylinder potential for a perfectly conducting cylinder (left panel) and a cylinder with dielectric constant $\epsilon = 5$ (right panel). The solid black line shows the result of the approximation via Eqs. (A.12) and (A.18), where the contributions in Eqs. (2.22) and (2.23) are included exactly for $|n| \leq 5$ while terms with higher $|n|$ are approximated via the uniform large-order behaviour of the Bessel functions according to Eqs. (A.16) and (A.19). The dashed black line shows the corresponding result for $n_{\max} = 1$ which is almost indistinguishable from the approximation with $n_{\max} = 5$. The orange dashed (solid) line shows results obtained when the sum in Eqs. (2.22) and (2.23) is truncated after $n_{\max} = 1$ ($n_{\max} = 5$) and the contribution from $|n| > 1$ ($|n| > 5$) are neglected. Notice that the expression $V_{\mathrm{nr}}(r)R^3/\beta_{\mathrm{nr}}$ depends only on the dimensionless ratio d/R and the dielectric constant ϵ.

In contrast to the case of a dielectric cylinder, Eq. (A.18) is also applicable for $n_{\max} = 0$ and the leading contribution to the potential (2.23), given solely by the $n = 0$ term, is proportional to $1/(r^4 \ln \varrho)$ for large values of ϱ.

For increasing values of $n_{\max}$, the approximations (A.12) and (A.18) converge smoothly to the exact potentials (2.22) and (2.23) in the limit $n_{\max} \to \infty$. The exact potential is treated exactly up to and including terms of $\mathcal{O}(1/\varrho^{5+2n_{\max}})$ at large distances ($d/R \to \infty$) and Eqs. (A.12) and (A.18) reproduce the behaviour of the potential close to the surface ($d/R \to 0$) properly, as contributions of all terms are considered at least approximately.

Figure A.3 shows numerical results for the atom-cylinder potential $V_{\mathrm{hr}}(r)$ in the highly retarded limit obtained in various approximations for a perfectly conducting cylinder (left panel) and for a dielectric cylinder with $\epsilon = 5$ (right panel). The approximation (A.12) and (A.18) of the highly retarded potential has converged to a relative accuracy better than 1% even for $n_{\max} = 1$ (dashed black line) and is essentially indistinguishable from results obtained for higher $n_{\max}$, e.g., $n_{\max} = 5$ (solid black line). Truncating the sum in Eqs. (2.22) and (2.23) without including the contributions of the residual terms approximately gives a rather poor approximation, shown by the dashed orange line ($n_{\max} = 1$) and the solid orange line ($n_{\max} = 5$).

Although the result for $n_{\max} = 5$ seems to give better results an approximate treatment where contributions from terms with $|n| > n_{\max}$ are neglected cannot reproduce the

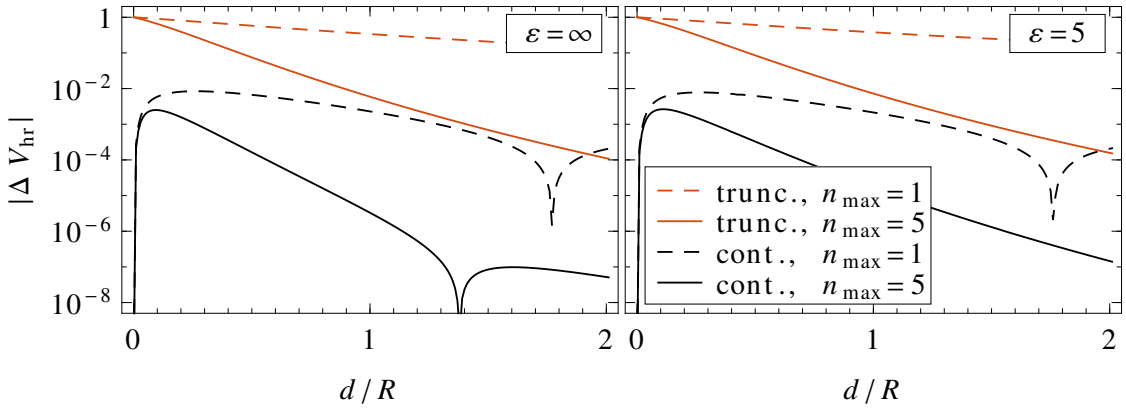

Figure A.4: Absolute value of the relative deviation of various approximations to the atom-cylinder potential $V_{\rm hr}$ in the highly retarded limit for a perfectly conducting cylinder (left panel) and a dielectric cylinder with $\epsilon = 5$ (right panel). The black dashed line is the result of approximations (A.12) and (A.18), when only the $n = 1$ contributions are included exactly, while the sums are continued to higher $|n|$ via the uniform large-order approximation of the Bessel functions according to Eqs. (A.16) and (A.19). The orange dashed (solid) line shows the result obtained by truncating the sum after $n_{\rm max} = 1$ ($n_{\rm max} = 5$) and neglecting contributions from $|n| > 1$ ($|n| > 5$).

potential close to the surface correctly. This is illustrated in Fig. A.4 where the relative deviations (A.11) of various approximations of the highly retarded limit are shown. While the deviations of the proper approximations in Eqs. (A.12) or (A.18) are below 1% for $n_{\rm max} = 1$ (dashed black line) and for $n_{\rm max} = 5$ (solid black line), the result of a simple truncation, where higher terms with $|n| > n_{\rm max}$ are neglected, gives an deviation of order unity for $n_{\rm max} = 1$ (dashed orange line). Including more terms (e.g., $n_{\rm max} = 5$, solid orange line) reduces the deviation but still fails in the limit $d/R \to 0$ where the relative deviation approaches unity.

Bibliography

[1] S. Chu, *Nobel Lecture: The manipulation of neutral particles*, Reviews of Modern Physics **70**, 685 (1998).

[2] C. N. Cohen-Tannoudji, *Nobel Lecture: Manipulating atoms with photons*, Reviews of Modern Physics **70**, 707 (1998).

[3] W. D. Phillips, *Nobel Lecture: Laser cooling and trapping of neutral atoms*, Reviews of Modern Physics **70**, 721 (1998).

[4] F. Dalfovo, S. Giorgini, and S. Stringari, *Theory of Bose-Einstein condensation in trapped gases*, Reviews of Modern Physics **71**, 463 (1999).

[5] W. Ketterle, D. S. Durfee, and D. M. Stamper-Kurn, *Making, probing and understanding Bose-Einstein condensates*, in *Proceedings of the Internation School of Physics Enrico Fermi* (1999).

[6] J. Fortágh and C. Zimmermann, *Magnetic microtraps for ultracold atoms*, Reviews of Modern Physics **79**, 235 (2007).

[7] R. Grimm, M. Weidemüller, and Y. B. Ovchinnikov, *Optical dipole traps for neutral atoms*, Advances in Atomic, Molecular, and Optical Physics **42**, 95 (2000).

[8] R. Folman and P. Krüger, *Microscopic atom optics: from wires to an atom chip*, Advances in Atomic, Molecular, and Optical Physics **48**, 263 (2002).

[9] R. Folman, P. Kruger, D. Cassettari, B. Hessmo, *et al.*, *Controlling cold atoms using nanofabricated surfaces: atom chips*, Physical Review Letters **84**, 4749 (2000).

[10] J. Fortágh and C. Zimmermann, *Toward atom chips*, Science **307**, 860 (2005).

[11] B. Bhushan (editor), *Springer Handbook of Nanotechnology* (Springer Verlag, Berlin, 2004).

[12] P. J. F. Harris, *Carbon Nanotube Science* (Cambridge University Press, Cambridge, 2009).

[13] M. Arndt, O. Nairz, J. Vos-Andreae, C. Keller, *et al.*, *Wave-particle duality of C_{60} molecules*, Nature **401**, 680 (1999).

[14] T. Juffmann, S. Truppe, P. Geyer, A. G. Major, *et al.*, *Wave and particle in molecular interference lithography*, Physical Review Letters **103**, 263601 (2009).

[15] T. Pasquini, M. Saba, G.-B. Jo, Y. Shin, *et al.*, *Low velocity quantum reflection of Bose-Einstein condensates*, Physical Review Letters **97**, 093201 (2006).

[16] T. Pasquini, Y. Shin, C. Sanner, M. Saba, *et al.*, *Quantum reflection from a solid surface at normal incidence*, Physical Review Letters **93**, 223201 (2004).

[17] R. H. Baughman, A. A. Zakhidov, and W. A. de Heer, *Carbon nanotubes – the route toward applications*, Science **297**, 787 (2002).

[18] M. Wallquist, K. Hammerer, P. Rabl, M. D. Lukin, *et al.*, *Hybrid quantum devices and quantum engineering*, Physica Scripta **T 137**, 014001 (2009).

[19] A. Sørensen, C. H. van der Wal, L. I. Childress, and M. D. Lukin, *Capacitive coupling of atomic systems to mesoscopic conductors*, Physical Review Letters **92**, 063601 (2004).

[20] L. Tian and P. Zoller, *Coupled ion-nanomechanical systems*, Physical Review Letters **93**, 266403 (2004).

[21] K. Hammerer, M. Wallquist, C. Genes, M. Ludwig, *et al.*, *Strong coupling of a mechanical oscillator and a single atom*, Physical Review Letters **103**, 063005 (2009).

[22] D. DeMille, J. M. Doyle, M. D. Lukin, S. E. Maxwell, *et al.*, *A coherent all-electrical interface between polar molecules and mesoscopic superconducting resonators*, Nature Physics **2**, 636 (2006).

[23] H. B. G. Casimir and D. Polder, *The influence of retardation on the London-van der Waals forces*, Physical Review **73**, 360 (1948).

[24] G. L. Klimchitskaya and V. M. Mostepanenko, *The Casimir force between real materials: Experiment and theory*, Reviews of Modern Physics **81**, 1827 (2009).

[25] F. Shimizu, *Specular reflection of very slow metastable neon atoms from a solid surface*, Physical Review Letters **86**, 987 (2001).

[26] J. E. Lennard-Jones, *Processes of adsorption and diffusion on solid surfaces*, Transactions of the Faraday Society **28**, 333 (1932).

[27] H. Friedrich, G. Jacoby, and C. G. Meister, *Quantum reflection by Casimir-van der Waals potential tails*, Physical Review A **65**, 032902 (2002).

[28] H. Friedrich and A. Jurisch, *Quantum reflection of metastable hydrogen atoms by a conducting surface*, Physics Letters A **335**, 43 (2005).

[29] H. Oberst, Y. Tashiro, K. Shimizu, and F. Shimizu, *Quantum reflection of He* on silicon*, Physical Review A **71**, 052901 (2005).

[30] H. Oberst, D. Kouznetsov, K. Shimizu, J.-i. Fujita, *et al.*, *Fresnel diffraction mirror for an atomic wave*, Physical Review Letters **94**, 013203 (2005).

[31] B. S. Zhao, S. Schulz, S. Meek, G. Meijer, *et al.*, *Quantum reflection of helium atom beams from a microstructured grating*, Physical Review A **78**, 010902 (2008).

[32] A. Husain, J. Hone, H. W. C. Postma, X. M. H. Huang, *et al.*, *Nanowire-based very-high-frequency electromechanical resonator*, Applied Physics Letters **83**, 1240 (2003).

[33] R. Salem, Y. Japha, J. Chabé, B. Hadad, *et al.*, *Nanowire atomchip traps for submicron atomsurface distances*, New Journal of Physics **12**, 023039 (2010).

[34] B. Lassagne, Y. Tarakanov, J. Kinaret, D. Garcia-Sanchez, *et al.*, *Coupling mechanics to charge transport in carbon nanotube mechanical resonators*, Science **325**, 1107 (2009).

[35] Z. F. Ren, Z. P. Huang, D. Z. Wang, J. G. Wen, *et al.*, *Growth of a single freestanding multiwall carbon nanotube on each nanonickel dot*, Applied Physics Letters **75**, 1086 (1999).

[36] V. I. Merkulov, D. H. Lowndes, Y. Y. Wei, G. Eres, *et al.*, *Patterned growth of individual and multiple vertically aligned carbon nanofibers*, Applied Physics Letters **76**, 3555 (2000).

[37] A. R. Harutyunyan, G. Chen, T. M. Paronyan, E. M. Pigos, *et al.*, *Preferential growth of single-walled carbon nanotubes with metallic conductivity*, Science **326**, 116 (2009).

[38] J. Yuan, H. Schmalz, Y. Xu, N. Miyajima, *et al.*, *Room-temperature growth of uniform tellurium nanorods and the assembly of tellurium or Fe_3O_4 nanoparticles on the nanorods*, Advanced Materials **20**, 947 (2008).

[39] M. Gierling, P. Schneeweiss, G. Visanescu, P. Federsel, *et al.*, *Cold-atom scanning probe microscopy*, Nature nanotechnology **6**, 446 (2011).

[40] O. Kálmán, T. Kiss, J. Fortágh, and P. Domokos, *Quantum galvanometer by interfacing a vibrating nanowire and cold atoms*, Nano Letters (2011).

[41] M. Fink, J. Eiglsperger, J. Madroñero, and H. Friedrich, *Influence of retardation in the scattering of ultracold atoms by conducting nanowires*, Physical Review A **85**, 040702(R) (2012).

[42] M. Fink, A. Naranjo, F. Arnecke, J. Eiglsperger, *et al.*, *s-wave scattering of a polarizable atom by an absorbing nanowire*, Physical Review A **81**, 062714 (2010).

[43] I. R. Lapidus, *Quantum-mechanical scattering in two dimensions*, American Journal of Physics **50**, 45 (1982).

[44] B. J. Verhaar, J. P. H. W. van den Eijnde, M. A. J. Voermans, and M. M. J. Schaffrath, *Scattering length and effective range in two dimensions: application to adsorbed hydrogen atoms*, Journal of Physics A **17**, 595 (1984).

[45] S. K. Adhikari, *Quantum scattering in two dimensions*, American Journal of Physics **54**, 362 (1986).

[46] F. Arnecke, H. Friedrich, and P. Raab, *Near-threshold scattering, quantum reflection, and quantization in two dimensions*, Physical Review A **78**, 052711 (2008).

[47] M. Fink, J. Eiglsperger, H. Friedrich, and J. Madroñero, *Scattering of ultracold atoms by an absorbing nanowire*, The European Physical Journal D **63**, 33 (2011).

[48] V. M. Nabutovskii, V. R. Belosludov, and A. M. Korotkikh, *Interaction potential between small neutral particles and spherical or cylindrical surfaces*, Sov. Phys. JETP **50**, 352 (1979).

[49] P. Schneeweiss, M. Gierling, G. Visanescu, D. P. Kern, *et al.*, *Dispersion forces between ultracold atoms and a carbon nanotube*, Nature nanotechnology **7**, 515 (2012).

[50] M. Fink, T.-O. Müller, J. Eiglsperger, and J. Madroñero, *Interaction of atomic quantum gases with a single carbon nanotube*, Europhysics Letters **102**, 33001 (2013).

[51] B. Jetter, J. Märkle, P. Schneeweiss, M. Gierling, *et al.*, *Scattering and absorption of ultracold atoms by nanotubes*, arXiv 1205.6161v1 (2012).

[52] H. Friedrich, *Theoretical Atomic Physics* (Springer Verlag, Berlin, 2005), 3rd edition.

[53] P. G. Burke, *Potential scattering in atomic physics* (Plenum Press, New York, 1977).

[54] C. J. Joachain, *Quantum Collision Theory* (North-Holland Publishing Company, Amsterdam, 1975).

[55] B. Simon and M. Reed, *Scattering Theory* (Academic Press, San Diego, 2001).

[56] J. R. Taylor, *Scattering Theory* (John Wiley & Sons, New York, 1972).

[57] R. G. Newton, *Scattering Theory of Waves and Particles* (Springer Verlag, Berlin, 1982).

[58] P. Langevin, *Sur une formule fondamentale de la théorie cinétique*, Annales de chimie et de physique, 8th ser. **5**, 245 (1905).

[59] M. Abramowitz and I. A. Stegun, *Handbook of Mathematical Functions: with Formulas, Graphs, and Mathematical Tables* (Dover Publications, New York, 1965).

[60] S. K. Adhikari and W. Gibson, *Low-energy behavior of few-particle scattering amplitudes in two dimensions*, Physical Review A **46**, 3967 (1992).

[61] M. Rzepka, P. Lamp, and M. A. de La Casa-Lillo, *Physisorption of hydrogen on microporous carbon and carbon nanotubes*, The Journal of Physical Chemistry B **102**, 10894 (1998).

[62] J. Zhao, A. Buldum, J. Han, and J. P. Lu, *Gas molecule adsorption in carbon nanotubes and nanotube bundles*, Nanotechnology **13**, 195 (2002).

[63] P. Chen, X. Wu, J. Lin, and K. L. Tan, *High H_2 uptake by alkali-doped carbon nanotubes under ambient pressure and moderate temperatures*, Science **285**, 91 (1999).

[64] H. Ulbricht, G. Moos, and T. Hertel, *Physisorption of molecular oxygen on single-wall carbon nanotube bundles and graphite*, Physical Review B **66**, 075404 (2002).

[65] D. Clougherty and W. Kohn, *Quantum theory of sticking*, Physical Review B **46**, 4921 (1992).

[66] G. Gioumousis and D. P. Stevenson, *Reactions of gaseous molecule ions with gaseous nolecules. V. Theory*, The Journal of Chemical Physics **29**, 294 (1958).

[67] G. Wentzel, *Eine Verallgemeinerung der Quantenbedingungen für die Zwecke der Wellenmechanik*, Zeitschrift für Physik **38**, 518 (1926).

[68] H. A. Kramers, *Wellenmechanik und halbzahlige Quantisierung*, Zeitschrift für Physik **39**, 828 (1926).

[69] L. Brillouin, *La mécanique ondulatoire de Schrödinger: une méthode générale de resolution par approximations successives*, Comptes Rendus de l'Academie des Sciences **183**, 24 (1926).

[70] H. Friedrich and J. Trost, *Working with WKB waves far from the semiclassical limit*, Physics Reports **397**, 359 (2004).

[71] W. Lamb and R. Retherford, *Fine structure of the hydrogen atom by a microwave method*, Physical Review **72**, 241 (1947).

[72] D. F. Walls and G. J. Milburn, *Quantum Optics* (Springer Verlag, Berlin, 2008), 2nd edition.

[73] A. Lambrecht, P. A. M. Neto, and S. Reynaud, *The Casimir effect within scattering theory*, New Journal of Physics **8**, 243 (2006).

[74] R. Fermani, S. Scheel, and P. Knight, *Trapping cold atoms near carbon nanotubes: Thermal spin flips and Casimir-Polder potential*, Physical Review A **75**, 062905 (2007).

[75] Y. B. Zel'dovich, *Theory of Interaction between an atom and a metal*, Zh. Eksp. Teor. Fiz. **5**, 22 (1935).

[76] A. Marvin and F. Toigo, *Van der Waals interaction between a point particle and a metallic surface. I. Theory*, Physical Review A **25**, 782 (1982).

[77] C. Eberlein and R. Zietal, *Retarded Casimir-Polder force on an atom near reflecting microstructures*, Physical Review A **80**, 012504 (2009).

[78] V. B. Bezerra, E. R. Bezerra de Mello, G. L. Klimchitskaya, V. M. Mostepanenko, *et al.*, *Exact CasimirPolder potential between a particle and an ideal metal cylindrical shell and the proximity force approximation*, The European Physical Journal C **71**, 1614 (2011).

[79] M. Schmeits and A. Lucas, *Physical adsorption and surface plasmons*, Surface Science **64**, 176 (1977).

[80] G. Barton, *Frequency shifts near an interface: inadequacy of two-level atomic models*, Journal of Physics B **7**, 2134 (1974).

[81] V. R. Belosludov, A. M. Korotkikh, and V. M. Nabutovskii, Paper at 6th Conf. on Surface forces, Moscow (1976).

[82] D. Langbein, *Theory of van der Waals attraction*, Springer Tracts Mod. Phys. **72**, 1 (1974).

[83] M. Boustimi, J. Baudon, and J. Robert, *Molecules interacting with a metallic nanowire*, Physical Review B **67**, 045407 (2003).

[84] Y. S. Barash and A. A. Kyasov, *Interaction potential for two filaments and for an atom interacting with a filament*, Sov. Phys. JETP **68**, 39 (1989).

[85] H. A. Bethe and E. E. Salpeter, *Handbuch der Physik Vol. XXXV* (Springer Verlag, Berlin, 1957).

[86] Z.-C. Yan, J. F. Babb, A. Dalgarno, and G. W. F. Drake, *Variational calculations of dispersion coefficients for interactions among H, He, and Li atoms*, Physical Review A **54**, 2824 (1996).

[87] C. Pekeris, *$1\,^1S$ and $2\,^3S$ states of helium*, Physical Review **115**, 1216 (1959).

[88] Z.-C. Yan and J. F. Babb, *Long-range interactions of metastable helium atoms*, Physical Review A **58**, 1247 (1998).

[89] Z.-C. Yan, A. Dalgarno, and J. F. Babb, *Long-range interactions of lithium atoms*, Physical Review A **55**, 2882 (1997).

[90] P. Kharchenko, J. F. Babb, and A. Dalgarno, *Long-range interactions of sodium atoms*, Physical Review A **55**, 3566 (1997).

[91] A. Derevianko, W. R. Johnson, M. S. Safronova, and J. F. Babb, *High-precision calculations of dispersion coefficients, static dipole polarizabilities, and atom-wall interaction constants for alkali-metal atoms*, Physical Review Letters **82**, 3589 (1999).

[92] C. Eberlein and R. Zietal, *Force on a neutral atom near conducting microstructures*, Physical Review A **75**, 032516 (2007).

[93] F. Arnecke, H. Friedrich, and J. Madroñero, *Scattering of ultracold atoms by absorbing nanospheres*, Physical Review A **75**, 042903 (2007).

[94] M. O'Carroll and J. Sucher, *Arctangent approximation to the intermolecular potential*, Physical Review **187**, 85 (1969).

[95] M. Fink, *Streuung von kalten Atomen an einem Nanodraht*, Diplomarbeit, Technische Universität München (2011).

[96] F. Arnecke, H. Friedrich, and J. Madroñero, *Effective-range theory for quantum reflection amplitudes*, Physical Review A **74**, 062702 (2006).

[97] L. Rayleigh, *On the electromagnetic theory of light*, Philosophical Magazine Series 5 **12**, 81 (1881).

[98] L. Rayleigh, *The dispersal of light by a dielectric cylinder*, Philosophical Magazine Series 6 **36**, 365 (1918).

[99] J. D. Jackson, *Classical Electrodynamics* (John Wiley & Sons, New York, 1999), 3rd edition.

[100] H. C. Van de Hulst, *Light Scattering by Small Particles* (John Wiley & Sons, New York, 1957).

[101] J. C. Maxwell, *A dynamical theory of the electromagnetic field*, Philosophical Transactions of the Royal Society of London **155**, 459 (1865).

[102] H. Hönl, A. W. Maue, and K. Westphal, *Theorie der Beugung*, in *Handbuch der Physik Bd. XXV/1* (Springer Verlag, Berlin, 1961).

[103] H. C. Hamaker, *The London - van der Waals attraction between spherical particles*, Physica **4**, 1058 (1937).

[104] P. Rodriguez-Lopez, S. J. Rahi, and T. Emig, *Three-body Casimir effects and non-monotonic forces*, Physical Review A **80**, 022519 (2009).

[105] G. L. Klimchitskaya, E. V. Blagov, and V. M. Mostepanenko, *Casimir-Polder interaction between an atom and a cylinder with application to nanosystems*, Journal of Physics A **39**, 6481 (2006).

[106] E. V. Blagov, G. L. Klimchitskaya, and V. M. Mostepanenko, *Van der Waals interaction between microparticle and uniaxial crystal with application to hydrogen atoms and multiwall carbon nanotubes*, Physical Review B **71**, 235401 (2005).

[107] V. Druzhinina, M. Mudrich, F. Arnecke, J. Madroñero, *et al.*, *Thermal disequilibrium effects in quantum reflection*, Physical Review A **82**, 032714 (2010).

[108] P. Schneeweiss, *Ultracold thermal atoms and Bose-Einstein condensates interacting with a single carbon nanofiber*, Dissertation, Universität Tübingen (2011).

[109] P. Schneeweiss, *private communication* (2012).

[110] M. Gierling, *Rastersondenmikroskopie mit ultrakalten Atomen*, Dissertation, Universität Tübingen (2011).

[111] P. Meystre, *Atom Optics* (Springer Verlag, Berlin, 2001).

[112] Y.-j. Lin, I. Teper, C. Chin, and V. Vuletić, *Impact of the Casimir-Polder potential and Johnson noise on Bose-Einstein condensate stability near surfaces*, Physical Review Letters **92**, 050404 (2004).

[113] H. C. Andersen, *Molecular dynamics simulations at constant pressure and/or temperature*, The Journal of Chemical Physics **72**, 2384 (1980).

[114] D. M. Harber and J. M. McGuirk, *Thermally induced losses in ultra-cold atoms*, Journal of Low Temperature Physics **133**, 229 (2003).

[115] W. H. Press, S. A. Teukolsky, W. T. Vetterling, and B. P. Flannery, *Numerical Recipes: The Art of Scientific Computing* (Cambridge University Press, Cambridge, 1992), 3rd edition.

[116] L. D. Landau and E. M. Lifshitz, *Statistical Physics* (Pergamon Press, Oxford, 1980), 3rd edition.

[117] P. S. Julienne, *Ultracold molecules from ultracold atoms: a case study with the KRb molecule*, Faraday Discussions **142**, 361 (2009).

[118] L. D. Landau and E. M. Lifshitz, *Mechanics* (Butterworth-Heinemann, Oxford, 1981), 3rd edition.

[119] I. Bloch, J. Dalibard, and W. Zwerger, *Many-body physics with ultracold gases*, Reviews of Modern Physics **80**, 885 (2008).

[120] C. Zipkes, S. Palzer, C. Sias, and M. Köhl, *A trapped single ion inside a Bose-Einstein condensate*, Nature **464**, 388 (2010).

[121] A. D. O'Connell, M. Hofheinz, M. Ansmann, R. C. Bialczak, *et al.*, *Quantum ground state and single-phonon control of a mechanical resonator*, Nature **464**, 697 (2010).

Acknowledgments

First and foremost I would like to thank Harald Friedrich for giving me the opportunity to join his group and for supervising this work. His advice, his ideas, and his critical questions have contributed substantially to the success of this project. It has always been a pleasure working with him. His way of thinking about physics and life in general has influenced me not only academically, but also personally.

I am indebted to Javier Madroñero who supported this project with numerous ideas and insightful discussions and who considerably contributed to its success. I am grateful to all the other group members of T30a, Tim-Oliver Müller, Sebastian Schröter, Johannes Eiglsperger, Patrick Raab, Florian Arnecke, Moritz Schönwetter, Alexander Kaiser, and Frauke Schwarz, with whom I had the pleasure of working together during the last years and who supported this work.

I would like to thank József Fortágh, Andreas Günther, Philip Schneeweiss, and Tom Judd for helpful discussions on the nanotube experiment and for sharing their experimental data.

Last but not least I want to thank my family and friends who supported and encouraged me throughout my studies. I am especially grateful to Kerstin who has always been a major support to me and to our daughter for distracting me from physics and giving me unlimited happiness and pleasure.